

Elucidating the Role of  
Transition Metal  
Electronic Structure in  
Catalysis and Spin  
Relaxation

Thesis by  
Kaitlin M. Luedecke

In Partial Fulfillment of the Requirements for  
the Degree of  
Doctor of Philosophy

The Caltech logo, featuring the word "Caltech" in a bold, orange, sans-serif font, centered within a light yellow rectangular background.

CALIFORNIA INSTITUTE OF TECHNOLOGY  
Pasadena, California

2025  
(Defended May 1, 2025)

© 2025

Kaitlin M. Luedecke  
ORCID: 0000-0002-8163-9417

*“And on the other side,*

*Why should we deny the truth?*

*We could have less to worry about, honey,*

*I won’t lie to you.”*

*- Andrew John Hozier-Byrne*

## ACKNOWLEDGEMENTS

This season of my life has been better than I ever could have hoped for—beyond my wildest, wildest dreams. Moving across the country to California for the chance to earn my PhD in chemistry is something that I will never regret. The last few years here at Caltech and in Pasadena have been so life-changing, life-enhancing, and fulfilling. I have been so happy here, and largely, that happiness comes from the people who surround me. Every day I reflect on how grateful (lucky!) I am to be in this specific place at this specific time with these specific people! Here follows my attempt to string together some notes of thanks to those who have made this journey so worthwhile.

First, I would like to thank the person who introduced me to the world of inorganic chemistry research and who has remained a mentor to me ever since. I was just 18 years old when I took Prof. Gregory Robinson's honors general chemistry course at the University of Georgia. Shortly thereafter, Prof. Robinson invited me into his research laboratory, and the rest seems like history. Greg has been the best, most encouraging mentor I have ever had. Thank you for always believing in me (even when I doubt myself) and for pushing me to strive for the best. It has been so wonderful to remain close even after undergrad and throughout graduate school—having you visit Caltech and seeing you at my wedding have been particularly meaningful moments over these last few years. I appreciate your guidance in my life more than you could ever know!

Along the line of thanking educators, I would also like to send my appreciation to Stephanie Sisk and Shelly Dowse, my high school AP biology and AP chemistry teachers. Ms. Sisk—you opened my eyes to science in a way that made me think that it could be fun! Your engaging stories about roadkill and pinworms made me laugh in class—and I think that laughter was the key to making science approachable for me. You also were always so encouraging and understanding, two traits that I appreciated a lot during my high school days. Ms. Dowse, thank you for giving me a rigorous introduction to chemistry! I appreciated your teaching style and positive demeanor in class. Thanks also to Barbara Baker, my high school band director. Ms. Baker—you molded me as a person more than I could have anticipated from a band program. From you, I learned to appreciate

other peoples' experiences and the importance of being a good person and leader. These soft skills have served (and will continue to serve) me well in life!

My training as an inorganic chemist has benefited greatly from the mentorship of senior graduate students. Dr. Hunter Hickox was my graduate-student mentor when I was an undergraduate in Prof. Robinson's lab. Thank you, Hunter, for being such a patient, kind mentor, a good example of a hard worker, and a good friend! I look back fondly on our jams to music in the lab (and that time you tricked me into eating a flower at that conference in Charlotte...). It has been great to keep in touch these last few years, and I am so proud of you! Dr. Ryan Ribson was my first mentor when I was a new graduate student in the Hadt lab. Ryan taught me so much about synthetic chemistry and introduced me to Caltech as a whole. It was always so fun to get margaritas and chat with you!

I have benefited a lot from the guidance of various professors at Caltech as well. Thank you to the members of my committee: Prof. Scott Cushing, Prof. Theo Agapie, and Prof. Kim See. I appreciated all of the scientific and nonscientific discussions and feedback from you all! In particular, I would like to thank Scott, the chair of my committee, for not only directing all of my committee meetings, but also for always leading with kindness and consideration.

When I was exploring research groups to join as a first year at Caltech, I knew that I could get excited about really any research direction. What was most important to me was working for someone who was *kind*. In this search, I found Prof. Ryan Hadt's physical inorganic research group as my home. Ryan, I cannot thank you enough for taking a chance on me all those years ago. We have had quite the journey together these last few years, but through it all, I could always count on you to foster an encouraging lab environment by leading with kindness (the pillars of the Hadt lab, perhaps?). I have found myself mulling (mauling? malling? moling?) over my PhD experience recently, and I can fully say that working in your lab and with you has been the best possible option I ever could have taken. Thank you for always believing in me and supporting me. I appreciate you!

Not only is the leader of the Hadt lab kind—but I have had the privilege to work alongside some of the smartest, most good-natured people in the Hadt lab as well. Thank

you to Dr. Gautam Stroschio, Dr. Alec Follmer, Dr. Ryan Ribson, Dr. Brendon McNicholas, Dr. Daniel Bím, Dr. Thais Scott, Dr. Paul Oyala, Dr. Ruben Mirzoyan, Dr. David Cagan, Nate Lopez, Kevin Alexander, Matthew Cox, Kate Benson, Dr. Stephen DiLuzio, Dr. Erica Sutcliffe, Dr. Stefan Lohaus, Dr. Jake Rothbaum, Dr. Kay Xia, Jonathan Aalto, Maria Blankemeyer, Keon Ha Hwang, Nathanael Kazmierczak, Joyce Kazmierczak, Arshiyam Alam Laaj, Chris (Goose) Totoiu, and Juliette Whiteside for being great coworkers during my time here. In particular, I have co-authored papers and worked on projects with Alec, Daniel, David, Nate, Paul, Stefan, Nathanael, Ryan, Matthew, Kevin, Stephen, Kate, and Keon Ha—thanks to you all for being so helpful and rigorous! Everyone in the group is always so eager to help each other out, discuss a hard problem, etc., and I am so appreciative. Alec, Ryan, and Erica, thank you for teaching me how to use the transient absorption setup in the lab. Daniel, thank you for taking me under your wing to learn computational chemistry and theory—you are a great teacher! Brendon, thank you for teaching me e-chem and for being a good friend as well. It is so great to see you as a professor in Tennessee! Thanks also to Nathanael and Paul for being the most patient at training me on the electron paramagnetic resonance instruments—through frustrations and triumphs!

Erica and Maria—working next to you both in the office has been such a treat. Erica, you joining the group meant I was no longer the only woman in the group—and how lovely it has been to work alongside you and have your friendship! You are so kind and smart and humble, and I cannot wait to see what's next in your future. You deserve the best! And Maria—you are literally one of the smartest people I know. And you're soooooo funny and fun and hard-working! I have learned a lot from you. I know that no matter what is in store for your future, you are going to do great things. I am so proud of you!

To my cohort, Nathanael and Goose—what a pleasure these last few years have been. Thank you both for your friendship and sanity-checks throughout the years. Nathanael, I have really enjoyed working alongside you on projects and have appreciated your teaching. I always learn so much from you (especially which words of my vocabulary are archaic). It has been so exciting to follow your (and Joyce's) journey, and I know without

a shadow of a doubt that you will do meaningful things in Michigan. Goose, I am so grateful for your friendship as well. Hearing you “honk” in the office about Winston Churchill or some other historical figure always lightened the mood! And you were the best inorganic–organometallics seminar co–host. Learning alongside you both and finding our place in the lab has been so meaningful to me. Our lunches and time spent together will be times I look back on fondly. Cheers to us!

David, thank you for being a good friend and person. From you, I have had lots of long talks about what it means to be a good scientist *and* a good person, and I find myself following those discussions still. You deserve everything that you have worked for, and I know that you will be successful on your journey in science. Finally, to the rest of Team LiSA, Stephen and Keon Ha—thank you both for keeping all of us on track and our heads on our shoulders. I am grateful for our discussions and friendships!

I must also extend a heartfelt thank you to my other friends at Caltech: Enric Adillon, Sasha Alabugin, Madeline Hicks, Levi Palmer, Jocelyn Mendes, and Dr. Danika Nimlos. Enric and Sasha, I have been “in this” with you guys since the very beginning. It has been so refreshing to have friends who I can fully be myself with and discuss anything with. Thank you both for all of the fun adventures, coffee breaks, and discussions we have had over the last few years. Madeline, thank you for keeping it real. I always appreciate your perspective on problems and topics, and writing letters encouraging people to vote is one of my favorite memories while at Caltech. Levi, Jocelyn, and Danika—my Cushing lab friends! Levi, thank you for always being a leader and such a caring, funny friend. It was so fun to organize an American Chemical Society symposium alongside you! Jocelyn, my wonderful, book-loving, kind friend. Thank you for all of our wine nights and run clubs and book reviews! You are going to absolutely crush whatever is next for you! And Danika, thank you for introducing me to your soccer friends and always being down for a beer or to chat about the world.

I would surely not have made it through my PhD with my head screwed on right if not for my communities outside of the immediate Caltech sphere. Thank you to my trivia team, Dr. Paul Oyala, Nate Hart, Dr. John Ovian, Dr. Christian Johansen, Emily Boyd, and Fernando Guerrero. I have looked forward to Tuesday nights at 8 p.m. at T-Boyles

each week! Thank you to my soccer friends, Michelle Leiker, Lulu Martinez, Jen Chuck, Janel Foo, Danika Nimlos, Jackie Cruz, Hannah Levy, Corey Crossfield, Catalina Combs, Bre Gibson, and Angie Capra. It has been so freeing to bring myself back to playing on a field, and every Monday night with you ladies is such a treat. Finally, I cannot thank my SoulCycle friends—Armineh Yousefian, Lauren Castle, Ana El Beleidy, Angela Tom, Lily Rosenbloom, and Alison Walker—enough for the perspectives they have shown me on life! You all have instilled such confidence in me and reminded me time and time again that being a good person is the most important thing in life. It has been such a privilege to be surrounded by such fun, intelligent, funny, kind, and bada\*\* women. Thank you for riding bikes that go nowhere with me! I have rather found that they take us ~everywhere we need to go~ instead.

Thank you to my parents, Patricia Luedecke and James Luedecke, for always encouraging me to do my best in school and making sure I was able to reach my goals. I would not have made it this far if not for my sister, Maddie Luedecke. Maddie, thank you for being the best emotional support/just general supporter of me. I cannot thank you enough for answering any call to talk me through a problem, for constant reassurance, for believing in me, and for going with me to every Hozier concert. It has been so fun to see us become friends these last few years, and I am so excited for our future adventures! (Thank you also for letting me talk to my niece Kailani on FaceTime whenever I'm sad at work!)

I am so grateful for the best in-laws that anyone could ever hope for. Sandi and Moe, thank you both for being like second parents to me. And Marissa (and Matt) and Tyler, thank you for treating me like family as well. I am so grateful for all of your love and support, whether it comes as visits to California or career advice!

I am so lucky to be married to the best man ever, Josh Trebuchon. Josh has been my rock throughout this entire PhD journey, and I am so grateful for all of his love and support these last few years. Thank you for always celebrating my wins, consoling me when I'm down, and for assuring me that no matter what, everything will be okay. I love you so much and am so excited for this next step of our future together (and for us to get a dog soon)!

Finally, I must end my acknowledgements with the biggest thank you to my grandparents, John and Anne Cronin. My grandparents immigrated to the United States from Ireland more than 50 years ago, and they have worked so hard to ensure that their family has the best life possible. From my grandparents, I have learned the importance of education and lifelong learning, to appreciate the nature around us, and to enjoy peace. To be quick to praise and to be slow to judge—to be kind in our pursuit of happiness. One of the major reasons I set out to get my PhD was to be the first in the family to be called a “doctor”—to make them proud. Thank you, Grandpa and Grandma, for all you have sacrificed and all you have taught me and done for me. You can call me Dr. Katie, now! I love you all the way.

## ABSTRACT

Transition metal complexes are the workhorses of physical inorganic chemistry and have diverse applications in catalysis and quantum information science, especially. The primary descriptor of transition metal complexes, and a good predictor of their utility, is their electronic structure. Notably, rigorous characterization of the spin states, oxidation states, excited states, and magnetic properties of these complexes is necessary to gain mechanistic detail for these applications; this thesis focuses on elucidating the role of transition metal electronic structure in catalysis and spin relaxation. Chapter 1 introduces important transition metal electronic structure considerations and motivates these studies. Part I includes Chapters 2–4 and considers complexes relevant for CO<sub>2</sub> reduction chemistry and cross-coupling reactivity. Chapter 2 investigates the conditions under which a CO<sub>2</sub> reduction catalyst, Fe-*p*-TMA, undergoes speciation changes and characterizes its excited-state identities and lifetimes. Chapter 3 considers the electrochemical conditions under which highly reduced CO reduction products are generated in an iron porphyrin system, and important connections to photocatalysis are made. Chapter 4 compares the excited-state identities and reactivities of prototypical and tethered Ni(II)-bpy aryl halide complexes. Part 2 includes Chapters 5–6 and focuses on spin relaxation, a key figure of merit in quantum information science. Chapter 5 investigates the effect of structural distortions in  $S = \frac{1}{2}$  copper porphyrin systems on their spin-lattice relaxation times, and Chapter 6 moves to identifying the mechanism of spin relaxation in an  $S = 1$  Cr(*o*-tolyl)<sub>4</sub> system. Together, these compiled studies reveal the nuanced roles of transition metal electronic structure in catalysis and spin relaxation and highlight the importance of their characterization for developing optimized systems.

## PUBLISHED CONTENT AND CONTRIBUTIONS

Follmer, A. H.<sup>†</sup>; **Luedecke, K. M.<sup>†</sup>**; Hadt, R. G. “ $\mu$ -Oxo Dimerization Effects on a Ground- and Excited-State Properties of a Water-Soluble Iron Porphyrin CO<sub>2</sub> Reduction Catalyst.” *Inorg. Chem.* **2022**, *61*, 20493. DOI: 10.1021/acs.inorgchem.2c03215.

K. M. L. contributed equally to the manuscript with A. H. F. K. M. L. participated in designing the study, synthesized compounds, carried out all experiments, performed data analyses, prepared figures, wrote the manuscript, and was involved in manuscript editing.

Kazmierczak, N. P.<sup>†</sup>; **Luedecke, K. M.<sup>†</sup>**; Gallmeier, E. T.; Hadt, R. G. “ $T_1$  Anisotropy Elucidates Spin Relaxation Mechanisms in an  $S = 1$  Cr(IV) Optically Addressable Molecular Qubit.” *J. Phys. Chem. Lett.* **2023**, *14*, 7658. DOI: 10.1021/acs.jpcclett.3c01964.

K. M. L. contributed equally to the manuscript with N. P. K. K. M. L. synthesized compounds, prepared all experimental samples, participated in data collection and analysis, contributed to figure generation, and contributed to writing and editing the manuscript.

Kazmierczak, N. P.; Lopez, N. E.; **Luedecke, K. M.**; Hadt, R. G. “Determining the Key Vibrations for Spin Relaxation in Ruffled Cu(II) Porphyrins via Resonance Raman Spectroscopy.” *Chem. Sci.* **2024**, *15*, 2380. DOI: 10.1039/D3SC05774G.

K. M. L. mentored N. E. L. through the synthesis of compounds and sample preparation, participated in data collection, analysis, and figure generation, and contributed to writing and editing the manuscript.

Bím, D.; **Luedecke, K. M.**; Cagan, D. A.; Hadt, R. G. “Light Activation and Photophysics of a Structurally Constrained Nickel(II)-Bipyridine Aryl Halide Complex.” *Inorg. Chem.* **2024**, *63*, 4120. DOI: 10.1021/acs.inorgchem.3c03822.

K. M. L. participated in data collection and analysis, including all ultrafast spectroscopic experiments and analyses, participated in figure generation, and contributed to writing and editing the manuscript.

## TABLE OF CONTENTS

Acknowledgements .....	iv
Abstract.....	x
Published Content and Contributions .....	xi
Table of Contents .....	xii
List of Schemes and Figures .....	xv
List of Tables.....	xviii
List of Equations .....	xix
Nomenclature and Abbreviations .....	xx
<b>Chapter 1: Introduction</b> .....	1
1.1. Introduction .....	2
1.2. Catalysis.....	2
1.2.1. $CO_x$ ( $x = 1, 2$ ) Reduction with Iron Porphyrin Catalysts.....	2
1.2.2. Cross-coupling Reactions .....	4
1.3. Spin Relaxation .....	5
1.3.1. $S = 1/2$ Molecules.....	5
1.3.2. $S = 1$ Molecules.....	6
1.4. Compound Scope .....	7
1.5. References .....	8
<b>Part I: Catalysis</b> .....	12
<b>Chapter 2: <math>\mu</math>-oxo Dimerization Effects on Ground- and Excited-State Properties of a Water-Soluble Iron Porphyrin <math>CO_2</math> Reduction Catalyst</b> .....	13
2.1. Introduction .....	14
2.2. Results and Analysis .....	15
2.2.1. UV-vis Spectroscopy .....	15
2.2.2. EPR and MCD Spectroscopy.....	18
2.2.3. Ultrafast TA Spectroscopy .....	20
2.3. Discussion.....	25
2.4. Conclusions .....	29
2.5. References .....	30
<b>Chapter 3: The Non-innocent Role of Amine Additives in the Electrochemical Generation of Highly Reduced <math>CO</math> Reduction Products in a Molecular Iron Porphyrin System</b> .....	35

<b>Chapter 4: Photophysics of a Structurally Constrained Ni(II)-Bipyridine Aryl Halide Complex</b> .....	60
4.1. Introduction .....	61
4.2. Results and Analysis .....	64
4.2.1. <i>Steady-State UV-vis Absorption Spectroscopy</i> .....	64
4.2.2. <i>Photochemical Activity</i> .....	66
4.2.3. <i>Transient Absorption Spectroscopy</i> .....	71
4.3. Discussion .....	75
4.4. Conclusions .....	83
4.5. References .....	83
<b>Part II: Spin Relaxation</b> .....	91
<b>Chapter 5: Determining the Key Vibrations for Spin Relaxation in Ruffled Cu(II) Porphyrins via Resonance Raman Spectroscopy</b> .....	92
5.1. Introduction .....	93
5.2. Results .....	97
5.3. Discussion.....	108
5.4. Conclusions .....	109
5.5. References .....	110
<b>Chapter 6: <math>T_1</math> Anisotropy Elucidates Spin Relaxation Mechanisms in an <math>S = 1</math> Cr(IV) Optically Addressable Molecular Qubit</b> .....	116
6.1. Introduction .....	117
6.2. Results and Discussion.....	119
6.3. Conclusions .....	126
6.4. References .....	127
<b>Appendix A: Supporting Information for Chapter 2: <math>\mu</math>-oxo Dimerization Effects on Ground- and Excited-State Properties of a Water-Soluble Iron Porphyrin CO<sub>2</sub> Reduction Catalyst</b> .....	132
<b>Appendix B: Supporting Information for Chapter 3: The Non-innocent Role of Amine Additives in the Electrochemical Generation of Highly Reduced CO Reduction Products in a Molecular Iron Porphyrin System</b> .....	133
<b>Appendix C: Supporting Information for Chapter 4: Photophysics of a Structurally Constrained Nickel(II)-Bipyridine Aryl Halide COMplex</b> .....	153
<b>Appendix D: Supporting Information for Chapter 5: Determining the Key Vibrations for Spin Relaxation in Ruffled Cu(II) Porphyrins via Resonance Raman Spectroscopy</b> .....	154

**Appendix E:** Supporting Information for Chapter 6:  $T_1$  Anisotropy Elucidates Spin Relaxation Mechanisms in an  $S = 1$  Cr(IV) Optically Addressable Molecular Qubit..... 155

## LIST OF SCHEMES AND FIGURES

	<i>Page</i>
<i>Chapter 1</i>	1
<b>Figure 1.1.</b> Redox characterization of iron porphyrin species	3
<b>Figure 1.2.</b> The Zeeman effect, $1/T_1$ , and $1/T_2$ for an $S = 1/2$ system	5
<b>Figure 1.3.</b> Zero-field splitting energy level diagram for an $S = 1$ system	7
<b>Figure 1.4.</b> Structures of molecules included in this thesis	8
 <i>Chapter 2</i>	 13
<b>Figure 2.1.</b> UV-vis and kinetics of Fe- <i>p</i> -TMA $\mu$ -oxo dimer formation in the presence of NaHCO <sub>3</sub>	15
<b>Figure 2.2.</b> UV-vis of Fe- <i>p</i> -TMA in the presence of various electrolytes	16
<b>Figure 2.3.</b> pH titrations of Fe- <i>p</i> -TMA, monitored by UV-vis	18
<b>Figure 2.4.</b> EPR of Fe- <i>p</i> -TMA in various conditions	19
<b>Figure 2.5.</b> MCD of Fe- <i>p</i> -TMA monomer and $\mu$ -oxo dimer	20
<b>Figure 2.6.</b> TA excitation wavelengths mapped onto UV-vis of Fe- <i>p</i> -TMA monomer and $\mu$ -oxo dimer	21
<b>Figure 2.7.</b> Jablonski diagram describing excited-state relaxation of Fe- <i>p</i> -TMA monomer and $\mu$ -oxo dimer	22
<b>Figure 2.8.</b> Normalized EAS wavelength profiles of TA components that described the relaxation of Fe- <i>p</i> -TMA monomer and $\mu$ -oxo dimer from 650 nm excitation	23
<b>Figure 2.9.</b> Normalized EAS wavelength profiles of TA components that described the relaxation of Fe- <i>p</i> -TMA monomer and $\mu$ -oxo dimer from 550 nm excitation	25
 <i>Chapter 3</i>	 35
<b>Figure 3.1.</b> Summary of work done toward identifying the origin of CH <sub>4</sub> formation from photo-/electrochemical CO <sub>2</sub> reduction by Fe- <i>p</i> -TMA	37

<b>Scheme 3.1.</b> Relevant reactions that occur under CO or CO <sub>2</sub> electro-reductive conditions	38
<b>Scheme 3.2.</b> Common degradation pathways for tertiary alkyl amines in photoredox catalysis	38
<b>Figure 3.2.</b> CV of Fe- <i>p</i> -TMA under Ar and CO	40
<b>Figure 3.3.</b> CV of Fe- <i>p</i> -TMA under Ar and CO in the presence of different acids	41
<b>Figure 3.4.</b> CPE at -2.1 V vs. Fe <sup>0/+</sup> of Fe- <i>p</i> -TMA samples containing NH <sub>4</sub> BF <sub>4</sub> and PhOH additives under CO	45
<b>Figure 3.5.</b> Faradaic efficiencies over time for CH <sub>4</sub> formation after CPE of NH <sub>4</sub> BF <sub>4</sub> , NH <sub>4</sub> BF <sub>4</sub> and Fe- <i>p</i> -TMA, and PhOH and Fe- <i>p</i> -TMA under CO	46
<b>Figure 3.6.</b> Faradaic efficiencies over time after CPE of only NH <sub>4</sub> BF <sub>4</sub> versus NH <sub>4</sub> BF <sub>4</sub> and Fe- <i>p</i> -TMA under CO	47
<b>Figure 3.7.</b> GC-MS spectra after CPE of Fe- <i>p</i> -TMA with PhOH versus Fe- <i>p</i> -TMA with NH <sub>4</sub> BF <sub>4</sub>	49
<i>Chapter 4</i>	60
<b>Figure 4.1.</b> Mechanisms of Ni–C bond homolysis for Ni(II)–bpy aryl halides	62
<b>Figure 4.2.</b> UV-vis of tethered and untethered Ni(II)-bpy aryl halide complexes	65
<b>Figure 4.3.</b> Photoirradiation of tethered and untethered Ni(II)-bpy aryl halide complexes in the presence and absence of mesityl bromide, monitored by UV-vis	67
<b>Figure 4.4.</b> Paramagnetic <sup>1</sup> H-NMR and UV-vis characterization of the irradiation product of the tethered Ni(II)–bpy aryl halide complex	70
<b>Figure 4.5.</b> Jablonski diagram describing the excited-state relaxation pathways of the tethered and untethered Ni(II)-bpy aryl halide complexes	73
<b>Figure 4.6.</b> Transient absorption of the tethered Ni(II)-bpy aryl halide complexes	74

<b>Figure 4.7.</b> Cross-coupling scheme describing selectivity in Ni(II)-bpy aryl halide ground- and excited-state catalysis	77
<b>Figure 4.8.</b> Mechanism for reversible Ni–C bond homolysis	79
<b>Figure 4.9.</b> DFT-optimized geometric distortions of tethered and untethered Ni(II)-bpy aryl halide complexes upon $^3\text{LF}$ state formation	81
<i>Chapter 5</i>	92
<b>Figure 5.1.</b> Mechanistic studies of spin-lattice relaxation in $S = \frac{1}{2}$ qubits	94
<b>Figure 5.2.</b> Geometries and vibrational modes of ruffled copper porphyrins	96
<b>Figure 5.3.</b> Temperature-dependent $T_1$ of CuOEP, CuTPP, and CuTiPP	100
<b>Figure 5.4.</b> Calculated spin relaxation rates $1/T_1$ for copper porphyrins	102
<b>Figure 5.5.</b> Calculated vs. experimental $1/T_1$ log-log slopes for CuOEP and CuTiPP	104
<b>Figure 5.6.</b> $1/T_1$ vs. temperature and Raman spectra of copper porphyrins; comparison to back-out relevant vibrational mode energies	105
<i>Chapter 6</i>	116
<b>Scheme 6.1.</b> Molecular crystal structures and point groups of $S = 1$ Cr( <i>o</i> -tolyl) $_4$ and $S = \frac{1}{2}$ Cr(acac) $_2$	118
<b>Figure 6.1.</b> Temperature-dependent pulse EPR for ZFS determination of Cr( <i>o</i> -tolyl) $_4$	120
<b>Figure 6.2.</b> $T_1$ anisotropy and functional fitting of $S = 1$ Cr( <i>o</i> -tolyl) $_4$ and $S = \frac{1}{2}$ Cr(acac) $_2$	122
<b>Figure 6.3.</b> Temperature dependence of $T_1$ anisotropy contributions for $S = 1$ Cr( <i>o</i> -tolyl) $_4$ and $S = \frac{1}{2}$ Cr(acac) $_2$	124

## LIST OF TABLES

	<i>Page</i>
<i>Chapter 2</i>	13
<b>Table 2.1.</b> Excited-state lifetimes of Fe- <i>p</i> -TMA monomer and $\mu$ -oxo dimer	28
<i>Chapter 5</i>	92
<b>Figure 5.1.</b> Normal coordinate structural decomposition analysis of porphyrin distortions	98
<b>Figure 5.2.</b> Copper porphyrin local mode energies and Raman mixed ligand symmetric stretch peaks	108

## LIST OF EQUATIONS

	<i>Page</i>
<i>Chapter 5</i>	92
<b>Equation 5.1.</b> Theoretical prediction of $1/T_1$ based from molecular spin-phonon coupling considerations	101
<b>Equation 5.2.</b> Local mode fitting of $1/T_1$ data	105
 <i>Chapter 6</i>	 116
<b>Figure 6.1.</b> Relationship between $\sin^2(2\theta)$ and $T_1$ anisotropy	125

## NOMENCLATURE AND ABBREVIATIONS

$1/T_1$	Spin-lattice relaxation rate
$^3\text{LF}$	Triplet ligand field
<i>AgCl</i>	Silver chloride
<i>B</i>	Externally-applied magnetic field
<b>Bpy</b>	Bipyridine
<b>CE</b>	Counter electrode
<b>CH<sub>4</sub></b>	Methane
<b>C<sub>2</sub>H<sub>4</sub></b>	Ethylene
<b>C<sub>2</sub>H<sub>6</sub></b>	Ethane
<b>C<sub>6</sub>H<sub>6</sub></b>	Benzene
<b>COR</b>	Carbon monoxide (CO) reduction
<b>CO</b>	Carbon monoxide
<b>CO<sub>2</sub></b>	Carbon dioxide
<b>CO<sub>2</sub>R</b>	Carbon dioxide (CO <sub>2</sub> ) reduction
<b>CO<sub>2</sub>RR</b>	Carbon dioxide (CO <sub>2</sub> ) reduction reaction
<b>CO<sub>x</sub> (x = 1, 2)</b>	Carbon monoxide (x = 1) or carbon dioxide (x = 2)
<b>CPE</b>	Controlled potential electrolysis
<b>Cr(DTBMS)<sub>4</sub></b>	Tetrakis(ditert-butylmethylsiloxide)chromium
<b>CrO(HEBA)<sub>2</sub><sup>-</sup></b>	Oxo-chromium bis(2-hydroxy-2-ethylbutyrate)
<b>Cr(<i>o</i>-tolyl)<sub>4</sub></b>	Tetrakis( <i>o</i> -tolyl)chromium

<b>CS<sub>2</sub></b>	Carbon disulfide
<b>CSD</b>	Cambridge structure database
<b>Cu(acac)<sub>2</sub></b>	Copper acetylacetonate
<b>Cu(mnt)<sub>2</sub><sup>2-</sup></b>	Copper maleonitriledithiolate
<b>CuOEP</b>	Copper octaethylporphyrin
<b>CuP</b>	Copper porphyrin
<b>CuPc</b>	Copper phthalocyanine
<b>CuTiPP</b>	Copper tetraisopropylporphyrin
<b>CuTPP</b>	Copper tetraphenylporphyrin
<b>CV</b>	Cyclic voltammetry
<b>CW</b>	Continuous wave
<b><i>D</i></b>	Axial zero-field splitting (parameter)
<b><i>D</i><sub>4h</sub></b>	Square planar
<b>DFT</b>	Density functional theory
<b>DMF</b>	Dimethylformamide
<b><i>e</i><sup>-</sup></b>	Electron
<b><i>E</i></b>	Rhombic zero-field splitting
<b><i>E</i><sub>1/2</sub></b>	Half-wave potential
<b><i>E</i><sub>p,c</sub></b>	Peak cathodic current potential
<b>EAS</b>	Evolution-associated spectra
<b>EDFS</b>	Echo-detected field sweep
<b>EPR</b>	Electron paramagnetic resonance (spectroscopy)

<b>ESEEM</b>	Electron spin echo envelope modulation
<b>EtOH</b>	Ethanol
<b>Fc</b>	Ferrocene
<b>FE</b>	Faradaic efficiency
<b>FeCHOP<sup>+</sup></b>	Protonated ferrous carbonyl porphyrin
<b>FeCOP</b>	Ferrous carbonyl porphyrin
<b>FeP</b>	Iron porphyrin
<b>Fe-<i>p</i>-TMA</b>	Iron 5,10,15,20-tetra( <i>para</i> - <i>N,N,N</i> -trimethylanilinium)porphyrin
<b>FeTMPyP</b>	Iron tetrakis( <i>N</i> -methyl-4-pyridyl)porphyrin
<b>FeTPP</b>	Iron tetraphenylporphyrin
<b>GC</b>	Glassy carbon
<b>GC</b>	Gas chromatography
<b>GC-MS</b>	Gas chromatography-mass spectrometry
<b>GSB</b>	Ground state bleach
<b>H<sup>•</sup></b>	Hydrogen atom
<b>H<sup>+</sup></b>	Proton
<b>H<sub>2</sub></b>	Hydrogen
<b>H<sub>2</sub>O</b>	Water
<b>HER</b>	Hydrogen evolution reaction
<b>IPCC</b>	International Panel on Climate Change
<b>IR</b>	Infrared
<b>Ir(ppy)<sub>3</sub></b>	Iridium tris(2-phenylpyridine)

<b>ISC</b>	Intersystem crossing
<b>KCl</b>	Potassium chloride
<b>KNO<sub>3</sub></b>	Potassium nitrate
<b>LF</b>	Ligand field
<b>LMCT</b>	Ligand-to-metal charge transfer
<b>LSS</b>	Ligand symmetric stretch
<b>LUMO</b>	Lowest unoccupied molecular orbital
<b>MCD</b>	Magnetic circular dichroism (spectroscopy)
<b>MHCO<sub>3</sub></b>	Metal bicarbonate
<b>MLCT</b>	Metal-to-ligand charge transfer
<b>MOF</b>	Metal organic framework
<b>MS</b>	Mass spectrometry
<b>NH<sub>3</sub></b>	Ammonia
<b>NH<sub>4</sub><sup>+</sup></b>	Ammonium
<b>NH<sub>4</sub>BF<sub>4</sub></b>	Ammonium tetrafluoroborate
<b>NiTiPP</b>	Nickel tetraisopropylporphyrin
<b>NiTPP</b>	Nickel tetraphenylporphyrin
<b>NMR</b>	Nuclear magnetic resonance (spectroscopy)
<b>NSD</b>	Normal coordinate structural decomposition
<b>NV<sup>-</sup></b>	Anionic nitrogen vacancy center
<b>PCET</b>	Proton coupled electron transfer
<b>PhOH</b>	Phenol

<b>pKa</b>	$-\log_{10}[\text{acid dissociation constant (Ka)}]$
<b>Pd(acac)<sub>2</sub></b>	Palladium acetylacetonate
<b>PXRD</b>	Powder X-ray diffraction
<b>Qubit</b>	Quantum bit
<b>RE</b>	Reference electrode
<b>RMSD</b>	Root-mean-square deviation
<b>RPM</b>	Revolutions per minute
<b>rR</b>	Resonance Raman (spectroscopy)
<b>S</b>	Spin (quantum number)
<b>Sn(<i>o</i>-tolyl)<sub>4</sub></b>	Tetrakis( <i>o</i> -tolyl)tin
<b>T<sub>1</sub></b>	Spin-lattice relaxation time
<b>T<sub>2</sub></b>	Electron spin coherence time
<b>T<sub>d</sub></b>	Tetrahedral
<b>T<sub>m</sub></b>	Phase memory time
<b>TA</b>	Transient absorption (spectroscopy)
<b>TBABF<sub>4</sub></b>	Tetrabutylammonium tetrafluoroborate
<b>UV-vis</b>	Ultraviolet-visible (spectroscopy)
<b>VOPc</b>	Vanadyl phthalocyanine
<b>VOTPP</b>	Vanadyl tetraphenylporphyrin
<b>WE</b>	Working electrode
<b>ZFS</b>	Zero-field splitting
<b>ZnOEP</b>	Zinc octaethylporphyrin

$\partial g/\partial Q$	Spin-phonon coupling coefficient
$\theta$	Angle
$\lambda_{\text{exc.}}$	Excitation wavelength
$\lambda_{\text{max.}}$	Wavelength of maximum intensity/absorbance
$\pi$	Pulse duration
$\tau$	Excited-state lifetime
$\Phi$	Quantum yield
*CO	Adsorbed carbon monoxide

# CHAPTER 1: INTRODUCTION

## 1.1. Introduction

Elucidating the role of transition metal electronic structure in various chemical and physical processes has remained a cornerstone thrust of inorganic chemistry. More specifically, the character of specific electrons in transition metal complexes has implications for their reactivity (e.g., catalysis), excited-state chemistry and relaxation, and magnetism. Therefore, there is much interest in understanding the ground states and optical/magnetically excited states of these compounds. This thesis spans a broad space of applications seen in physical inorganic chemistry, from molecular catalysis to quantum bit (qubit) design. However, a unifying theme across all studies discussed herein is the characterization of the electronic structure of target compounds and investigation into the role their configuration plays in achieving specific goals (for e.g., efficient CO<sub>2</sub> reduction or realizing high-temperature coherence). Ultimately, transition metal electronic structure dictates the abilities of complexes to act in certain applications, so its characterization is the first step toward understanding what limits a complex's ability, leads to a complex's deactivation, or promotes desired behavior in a system.

## 1.2. Catalysis

### 1.2.1. CO<sub>x</sub> ( $x = 1, 2$ ) Reduction with Iron Porphyrin Catalysts

Transition metal complexes make up the large majority of known molecular CO<sub>x</sub> ( $x = 1, 2$ ) reduction catalysts.<sup>1,2</sup> The ability of a transition metal center to bind CO<sub>x</sub> and stabilize intermediates en route toward reduced product formation is largely due to the particular electronic structure of the complex. Iron porphyrins demonstrate a good example of the role electronics play in catalysis; iron porphyrin complexes are a well-known class of CO<sub>2</sub> reduction catalyst that can generate CO or CH<sub>4</sub> both photo- and electrochemically from CO<sub>2</sub> feedstocks.<sup>3,4</sup> In these systems, a reduced *formal* Fe(0) state binds CO<sub>2</sub> and templates it for proton-coupled electron-transfer (PCET) chemistry to give reduced products.<sup>3,5</sup> However, the electronic configuration of this reduced state does not reflect a true Fe(0), d<sup>8</sup> configuration; rather, a resonance structure of an Fe(II) center antiferromagnetically coupled to a porphyrin ligand diradical describes the electron density best (**Figure 1.1**). Indeed, only the first 1 e<sup>-</sup> reduction of Fe(III) to Fe(II) is metal-centered, with the

remaining reduction events taking place on the ligand (**Figure 1.1**).<sup>5</sup> These electronics play a role in catalysis with iron porphyrin species, especially considering that the radical character of the porphyrin macrocycle may lend itself well to deactivation of the active catalyst via ligand degradation pathways.

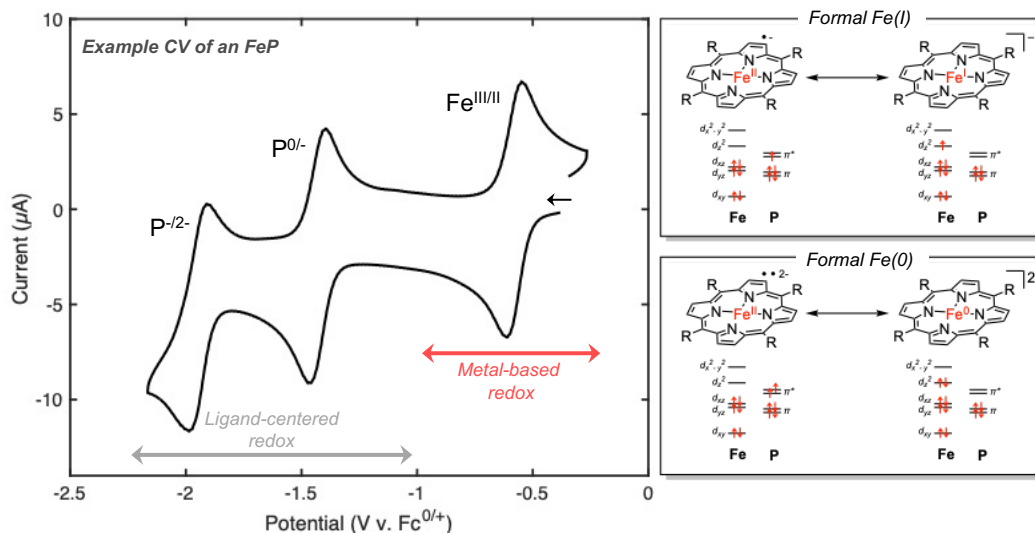


**Figure 1.1.** Redox characterization of iron porphyrin (FeP) species

Further, the Sabatier principle is a key design strategy for the optimal electronic structure of a transition metal catalyst. This principle suggests that maximal activity for  $\text{CO}_x$  reduction occurs when the metal center binds  $\text{CO}_x$  with sufficient energy to support further chemistry of the substrate, but not too strongly such that intermediate reactivity is disfavored.<sup>6</sup> Again, we can use the iron porphyrin's electronic structure as an example for understanding reactivity. Typically, iron porphyrin species are exceptional  $\text{CO}_2$ -to- $\text{CO}$  reduction catalysts, and reactivity beyond  $\text{CO}$  is rare.<sup>7</sup> This trend in reactivity may be explained in part by the very strong binding affinity of  $\text{Fe(II)}$  for  $\text{CO}$ , a key intermediate in catalysis.<sup>8,9</sup> The  $d_{xz}$  and  $d_{yz}$  degenerate orbitals of the iron center can engage in  $\pi$  back-bonding with the unoccupied  $\text{CO } \pi^*$  orbitals, and this interaction stabilizes the  $\text{Fe-C}$  bond while destabilizing the  $\text{C-O}$  bond. The strong-field  $\text{CO}$  ligand also pushes the ferrous center to adopt a low-spin configuration, while the unbound ferrous center has a high-spin

configuration.<sup>10</sup> Spin state indeed influences CO<sub>x</sub> reduction, with product selectivity differences having been reported for iron porphyrin systems depending on high-spin, intermediate-spin, or low-spin electronic configurations.<sup>11</sup>

In this thesis, the excited states of an iron porphyrin CO<sub>x</sub> reduction catalyst were characterized in order to determine their relevance for catalysis. For an excited state to react with substrate, it typically must have a lifetime of at least 1 ns to compete with diffusion.<sup>10</sup> Indeed, we observed that a  $\mu$ -oxo dimer form of the iron porphyrin species that was formed in catalytically relevant conditions exhibited excited-state relaxation on that timescale.<sup>10</sup> Further, we investigated the viability for CO<sub>x</sub> reduction to give CH<sub>4</sub> electrochemically in the same iron porphyrin system. From the electrochemical results, we determined that although the iron porphyrin catalyst was catalytic for the hydrogen evolution reaction, the C-containing reduced products arose from either reduced porphyrin ligand degradation or exogenous acid-based reactivity.

### *1.2.2. Cross-coupling Reactions*

In the field of Ni-centered cross-coupling catalysis, the identity of the excited state that allows for the generation of a reactive species has largely been contended.<sup>12,13</sup> These Ni(II)-bpy aryl halide complexes have shown the remarkable ability to form C-C, C-N, C-O, and C-F bonds upon photoirradiation, but beyond initial formation of a <sup>1</sup>MLCT state, the electronic structure responsible for catalysis was not known until recent careful work from the Hadt laboratory.<sup>14</sup> The allowedness of the light-driven promotion of a Ni d<sub>yz</sub> electron into an unoccupied, high-lying bpy  $\pi^*$  orbital ultimately gives rise to an <sup>1</sup>MLCT state that undergoes intersystem crossing and then a final LMCT transition to cleave the Ni-C bond.<sup>12</sup> Still, characterization of the <sup>3</sup>LF state of the Ni(II)-bpy aryl halide complexes is important in understanding catalysis, particularly for disproving the null hypothesis. For example, synthesis of a covalently-linked aryl-bpy Ni(II)-bpy aryl halide complex turns off <sup>3</sup>LF formation, as that electronic state is not able to be stabilized via geometric distortion like in the prototypical example.<sup>15</sup> Yet still, similarly to the prototypical example, this tethered complex reacts with electrophile.<sup>15</sup> The electronic

structure of transition metal complexes can also be leveraged in order to gather mechanistic information about various reactivities.

### 1.3. Spin Relaxation

#### 1.3.1. $S = 1/2$ Molecules

The ground-state electronic structure of  $S = 1/2$  transition metal species is particularly important for understanding factors that give rise to spin relaxation. An ultimate goal of quantum information science is to achieve qubits with high-temperature coherence; minimizing spin relaxation rates is one manner in which that goal may be accomplished.<sup>16</sup> In an  $S = 1/2$  system, the Zeeman effect removes the degeneracy of the  $M_S = +1/2$  and  $M_S = -1/2$  in the presence of an externally-applied magnetic field (**Figure 1.2**). The transition between the lower-lying magnetic sublevel and the excited level gives rise to an “on” state that can be utilized for quantum information science applications.

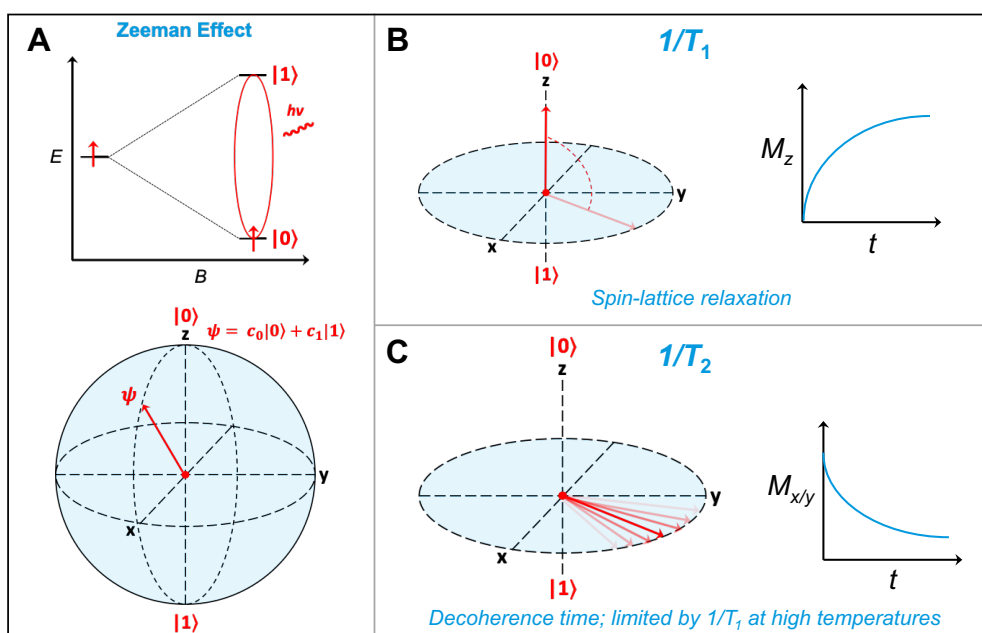


**Figure 1.2.** The Zeeman effect (A) as it relates to spin relaxation in an  $S = 1/2$  system. Spin relaxes longitudinally via spin-lattice relaxation (B) and in the  $xy$  plane via decoherence

( $T_2$ ) (C). At high temperatures where the best qubits operate,  $T_2$  is limited by  $T_1$ ;  $T_1$  is the most important metric for design principles at high temperatures.

Various electronic structure considerations may give rise to favorable qubit behavior for an  $S = 1/2$  qubit. For example, an unpaired electron in an orbital with less orbital angular momentum (e.g., a  $d_{z^2}$  orbital with  $m_l = 0$ ) may exhibit longer coherence times; an electron in an orbital with larger orbital angular momentum is predicted to relax faster via Spin Hamiltonian models.<sup>17</sup> Additionally, the unpaired electron may interact with the environment via spin-phonon coupling, which contributes to relaxation via specific symmetry rules.<sup>18</sup> So, careful consideration of the environment of the unpaired spin on a transition metal complex is necessary in order to develop the most robust qubits.

In this thesis, we investigate the symmetry of vibrational modes that may interact with the unpaired spin on copper porphyrin complexes and drive spin relaxation. Totally symmetric vibrational modes ( $a$ ) are symmetry-allowed contributors to  $1/T_1$ ,<sup>18</sup> and we spectroscopically confirm that the lower-energy, and hence more thermally accessible, vibrational modes with the proper symmetry led to faster relaxation in these model  $S = 1/2$  systems.<sup>19</sup>

### 1.3.2. $S = 1$ Molecules

While  $S = 1/2$  molecular systems have been extensively studied as qubit candidates, the necessity of large magnetic fields and very cold temperatures for quantitative spin polarization limits their applications.<sup>20</sup> However,  $S = 1$  systems may overcome this barrier by leveraging their zero-field splitting, which is borne from their triplet ground-state electronic configuration (**Figure 1.3**).<sup>21,22</sup> Despite this ability to achieve spin polarization at less extreme conditions, spin-lattice relaxation for  $S = 1$  species is typically quite fast, and coherence is usually lost at temperatures above 60 K.<sup>23</sup> Therefore, elucidating the mechanisms of relaxation in these optically-addressable qubit candidates is necessary in order to develop design principles to increase their coherence temperatures.

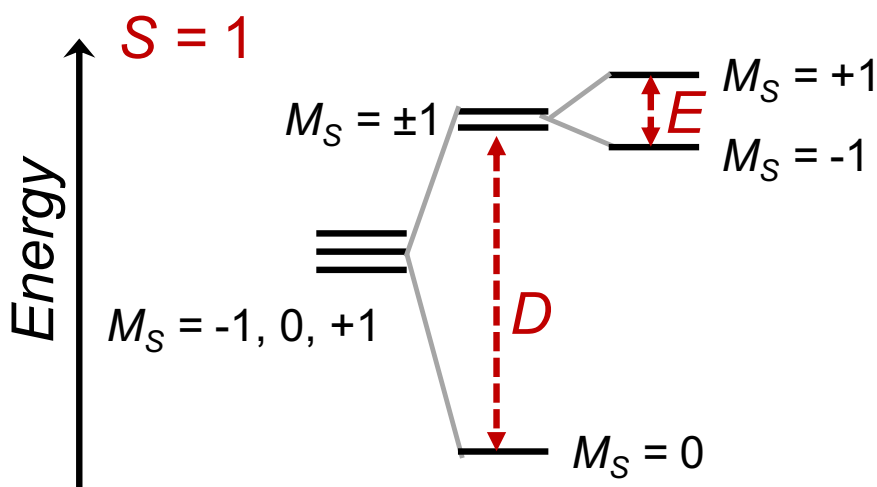


**Figure 1.3.** Zero-field splitting in the absence of a magnetic field for an  $S = 1$  complex. The ZFS term  $D$  refers to the axial ZFS parameter, and the ZFS term  $E$  refers to the rhombic ZFS value.

Herein, we leveraged variable-temperature and variable-field electron paramagnetic resonance (EPR) in order to decipher the mechanism of spin-lattice relaxation in an  $S = 1$  Cr(*o*-tolyl)<sub>4</sub> quantum bit candidate. We determined that low-energy (pseudo-)acoustic phonon interactions with the spins likely drove relaxation in this system.<sup>23</sup>

#### 1.4. Compound Scope

An overview of the transition metal complexes that are evaluated in this thesis is shown in **Figure 1.4**. These complexes span applications in catalysis and spin relaxation; their electronic structures are all key factors in understanding their utility.

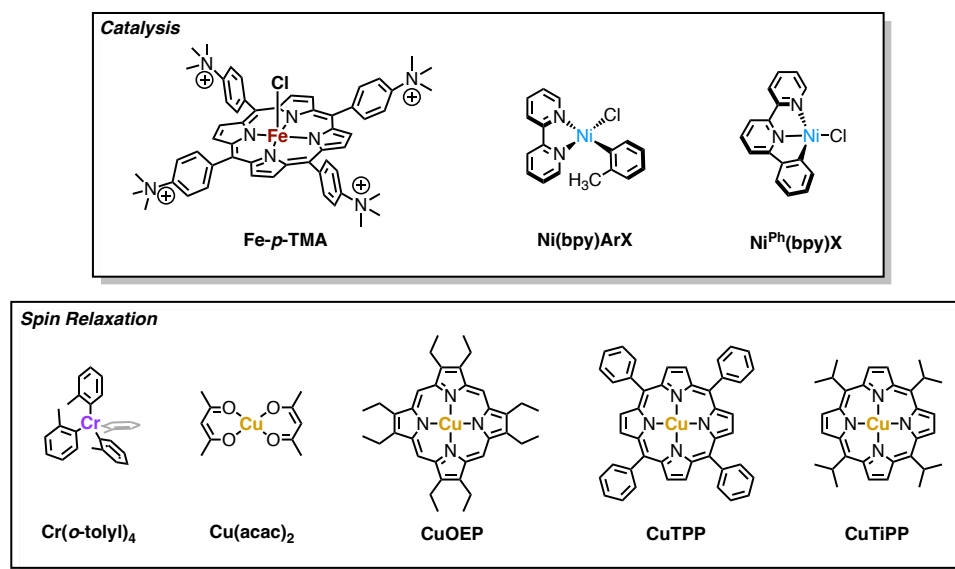


**Figure 1.4.** Molecules evaluated in this thesis

## 1.5. References

- (1) Boutin, E.; Merakeb, L.; Ma, B.; Boudy, B.; Wang, M.; Bonin, J.; Anxolabéhère-Mallart, E.; Robert, M. Molecular Catalysis of CO<sub>2</sub> Reduction: Recent Advances and Perspectives in Electrochemical and Light-Driven Processes with Selected Fe, Ni and Co Aza Macrocyclic and Polypyridine Complexes. *Chem. Soc. Rev.* **2020**, *49* (16), 5772–5809. <https://doi.org/10.1039/D0CS00218F>.
- (2) Boutin, E.; Robert, M. Molecular Electrochemical Reduction of CO<sub>2</sub> beyond Two Electrons. *Trends in Chemistry* **2021**, *3* (5), 359–372. <https://doi.org/10.1016/j.trechm.2021.02.003>.
- (3) Costentin, C.; Robert, M.; Savéant, J.-M.; Tatin, A. Efficient and Selective Molecular Catalyst for the CO<sub>2</sub> -to-CO Electrochemical Conversion in Water. *Proc. Natl. Acad. Sci. U.S.A.* **2015**, *112* (22), 6882–6886. <https://doi.org/10.1073/pnas.1507063112>.
- (4) Bonetto, R.; Crisanti, F.; Sartorel, A. Carbon Dioxide Reduction Mediated by Iron Catalysts: Mechanism and Intermediates That Guide Selectivity. *ACS Omega* **2020**, *5* (34), 21309–21319. <https://doi.org/10.1021/acsomega.0c02786>.
- (5) Römel, C.; Song, J.; Tarrago, M.; Rees, J. A.; van Gastel, M.; Weyhermüller, T.; DeBeer, S.; Bill, E.; Neese, F.; Ye, S. Electronic Structure of a Formal Iron(0)

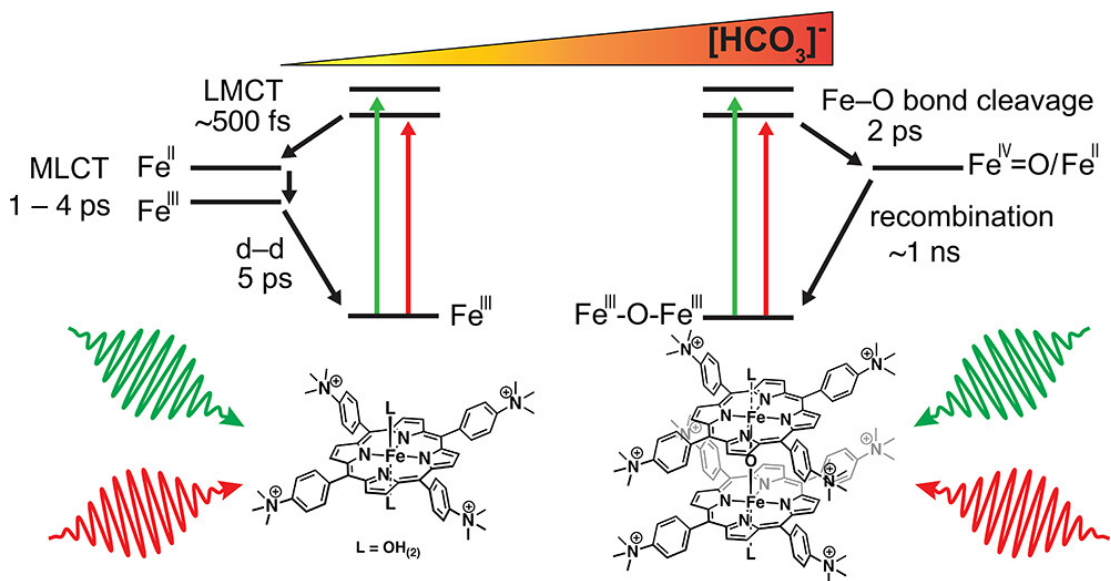
- Porphyrin Complex Relevant to CO<sub>2</sub> Reduction. *Inorg. Chem.* **2017**, *56* (8), 4745–4750. <https://doi.org/10.1021/acs.inorgchem.7b00401>.
- (6) Zhang, X.; Guo, S.-X.; Gandionco, K. A.; Bond, A. M.; Zhang, J. Electrocatalytic Carbon Dioxide Reduction: From Fundamental Principles to Catalyst Design. *Materials Today Advances* **2020**, *7*, 100074. <https://doi.org/10.1016/j.mtadv.2020.100074>.
- (7) Rao, H.; Schmidt, L. C.; Bonin, J.; Robert, M. Visible-Light-Driven Methane Formation from CO<sub>2</sub> with a Molecular Iron Catalyst. *Nature* **2017**, *548* (7665), 74–77. <https://doi.org/10.1038/nature23016>.
- (8) Nagel, R. L.; Gibson, Q. H. Kinetics of the Reaction of Carbon Monoxide with the Hemoglobin-Haptoglobin Complex. *Journal of Molecular Biology* **1966**, *22* (2), 249–255. [https://doi.org/10.1016/0022-2836\(66\)90130-6](https://doi.org/10.1016/0022-2836(66)90130-6).
- (9) Azcarate, I.; Costentin, C.; Robert, M.; Savéant, J.-M. Dissection of Electronic Substituent Effects in Multielectron–Multistep Molecular Catalysis. Electrochemical CO<sub>2</sub>-to-CO Conversion Catalyzed by Iron Porphyrins. *J. Phys. Chem. C* **2016**, *120* (51), 28951–28960. <https://doi.org/10.1021/acs.jpcc.6b09947>.
- (10) Follmer, A. H.; Luedecke, K. M.; Hadt, R. G.  $\mu$ -Oxo Dimerization Effects on Ground- and Excited-State Properties of a Water-Soluble Iron Porphyrin CO<sub>2</sub> Reduction Catalyst. *Inorg. Chem.* **2022**, *61* (50), 20493–20500. <https://doi.org/10.1021/acs.inorgchem.2c03215>.
- (11) Patra, S.; Ghosh, S.; Samanta, S.; Nayek, A.; Dey, A. Second Sphere Control of CO<sub>2</sub> Reduction Selectivity by Iron Porphyrins: The Role of Spin State. *Journal of Organometallic Chemistry* **2025**, *1023*, 123439. <https://doi.org/10.1016/j.jorganchem.2024.123439>.
- (12) Cagan, D. A.; Bím, D.; Silva, B.; Kazmierczak, N. P.; McNicholas, B. J.; Hadt, R. G. Elucidating the Mechanism of Excited-State Bond Homolysis in Nickel–Bipyridine Photoredox Catalysts. *J. Am. Chem. Soc.* **2022**, *144* (14), 6516–6531. <https://doi.org/10.1021/jacs.2c01356>.
- (13) Ting, S. I.; Garakyaraghi, S.; Taliaferro, C. M.; Shields, B. J.; Scholes, G. D.; Castellano, F. N.; Doyle, A. G. <sup>3</sup>d-d Excited States of Ni(II) Complexes Relevant to

- Photoredox Catalysis: Spectroscopic Identification and Mechanistic Implications. *J. Am. Chem. Soc.* **2020**, *142* (12), 5800–5810. <https://doi.org/10.1021/jacs.0c00781>.
- (14) Cagan, D. A.; Bím, D.; Kazmierczak, N. P.; Hadt, R. G. Mechanisms of Photoredox Catalysis Featuring Nickel–Bipyridine Complexes. *ACS Catal.* **2024**, *14* (11), 9055–9076. <https://doi.org/10.1021/acscatal.4c02036>.
- (15) Bím, D.; Luedecke, K. M.; Cagan, D. A.; Hadt, R. G. Light Activation and Photophysics of a Structurally Constrained Nickel(II)–Bipyridine Aryl Halide Complex. *Inorg. Chem.* **2024**, *63* (9), 4120–4131. <https://doi.org/10.1021/acs.inorgchem.3c03822>.
- (16) Wasielewski, M. R.; Forbes, M. D. E.; Frank, N. L.; Kowalski, K.; Scholes, G. D.; Yuen-Zhou, J.; Baldo, M. A.; Freedman, D. E.; Goldsmith, R. H.; Goodson, T.; Kirk, M. L.; McCusker, J. K.; Ogilvie, J. P.; Shultz, D. A.; Stoll, S.; Whaley, K. B. Exploiting Chemistry and Molecular Systems for Quantum Information Science. *Nat Rev Chem* **2020**, *4* (9), 490–504. <https://doi.org/10.1038/s41570-020-0200-5>.
- (17) Kazmierczak, N. P.; Xia, K. T.; Sutcliffe, E.; Aalto, J. P.; Hadt, R. G. A Spectrochemical Series for Electron Spin Relaxation. *J. Am. Chem. Soc.* **2025**, *147* (3), 2849–2859. <https://doi.org/10.1021/jacs.4c16571>.
- (18) Kazmierczak, N. P.; Hadt, R. G. Illuminating Ligand Field Contributions to Molecular Qubit Spin Relaxation via  $T_1$  Anisotropy. *J. Am. Chem. Soc.* **2022**, *144* (45), 20804–20814. <https://doi.org/10.1021/jacs.2c08729>.
- (19) Kazmierczak, N. P.; Lopez, N. E.; Luedecke, K. M.; Hadt, R. G. Determining the Key Vibrations for Spin Relaxation in Ruffled Cu(II) Porphyrins via Resonance Raman Spectroscopy. *Chem. Sci.* **2024**, *15* (7), 2380–2390. <https://doi.org/10.1039/D3SC05774G>.
- (20) Harvey, S. M.; Wasielewski, M. R. Photogenerated Spin-Correlated Radical Pairs: From Photosynthetic Energy Transduction to Quantum Information Science. *J. Am. Chem. Soc.* **2021**, *143* (38), 15508–15529. <https://doi.org/10.1021/jacs.1c07706>.
- (21) Drago, R. S.; Drago, R. S. *Physical Methods for Chemists*, 2nd ed.; Saunders College Pub: Ft. Worth, 1992.

- (22) Deaton, J. C.; Gebhard, M. S.; Solomon, E. I. Transverse and Longitudinal Zeeman Effect on [Tetraphenylphosphonium Tetrachloroferrate(1-)]: Assignment of the Ligand Field Transitions and the Origin of the 6A1 Ground-State Zero-Field Splitting. *Inorg. Chem.* **1989**, *28* (5), 877–889. <https://doi.org/10.1021/ic00304a016>.
- (23) Kazmierczak, N. P.; Luedecke, K. M.; Gallmeier, E. T.; Hadt, R. G.  $T_1$  Anisotropy Elucidates Spin Relaxation Mechanisms in an  $S = 1$  Cr(IV) Optically Addressable Molecular Qubit. *J. Phys. Chem. Lett.* **2023**, *14* (34), 7658–7664. <https://doi.org/10.1021/acs.jpcllett.3c01964>.

**PART I: CATALYSIS**

**CHAPTER 2:  $\mu$ -OXO DIMERIZATION EFFECTS ON GROUND- AND EXCITED-STATE PROPERTIES OF A WATER-SOLUBLE IRON PORPHYRIN CO<sub>2</sub> REDUCTION CATALYST**



Adapted with permission from:

Follmer, A. H.<sup>†</sup>; Luedecke, K. M.<sup>†</sup>; Hadt, R. G. “ $\mu$ -Oxo Dimerization Effects on a Ground- and Excited-State Properties of a Water-Soluble Iron Porphyrin CO<sub>2</sub> Reduction Catalyst.” *Inorg. Chem.* **2022**, *61* (50), 20493. DOI: 10.1021/acs.inorgchem.2c03215.

<sup>†</sup>Co-first author.

Copyright 2022 American Chemical Society.

## 2.1. Introduction

Iron tetraphenylporphyrin (FeTPP) complexes are well studied and versatile catalysts that can accomplish O<sub>2</sub> activation, H<sub>2</sub> evolution, and CO<sub>2</sub> reduction.<sup>1-4</sup> Particularly, FeTPP functionalized with trimethyl ammonium appendages at the phenyl *para* positions is both water soluble and electro/photochemically competent for the CO<sub>2</sub> reduction reaction (CO<sub>2</sub>RR). The Robert and Savéant groups have demonstrated the high stability and selectivity of iron 5,10,15,20-tetra(*para*-*N,N,N*-trimethylanilinium)porphyrin (Fe-*p*-TMA) in electro- and photochemical reduction of CO<sub>2</sub>. In both aqueous and organic solutions without a photosensitizer, Fe-*p*-TMA can reduce CO<sub>2</sub> to CO and ultimately to CH<sub>4</sub> in organic solutions upon addition of a photosensitizer.<sup>4-9</sup> These capabilities of Fe-*p*-TMA are suggested to arise from the electron-withdrawing nature of the NMe<sub>3</sub><sup>+</sup> groups that stabilize a key hypothesized catalytic intermediate, an Fe(0)-CO<sub>2</sub> adduct, via Coulombic interactions.<sup>6</sup> Additionally, the Lewis acidic groups positively shift the Fe<sup>I</sup>/Fe<sup>0</sup> couple, effectively lowering the overpotential and making the electrochemical CO<sub>2</sub>RR more favorable compared to other iron-porphyrin based systems.<sup>5</sup>

Although proposed catalytic cycles exist for the CO<sub>2</sub>RR by Fe-*p*-TMA, the precise identity of many intermediates involved in this conversion is unknown.<sup>4,8,9</sup> Previous reports describe the catalyst as monomeric when it enters the catalytic cycle, but it is well known that water-soluble iron porphyrins exhibit complex equilibria with propensities to form  $\mu$ -oxo diiron species (referred to herein as a  $\mu$ -oxo dimer for consistency with previous literature) depending on the pH and ionic strength of their aqueous solutions.<sup>10-16</sup> Indeed, high ionic strength conditions are invoked in both the electro- and photochemical CO<sub>2</sub>RR by Fe-*p*-TMA and other catalysts, particularly with metal bicarbonates (MHCO<sub>3</sub>, M = Na, K, Cs) employed as electrolytes.<sup>9,17</sup> Therefore, conditions that favor the CO<sub>2</sub>RR by Fe-*p*-TMA also favor its dimerization. However, the relevance of  $\mu$ -oxo dimer formation in the context of the photocatalytic conditions has not been expressed in previous reports.

Here, we utilize a combination of optical and magnetic spectroscopic techniques to characterize Fe-*p*-TMA and its complex, tunable equilibrium in aqueous conditions. Additionally, we leverage the ability to chemically control and spectrally address these

species and their photogenerated states via ultrafast transient absorption (TA) spectroscopy. We find that consideration of dimeric versus monomeric Fe-*p*-TMA has strong implications for the identities and lifetimes of the excited states generated in photocatalytically relevant solutions.

## 2.2. Results and Analysis

### 2.2.1. UV-vis Spectroscopy

Water-soluble iron porphyrins are known to undergo  $\mu$ -oxo dimer formation with increasing pH, ionic strength, and/or concentration.<sup>10-16,18</sup> As described further below, the presence of more than two absorption bands in the Q band region and a shoulder in the Soret band indicate that Fe-*p*-TMA exists as an equilibrium of species at dilute concentrations in low ionic strength and near-neutral pH solutions. Introduction of an electrolyte such as NaHCO<sub>3</sub>, which increases the ionic strength of the solution, initiates a decrease in intensity and a concomitant blue shift of the Soret peak (arrows in **Figure 2.1A**). This shift is accompanied by an increase in the intensity of the Q band at 564 nm and a decrease in the features near 650 nm (arrows in **Figure 2.1A**). These spectral changes are consistent with those observed in the formation of water-soluble  $\mu$ -oxo binuclear iron porphyrins.<sup>16,19-21</sup> As expected, increasing the concentration of bicarbonate leads to faster rates of  $\mu$ -oxo dimer formation and a greater overall concentration of this species (**Figures 2.1B** and **S6** and **Table S1**).

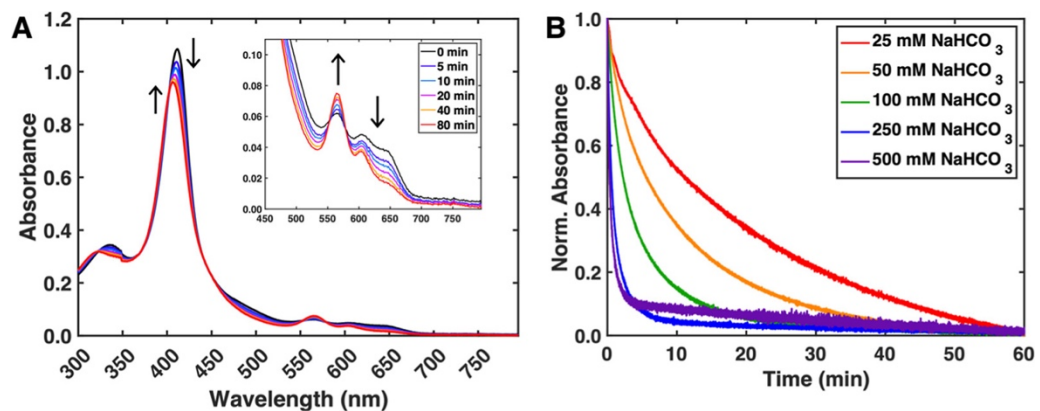


**Figure 2.1.** Bicarbonate-induced  $\mu$ -oxo dimer formation of Fe-*p*-TMA (pH  $\sim$  8.3). **(A)** Evolution of the Fe-*p*-TMA steady-state absorption spectrum upon addition of 50 mM NaHCO<sub>3</sub>. Inset: Q band region. **(B)** Normalized kinetic traces of  $\mu$ -oxo dimer formation as a function of [NaHCO<sub>3</sub>] monitored at 412 nm

Bicarbonate is a buffering electrolyte and therefore affects both the pH and ionic strength of the Fe-*p*-TMA solutions. To disambiguate these effects, solutions were prepared using different metal bicarbonates, nonbuffering electrolytes, and across a wide range of pH values. The UV-vis spectra of Fe-*p*-TMA in the presence of different MHCO<sub>3</sub> identities (M = Na, K, Cs) commonly employed in the CO<sub>2</sub>RR are indistinguishable and support that the origin of the  $\mu$ -oxo dimerization is an effect induced by the bicarbonate anion (**Figure 2.2A**).

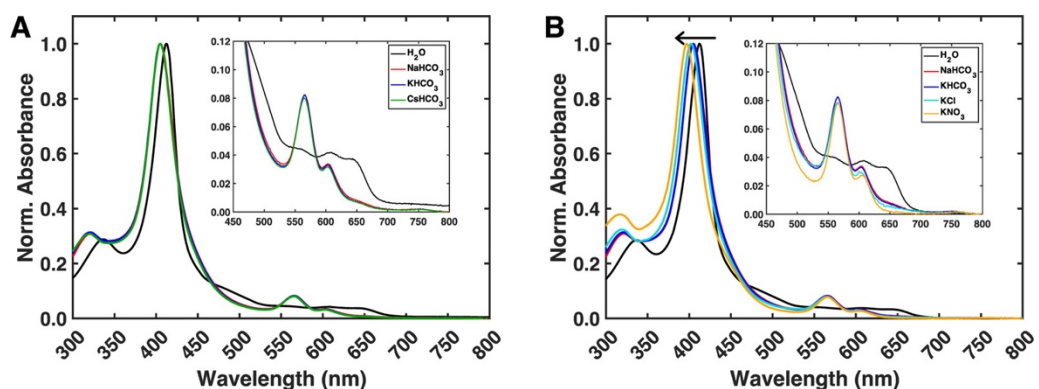


**Figure 2.2.** **(A)** Normalized steady-state absorption spectra of Fe-*p*-TMA in H<sub>2</sub>O and 500 mM MHCO<sub>3</sub> solutions (M = Na, K, Cs). Inset: Q band region. **(B)** Normalized steady-state absorption spectra of Fe-*p*-TMA in various electrolyte conditions. Insets: Q band region

Non-buffering electrolytes such as KCl and KNO<sub>3</sub> induce similar effects on the steady-state absorption spectrum as with the addition of MHCO<sub>3</sub> (**Figure 2.2B**). However, the positions of their respective Soret bands are shifted to higher energies. Both the Soret and Q bands arise from porphyrin-centered  $\pi$ - $\pi^*$  transitions that mix with frontier metal d-orbitals upon metalation.<sup>22</sup> Therefore, these transitions are highly sensitive to factors

that alter the porphyrin structure and/or metal spin/oxidation states, such as the presence of axial ligands and solvent identity. However, interestingly, in the absorption spectra of Fe-*p*-TMA, the energy of the Q bands remains unchanged, while the position of the Soret shifts in different electrolyte solutions following the trend in anion:  $\text{OH}^- < \text{HCO}_3^- < \text{Cl}^- < \text{NO}_3^-$  (arrow in **Figure 2.2B**).

Varying the pH of Fe-*p*-TMA solutions results in three different UV-vis profiles that correspond to distinct speciation in three pH regimes:  $<4.5$ ,  $4.5-12$ , and  $>12$  (**Figure 2.3**). The effects of pH on water-soluble porphyrins have been extensively studied, and Fe-*p*-TMA displays similar behavior.<sup>14,15,18,19</sup> In nonbuffered conditions, aqueous Fe<sup>III</sup> porphyrin systems exist as (1) monomeric in acidic conditions ( $\text{pH} < 4.5$ ), (2) predominately dimeric in basic conditions ( $\text{pH} > 12$ ), and (3) a mixture of monomer and dimer at intermediate pH ranges. At  $\text{pH} < 4.5$ , we observe multiple monomeric populations with overlapping Soret bands (**Figure 2.3A**). Literature assignments of other water-soluble iron-based porphyrin systems suggest that in acidic pH solutions ( $<4.5$ ), the Soret feature has an intense maximum that describes the absorbance of a monoaqua-ligated metalloporphyrin with a shoulder that describes the symmetric six-coordinate diaqua-ligated monomer.<sup>19</sup> As pH approaches neutral conditions, the Soret red-shifts and the Q band region becomes consistent with an equilibrium between one monomeric species and a  $\mu$ -oxo dimeric species. At very basic pH values ( $>12$ ), the monomer/dimer equilibrium remains, but the growth of a new feature in the Q band region ( $\sim 650$  nm) is attributed to a unique hydroxy-ligated monomer.<sup>19</sup> In 500 mM  $\text{NaHCO}_3$ , the same trends hold, except that at pHs 4–12, the monomer/dimer equilibrium strongly favors the  $\mu$ -oxo dimer (**Figure 2.3B**). However, at high pH values, the growth of a 650 nm feature supports the assignment of a new monomeric species as well.

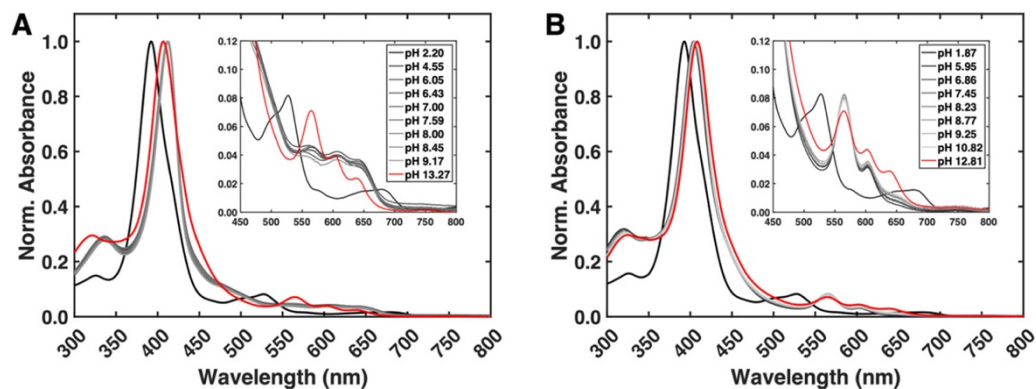


**Figure 2.3.** pH titrations of Fe-*p*-TMA in H<sub>2</sub>O (A) and at a constant ionic strength (500 mM NaHCO<sub>3</sub>) (B). Insets: Q band region. Spectra have been normalized to the maximum intensity of the Soret. pH was modulated with the addition of NaOH/HCl.

### 2.2.2. EPR and MCD Spectroscopy

Electron paramagnetic resonance (EPR) spectroscopy reveals a marked difference in the magnetic spectra of Fe-*p*-TMA solutions depending on the electrolyte (**Figure 2.4**). The 5 K continuous wave (CW) EPR signal in 50/50 H<sub>2</sub>O/glycerol glass is axial with features  $g_{x,y} = \sim 6$  and  $g_z = \sim 2$ , indicating a high-spin Fe<sup>III</sup>  $S = 5/2$  ground state (**Figure S10**). Since samples were frozen as glasses, it is possible that they could undergo a change in speciation upon freezing. However, across all spectra that contained an additional electrolyte, there is a common loss of spectral intensity despite identical Fe-*p*-TMA concentrations. This intensity loss is attributed to  $\mu$ -oxo dimer formation and resultant antiferromagnetic coupling between the two Fe<sup>III</sup> centers.<sup>23</sup> The remaining signal intensity is attributed to residual monomer population. Additionally, while Fe-*p*-TMA in KCl solutions exhibits the expected loss of spectral intensity, only the species in NaHCO<sub>3</sub> and basic solution induce significant changes in rhombicity.

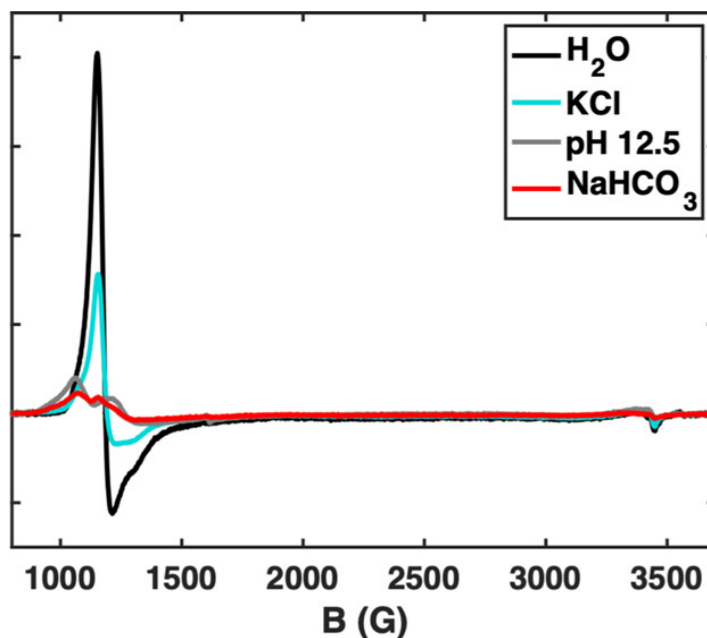


**Figure 2.4.** 5 K X-band CW EPR spectra of Fe-*p*-TMA with various 500 mM electrolyte additives and pH conditions

To corroborate the assignment of the UV–vis spectra of the monomeric and  $\mu$ -oxo dimer species, we employed room-temperature magnetic circular dichroism (MCD) spectroscopy taken at 1.4 T. The MCD spectra are consistent with previous spectra obtained for different speciations of FeTPPCl and FeTMPyP, including their  $\mu$ -oxo forms.<sup>24-27</sup> The MCD spectra exhibit dispersion-type A terms with energies consistent with their steady-state absorption spectra/bands (dashed lines in **Figure 2.5**). As A terms are associated with degenerate excited states, we conclude that the lowest unoccupied molecular orbitals (LUMOs) are degenerate and are interpretable through the Gouterman-type four-orbital model of porphyrin absorption spectra. Additionally, the MCD spectra only display differential absorption near 650 nm ( $\sim 15,000$   $\text{cm}^{-1}$ ) in water alone (i.e., for the monomeric species). Like the absorption spectra, when bicarbonate is present and  $\mu$ -oxo Fe-*p*-TMA is favored, this feature decreases dramatically (**Figure 2.5**).

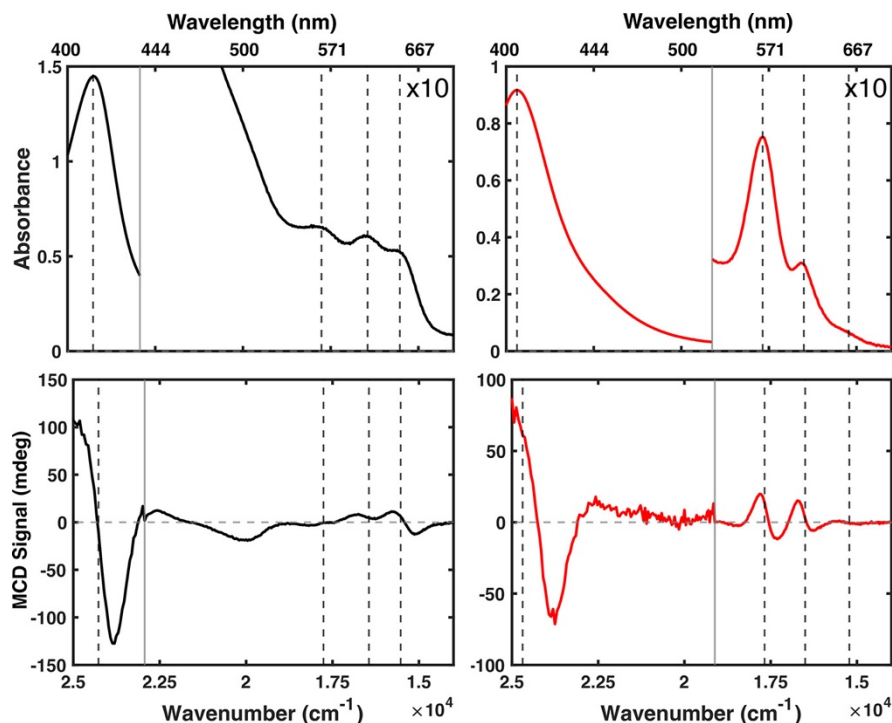


**Figure 2.5.** Top: Electronic absorption spectra of 50  $\mu\text{M}$  Fe-*p*-TMA in  $\text{H}_2\text{O}$  (left) and 500 mM  $\text{NaHCO}_3$  (right). The Q band region is scaled for a 10 $\times$  dilution factor consistent with the 50  $\mu\text{M}$  (Soret) and 5  $\mu\text{M}$  (Q band) MCD samples. Bottom: MCD spectra (1.4 T) of Fe-*p*-TMA in water (left) and 500 mM (50 mM)  $\text{NaHCO}_3$  (right)

### 2.2.3. Ultrafast TA Spectroscopy

Direct photoexcitation of Fe-*p*-TMA at  $\lambda_{\text{exc.}} > 420$  nm has been demonstrated to result in the  $\text{CO}_2\text{RR}$ .<sup>4,8,9,28,29</sup> As these reports utilize  $\text{MHCO}_3$  to perform catalysis, we studied the impact of the addition of  $\text{MHCO}_3$  species on the photodynamic properties of Fe-*p*-TMA. Given the ability to discern between the monomer and dimer species in the steady-state absorption profiles of the Q band region ( $\sim 470$ – $700$  nm) (**Figure 2.6**), we performed a wavelength-dependence study using ultrafast TA spectroscopy to delineate the excited-state behavior of these two species. Differences in relaxation rates between  $\text{MHCO}_3$  ( $\text{M} = \text{Na, K, Cs}$ ) solutions were not observed within error (**Figures S12–S26**).

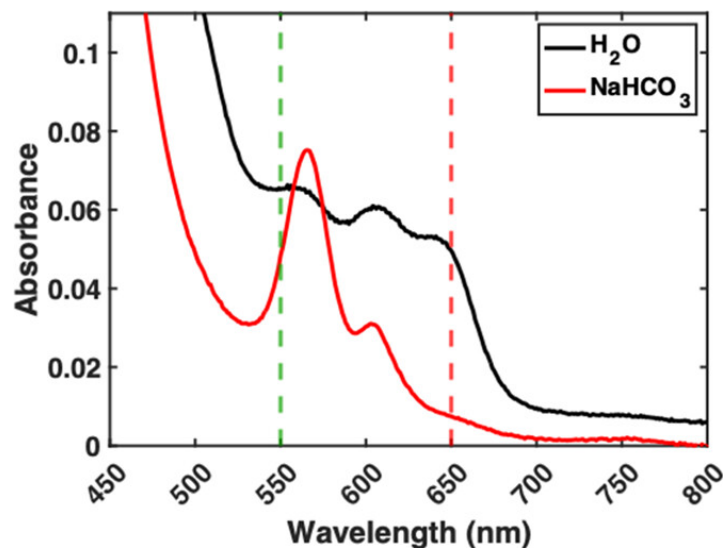


**Figure 2.6.** Excitation wavelengths ( $\lambda_{\text{exc.}} = 550$  and  $650$  nm) noted on steady-state absorption spectra of Fe-*p*-TMA in H<sub>2</sub>O and 500 mM NaHCO<sub>3</sub> solutions. The species in water is best described as an equilibrium of monomer and  $\mu$ -oxo dimer, whereas NaHCO<sub>3</sub> is predominantly  $\mu$ -oxo dimer. The width of the pump scatter is  $\sim 20$  and  $\sim 30$  nm on either side of the central wavelength of excitation for 550 and 650 nm, respectively.

The steady-state absorption profiles of the monomeric and MHCO<sub>3</sub>-induced  $\mu$ -oxo dimeric species display Soret energies ranging from 412 to 407 nm, respectively, which is a function of the interplay of both increased dimer population and perturbed dielectric of the surrounding solution due to the addition of MHCO<sub>3</sub> (*vide infra*). Further, the absorption band at 650 nm is nearly absent in conditions where dimer formation is preferred (i.e., in the presence of bicarbonate and other electrolytes). Note that this band does go away entirely for the dimer species upon addition of KNO<sub>3</sub> (**Figure 2.2B**). This band therefore provides a spectrally addressable, monomer-associated feature, while the blue shifting of the Soret band/ground-state bleach in the TA data provides a handle for the discernment of excited-state dynamics associated with monomeric and  $\mu$ -oxo dimeric species.

Relaxation of monomeric Fe-*p*-TMA after photoexcitation at 650 nm in neutral pH H<sub>2</sub>O was best fit to a three-component sequential model (**Figure 2.7**). With  $\tau_1 = \sim 333$  fs,  $\tau_2 = 1.44$  ps, and  $\tau_3 = 4.66$  ps, Fe-*p*-TMA exhibits a relaxation process analogous to those

previously described for FeTPP and FeTMPyP monomers.<sup>30,31</sup> The energy of the ground-state bleach near 412 nm in each of the evolution-associated spectra (EAS) is consistent with its steady-state absorption profile (**Figures 2.2 and 2.8**). To support this monomeric assignment in H<sub>2</sub>O with  $\lambda_{\text{exc.}} = 650$  nm, we collected TA data of acid-induced monomeric Fe-*p*-TMA (**Figure S35**). While the spectral profiles for these two samples differ slightly due to differences in monomeric speciation, the lifetimes of the components are comparable.

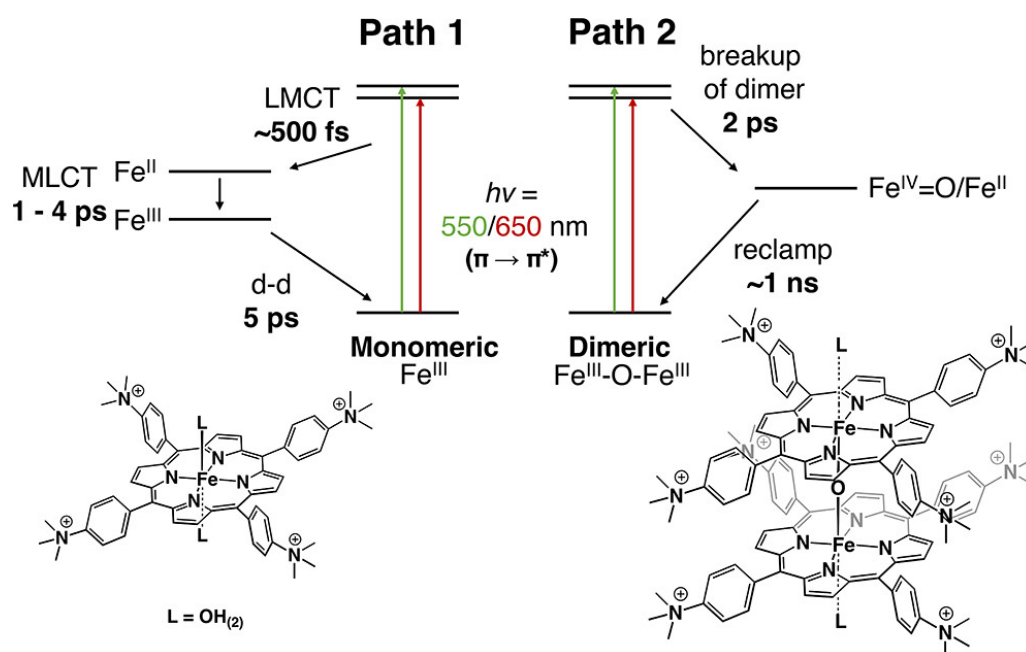


**Figure 2.7.** Proposed mechanisms of Fe-*p*-TMA relaxation after photoexcitation into the Q band region for the monomeric and dimeric forms. In conditions where an equilibrium of monomeric and dimeric species exists, that is, in H<sub>2</sub>O at mild pH values, both relaxation pathways occur. The oxidation state of the iron centers is depicted at each intermediate state.

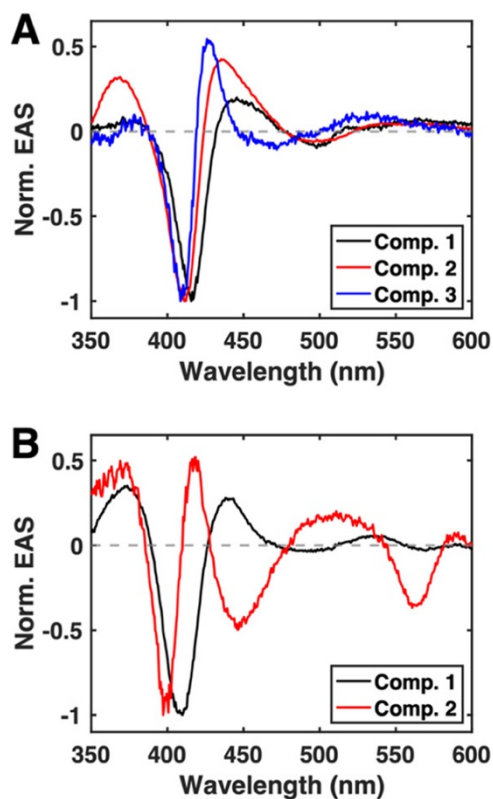


**Figure 2.8.** Normalized EAS profiles of Fe-*p*-TMA in H<sub>2</sub>O (A) of a three-component sequential model ( $\tau_1 = 333$  fs,  $\tau_2 = 1.44$  ps, and  $\tau_3 = 4.66$  ps) and 500 mM NaHCO<sub>3</sub> solution (B), which is best fit to a two-component sequential model ( $\tau_1 = 2.04$  ps and  $\tau_2 = \sim 1$  ns). The excitation wavelength is  $\lambda_{\text{exc.}} = 650$  nm.

On the other hand, the addition of MHCO<sub>3</sub> to solutions of Fe-*p*-TMA drastically alters the observed photodynamics. Under these conditions, the  $\mu$ -oxo dimer form is prevalent, and the difference spectra are best fit to a two-component sequential model with  $\tau_1 = 2$  ps and  $\tau_2 = \sim 1$  ns (**Figures 2.7 and 2.8**). The lifetimes and differential TA profiles of the Fe-*p*-TMA  $\mu$ -oxo dimer agree well with previous reports of both covalently tethered (Pacman) and nontethered Fe<sup>III</sup>- $\mu$ -oxo-Fe<sup>III</sup> porphyrin systems.<sup>32,33</sup> In these reports, excitation at multiple wavelengths results in the cleavage of a Fe<sup>III</sup>-O bond and generates transient Fe<sup>IV</sup>=O and Fe<sup>II</sup> porphyrin species ( $\tau_1 < 20$  ps) that then recombine (or, reclamp) to reform the ground-state dimer ( $\tau_2 = \sim 1$  ns). The EAS profile of component 2 representing the Fe<sup>IV</sup>=O/Fe<sup>II</sup> state should therefore consist of positive features due to the

formation of the  $\text{Fe}^{\text{IV}}=\text{O}$  and  $\text{Fe}^{\text{II}}$  species combined with the depletion or subtraction of the dimer spectrum (**Figure 2.8B**). Indeed, we observe a negative band at 560 nm consistent with the ground-state bleach of the dimer. The ground state dimer spectrum also displays strong positive absorption in the  $\sim 450$  nm range, which presents as a negative feature in the TA profile. In combination with a positive absorption at shorter wavelengths, the difference spectrum presents as a negative band at 450 nm. Together with positive features that may be attributed to  $\text{Fe}^{\text{IV}}=\text{O}$  and  $\text{Fe}^{\text{II}}$  species at 420 nm, a broad absorption  $\sim 510$  nm, and smaller absorption at  $\sim 590$  nm, the spectra become identical to that of a well-characterized  $\text{Fe}^{\text{IV}}=\text{O}/\text{Fe}^{\text{II}}$  state,<sup>34</sup> as depicted in **Figure S1** of ref. 34. These bands are distinct from those found in the water alone.

We also performed TA spectroscopy with  $\lambda_{\text{exc.}} = 550$  nm, where both monomeric and dimeric populations absorb with nearly equal intensity (**Figure 2.6**). Here, the bicarbonate concentration-dependent photodynamics provided important information about the nature of the second relaxation component. Not only does this lifetime increase upon the increasing concentration of  $\text{MHCO}_3$  but is also associated with a flattening of the excited-state absorption feature centered around 430 nm in the EAS profiles (**Figure 2.9B**). Rury and Sension attributed their  $\tau_2$  with similar lifetimes to a charge-transfer event,<sup>30</sup> and, similarly, Williams and Knappenberger noted a charge transfer  $\tau_2$  having a dielectric dependence in an FeTMPyP system.<sup>31</sup> In an acid-induced monomeric FeTMPyP system, an increase in  $\tau_2$  was observed by decreasing the dielectric constant of the solution.<sup>31</sup> We observe the same so-called dielectric effect on our  $\tau_2$ : increasing the concentration of  $\text{MHCO}_3$  (i.e., decreasing the dielectric constant of solution) leads to a prolonged  $\tau_2$  lifetime for the monomeric population (**Figure 2.9D**).

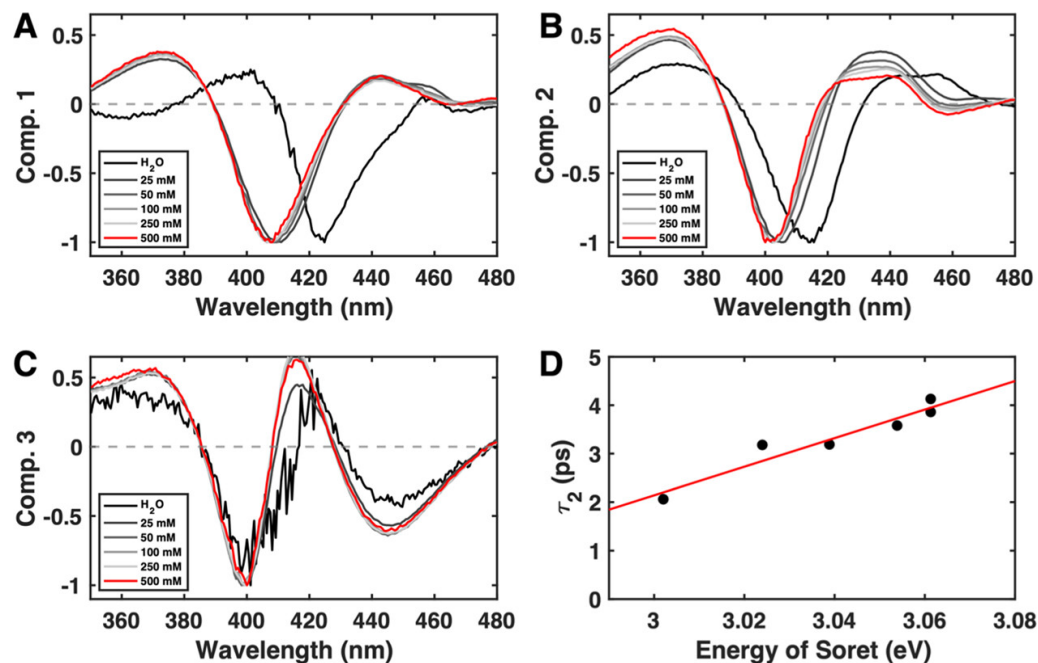


**Figure 2.9.** Normalized EAS profiles of Fe-*p*-TMA in H<sub>2</sub>O and NaHCO<sub>3</sub> solutions with  $\lambda_{\text{exc.}} = 550$  nm from a three-component sequential model. (A) EAS component 1 ( $\tau_1 = \sim 500$  fs), (B) EAS component 2 ( $\tau_2 = 2\text{--}4$  ps), (C) EAS component 3 ( $\tau_3 = \sim 1$  ns), and (D)  $\tau_2$  dependence on the position of the steady-state Soret band. With the increasing concentration of NaHCO<sub>3</sub>, the  $\tau_2$  excited-state lifetime increases, the EAS profiles flatten in the 430 nm region, and the energy of the steady-state Soret band blue-shifts to higher energy.

### 2.3. Discussion

Previous reports have investigated Fe-*p*-TMA as an efficient electro- and photocatalyst for the CO<sub>2</sub>RR.<sup>4,8,9,28,29</sup> In these reports, the resting state of the catalyst is proposed to be monomeric. However, we found that Fe-*p*-TMA speciation is sensitive to its chemical microenvironment. Consequently, in conditions reported for aqueous CO<sub>2</sub>RR, the catalyst exists predominantly as a  $\mu$ -oxo porphyrin dimer in its resting state. Since the CO<sub>2</sub>RR was demonstrated by direct irradiation of Fe-*p*-TMA at  $\lambda_{\text{exc.}} > 420$  nm and both monomeric and  $\mu$ -oxo dimeric porphyrins display absorption in this region, we utilized optical and magnetic spectroscopic techniques to characterize these monomeric and  $\mu$ -oxo dimeric species in their ground and excited states. We demonstrate the equilibrium that dictates

that speciation depends strongly on the pH and ionic strength of solution, and the achievable photochemical pathways of each species are altered accordingly.

Given this propensity for  $\text{MHCO}_3$  to induce  $\mu$ -oxo dimer formation in aqueous solutions and that direct photoexcitation of Fe-*p*-TMA in the presence of  $\text{MHCO}_3$  at  $\lambda_{\text{exc.}} > 420$  nm has been shown to accomplish the  $\text{CO}_2\text{RR}$ , we sought to study the tunable photodynamic properties of Fe-*p*-TMA. The monomer and  $\mu$ -oxo dimer species are discernible in the steady-state Q band region (470–700 nm) (**Figure 2.6**). Specifically, the excited-state behavior of monomeric and  $\mu$ -oxo dimeric populations of Fe-*p*-TMA was delineated using ultrafast TA spectroscopy by leveraging their differential absorption at 650 nm. This feature is attributed to a monomeric population.

In catalytically relevant conditions (i.e., in the presence of an electrolyte, particularly  $\text{MHCO}_3$ ), the resting state of Fe-*p*-TMA is dominated by its  $\mu$ -oxo dimeric form. Indeed, the formation of this  $\mu$ -oxo binuclear species is favored and fortified with increasing ionic strength. Increasing the pH from acidic (pH  $\sim$  4) to basic (pH  $>$  12) results in spectral changes similar to those associated with increasing ionic strength (**Figures 2.3** and **S2**). However, in addition to observing substantial dimeric population in the steady-state absorption spectra at pH  $>$  12, a new spectral feature appears at 650 nm that we attribute to a new monomeric species.

It is also observed that the energy difference between the Soret and the Q bands for the  $\mu$ -oxo binuclear species increases as the anion identity of the electrolyte is modulated from  $\text{OH}^-$  to  $\text{HCO}_3^-$  to  $\text{Cl}^-$  to  $\text{NO}_3^-$  (**Figure 2.2B**). This trend likely indicates a change in the solvation environment about the catalyst (e.g., pH or ionic strength) rather than axial ligand exchange, as one would expect simultaneous changes in the position and intensity of the Soret and Q bands upon a change in the primary coordination sphere.<sup>35</sup> Given the positive charge of the peripheral appendages of Fe-*p*-TMA, it is likely that the unique association of these anions with the TMA groups results in these observed differences. The trend in the Soret energies ( $\text{OH}^- < \text{HCO}_3^- < \text{Cl}^- < \text{NO}_3^-$ ) is consistent with decreasing anion basicity. Therefore, it is possible that, as the Lewis basicity of the anionic electrolyte is increased, the electrostatic interaction of the anion with the positive peripheral TMA charges is greater, and, therefore, the stronger base screens the positive porphyrin-based

charges more. Consequently, the energy of the  $\pi$ - $\pi^*$ -based Soret band decreases (i.e., higher  $\lambda_{\text{Soret}}$  wavelength) as a function of the screening ability of the anion. This electrostatic argument is one potential description of the experimental data, but whether the energy shifts arise from electron-withdrawing and/or porphyrin ring distortions is currently unclear. It is also unclear at this point as to whether or not this potential screening will manifest in the relative stabilities of the CO<sub>2</sub>RR intermediates (e.g., the Fe(0)-CO<sub>2</sub> adduct).

CW EPR spectroscopy also reveals changes in the Fe-*p*-TMA ground state upon the addition of different electrolytes. While there is a marked decrease in intensity due to the formation of  $\mu$ -oxo dimers with antiferromagnetically coupled iron centers, the observed intensity of these spectra arises from residual monomeric populations with high-spin ground states ( $S = 5/2$ ). The unique changes in rhombicity between these samples likely reflect perturbations to either the electronic structure and/or geometry of the porphyrin ring, which supports the conclusion that the anionic electrolytes are interacting with the TMA substituents. Further, the spectral profile of the residual monomeric population of Fe-*p*-TMA in the presence of KCl closely resembles the population in H<sub>2</sub>O alone. However, it is interesting to note that in the presence of MHCO<sub>3</sub>, which enhances Fe-*p*-TMA's catalytic capabilities,<sup>17</sup> the EPR signal of the complex exhibits a distinctly more rhombic profile.

Characterization of the ultrafast photodynamics of monomeric iron porphyrins has been performed on complexes such as FeTPP in organic solvents and the water-soluble FeTMPyP complex.<sup>30,31</sup> In those systems, excitation into either the Soret and/or Q bands leads to excited-state dynamics that are best described by a three-component sequential model. These components are attributed to ligand-to-metal charge transfer (LMCT), followed by a metal-to-ligand charge transfer (MLCT), and then a d-d transition with an inferred spin-flip. All of these dynamics are complete in less than 20 ps. In contrast, covalently tethered and noncovalent  $\mu$ -oxo dimeric iron porphyrin species studied by flash photolysis exhibit excited-state dynamics with lifetimes extending to the nanosecond timescale.<sup>33</sup> In these systems, the initial dimer species undergoes a homolytic Fe<sup>III</sup>-O bond cleavage that leads to the formation of transient Fe<sup>IV</sup>=O and Fe<sup>II</sup> monomeric species. The

high-valent photogenerated intermediate can go on to oxidize a variety of substrates. However, if this process is unproductive, that is, in the absence of a substrate, then the transient species ultimately recombine to reform the  $\mu$ -oxo dimeric ground state.<sup>34,36</sup>

Here, Fe-*p*-TMA was found to undergo relaxation processes best described by three- and two-component sequential models for monomeric and  $\mu$ -oxo dimeric species, respectively. Akin to the relaxation paths reported for FeTPP and FeTMPyP monomers,<sup>30,31</sup> Fe-*p*-TMA monomers undergo LMCT, MLCT, and subsequent relaxation from a ligand field excited state in less than 20 ps. This relaxation mechanism was confirmed by tuning the equilibrium with pH (acidic, 3.58) to favor monomeric species and repeating the TA measurements. These monomer-favoring conditions displayed nearly identical relaxation lifetimes to those found when probing the monomer at neutral pH (**Figures S28** and **S35**). The  $\mu$ -oxo dimer form, on the other hand, was best fit to a two-component sequential model, where cleavage of an Fe<sup>III</sup>-O bond generates transient Fe<sup>IV</sup>=O and Fe<sup>II</sup> porphyrin monomers ( $\tau_1 = 2$  ps) that recombine to the ground-state  $\mu$ -oxo dimer ( $\tau_2 = \sim 1$  ns). The assignment of this long-lived Fe<sup>IV</sup>=O/Fe<sup>II</sup> monomer pair is supported by the spectral similarity to previous reports for covalently and noncovalently linked Fe-porphyrin complexes (**Table 2.1** and **Figure S1** in reference 34).

**Table 2.1.** Lifetimes Obtained by Global Fitting<sup>a</sup>

Fe- <i>p</i> -TMA	$\tau_1$	$\tau_2^*$	$\tau_3$
monomer	$\sim 500$ fs	2-4 ps	5 ps
$\mu$ -oxo dimer	2 ps	1 ns	–

<sup>a</sup>For the monomeric form,  $\tau_1$  and  $\tau_2$  values were obtained from fits of  $\lambda_{\text{exc.}} = 550$  nm data, and  $\tau_3$  was extracted from  $\lambda_{\text{exc.}} = 650$  nm data. \* $\tau_2$  of the monomer relaxation describes a charge-transfer process that is dependent on [MHCO<sub>3</sub>] (longer lifetimes with higher concentration). Dimer lifetimes were obtained from fits of  $\lambda_{\text{exc.}} = 650$  nm data.

The timescale for recombination to regenerate the  $\mu$ -oxo dimer is sufficiently long to allow for the Fe<sup>IV</sup>=O or Fe<sup>II</sup> porphyrin species to exhibit reactivity. For example, photoexcitation of other  $\mu$ -oxo iron porphyrin systems has resulted in catalytic oxidation

of olefins and sulfides.<sup>36</sup> In that same vein, this prolonged excited state of the Fe-*p*-TMA dimeric species may help explain the enhanced photocatalyzed CO<sub>2</sub>RR in aqueous conditions. Further studies are needed to investigate the role of the  $\mu$ -oxo species in the context of this mechanism.

The overlapping absorption at 550 nm was also utilized to assign the identity of the second component of the monomeric relaxation path as MLCT in origin.  $\tau_2$  found here is highly sensitive to the concentration of MHCO<sub>3</sub>. Decreasing the dielectric constant of the solution leads to a prolonged  $\tau_2$  lifetime for the monomeric population and can be related back to the blue shift in the energy of the Soret band (**Figure 2.9D**). Despite our excitation into the Q band manifold, longer  $\tau_2$  lifetimes correspond to higher-energy Soret positions and are associated with higher ionic strength (lower dielectric) conditions. These comparisons support our conclusion that the identity of the first two relaxation events upon excitation of Fe-*p*-TMA at 550 nm can be modeled as monomer-based LMCT and subsequent MLCT processes. It is currently unclear why the LMCT component does not exhibit ionic strength dependence. It should also be noted that the third component of the data collected at 550 nm (**Figure 2.9C**) does not agree with the monomer-based model but rather is consistent with the second component of  $\mu$ -oxo dimeric relaxation (**Figure 2.8B**), reflecting the excitation of both species at this wavelength.

## 2.4. Conclusions

This study has demonstrated the existence of a complex equilibrium between mononuclear and  $\mu$ -oxo dimeric species in the precatalytic form of a water-soluble iron porphyrin, Fe-*p*-TMA, which is capable of carrying out the CO<sub>2</sub>RR. It is demonstrated how conditions used to perform catalysis with Fe-*p*-TMA favor  $\mu$ -oxo dimer formation. Further, as one may expect, the photodynamic pathways accessible to monomeric versus  $\mu$ -oxo dimeric species are distinct. It is found that Fe-*p*-TMA forms  $\mu$ -oxo dimers in the presence of bicarbonate and that the dimeric form exhibits similar excited-state dynamics to previously characterized  $\mu$ -oxo binuclear iron porphyrin systems used in oxidative chemistry (i.e., Fe<sup>IV</sup>=O or Fe<sup>II</sup> porphyrin species). Using a unique low-energy absorption feature attributed to a monomeric species, the excited-state dynamics of monomer and  $\mu$ -oxo

dimer species were differentiated. Monomeric Fe-*p*-TMA, regardless of environmental conditions, displayed relaxation dynamics that were complete within 10 ps and were consistent with a three-step relaxation found for other Fe<sup>III</sup> porphyrin complexes. The assignment of the second state (MLCT) was supported by the bicarbonate dependence of its excited-state profile and lifetime. In this study, optical and magnetic spectroscopic techniques were leveraged to identify and characterize chemical microenvironment effects on the distinct speciation in the ground and excited states of an iron porphyrin CO<sub>2</sub>RR catalyst.

## 2.5. References

- (1) Bhugun, I.; Lexa, D.; Savéant, J.-M. Homogeneous Catalysis of Electrochemical Hydrogen Evolution by Iron(0) Porphyrins. *J. Am. Chem. Soc.* **1996**, *118*, 3982–3983, DOI: 10.1021/ja954326x.
- (2) Costentin, C.; Dridi, H.; Savéant, J.-M. Molecular Catalysis of O<sub>2</sub> Reduction by Iron Porphyrins in Water: Heterogeneous versus Homogeneous Pathways. *J. Am. Chem. Soc.* **2015**, *137*, 13535–13544, DOI: 10.1021/jacs.5b06834.
- (3) Zou, L.; Sa, R.; Lv, H.; Zhong, H.; Wang, R. Recent Advances on Metalloporphyrin-Based Materials for Visible-Light-Driven CO<sub>2</sub> Reduction. *ChemSusChem* **2020**, *13*, 6124, DOI: 10.1002/cssc.202001796.
- (4) Rao, H.; Schmidt, L. C.; Bonin, J.; Robert, M. Visible-Light-Driven Methane Formation from CO<sub>2</sub> with a Molecular Iron Catalyst. *Nature* **2017**, *548*, 74–77, DOI: 10.1038/nature23016.
- (5) Costentin, C.; Robert, M.; Savéant, J.-M.; Tatin, A. Efficient and Selective Molecular Catalyst for the CO<sub>2</sub> -to-CO Electrochemical Conversion in Water. *Proc. Natl. Acad. Sci. U.S.A.* **2015**, *112*, 6882–6886, DOI: 10.1073/pnas.1507063112.
- (6) Azcarate, I.; Costentin, C.; Robert, M.; Savéant, J.-M. Through-Space Charge Interaction Substituent Effects in Molecular Catalysis Leading to the Design of the Most Efficient Catalyst of CO<sub>2</sub> -to-CO Electrochemical Conversion. *J. Am. Chem. Soc.* **2016**, *138*, 16639–16644, DOI: 10.1021/jacs.6b07014.

- (7) Takeda, H.; Cometto, C.; Ishitani, O.; Robert, M. Electrons, Photons, Protons and Earth-Abundant Metal Complexes for Molecular Catalysis of CO<sub>2</sub> Reduction. *ACS Catal.* **2017**, *7*, 70– 88, DOI: 10.1021/acscatal.6b02181.
- (8) Rao, H.; Bonin, J.; Robert, M. Non-Sensitized Selective Photochemical Reduction of CO<sub>2</sub> to CO under Visible Light with an Iron Molecular Catalyst. *Chem. Commun.* **2017**, *53*, 2830– 2833, DOI: 10.1039/C6CC09967J.
- (9) Rao, H.; Bonin, J.; Robert, M. Visible-Light Homogeneous Photocatalytic Conversion of CO<sub>2</sub> into CO in Aqueous Solutions with an Iron Catalyst. *ChemSusChem* **2017**, *10*, 4447– 4450, DOI: 10.1002/cssc.201701467.
- (10) Ivanca, M. A.; Lappin, A. G.; Scheidt, W. R. Water-Soluble Ferric Porphyrinates: Solution and Solid-State Species. *Inorg. Chem.* **1991**, *30*, 711– 718, DOI: 10.1021/ic00004a022.
- (11) La, T.; Miskelly, G. M. Slow Interconversion of Aquo- and Hydroxo-Ligated Iron(III) Porphyrins. *J. Am. Chem. Soc.* **1995**, *117*, 3613– 3614, DOI: 10.1021/ja00117a031.
- (12) La, T.; Miskelly, G. M.; Bau, R. Solution NMR Studies and Crystal Structure of the Water-Soluble Iron(III) Porphyrin Iron 5,10,15,20-Tetrakis(2,3,5,6-Tetrafluoro-4- *N*, *N*, *N* -Trimethylaniliniumyl)Porphyrin ([FeTF<sub>4</sub>TMAP]<sup>5+</sup>). *Inorg. Chem.* **1997**, *36*, 5321– 5328, DOI: 10.1021/ic961486g.
- (13) La Mar, G. N.; Eaton, G. R.; Holm, R. H.; Walker, F. Ann. Proton Magnetic Resonance Investigation of Antiferromagnetic Oxo-Bridged Ferric Dimers and Related High-Spin Monomeric Ferric Complexes. *J. Am. Chem. Soc.* **1973**, *95*, 63– 75, DOI: 10.1021/ja00782a012.
- (14) Miskelly, G. M.; Webley, W. S.; Clark, C. R.; Buckingham, D. A. Acidity and Dimerization of Three Water-Soluble Iron(III) Porphyrin Cations: (*Meso-α*, *β*, *α*, *β*-Tetrakis(*o*-(*N*-Methylnicotinamido)Phenyl)Porphyrinato)Iron(III), (*Meso-α*, *α*, *α*, *α*-Tetrakis(*o*-(*N*-Methylnicotinamido)Phenyl)Porphyrinato)Iron(III), and (*Meso*-Tetrakis(1-Methylpyridinium-4-yl)Porphyrinato)Iron(III). *Inorg. Chem.* **1988**, *27*, 3773– 3781, DOI: 10.1021/ic00294a021.

- (15) Stong, J. D.; Hartzell, C. R. Heme Models I. Solution Behavior of a Water Soluble Iron Porphyrin. *Bioinorg. Chem.* **1976**, *5*, 219– 233, DOI: 10.1016/S0006-3061(00)82020-7.
- (16) Forshey, P. A.; Kuwana, T. Electrochemical and Spectral Speciation of Iron Tetrakis(N-Methyl-4-Pyridyl)Porphyrin in Aqueous Media. *Inorg. Chem.* **1981**, *20*, 693– 700, DOI: 10.1021/ic50217a011.
- (17) Torbensen, K.; Joulié, D.; Ren, S.; Wang, M.; Salvatore, D.; Berlinguette, C. P.; Robert, M. Molecular Catalysts Boost the Rate of Electrolytic CO<sub>2</sub> Reduction. *ACS Energy Lett.* **2020**, *5*, 1512– 1518, DOI: 10.1021/acsenerylett.0c00536.
- (18) Williams, L. J.; Dowgiallo, A.-M.; Knappenberger, K. L. Plasmonic Nanoparticle Networks Formed Using Iron Porphyrin Molecular Bridges. *Phys. Chem. Chem. Phys.* **2013**, *15*, 11840, DOI: 10.1039/c3cp51420j.
- (19) Gonçalves, P. J.; Sciuti, L. F.; Neto, N. M. B.; e Silva, R. C.; Silveira-Alves, E.; Mendonça, C. R.; Zílio, S. C.; Borissevitch, I. E.; de Boni, L. Effects of PH on the Ultrafast Transient Absorption of Iron (III) Meso-Tetrakis(4-N-Methyl-Pyridiniumyl) Porphyrin (Fe<sup>3+</sup>+TMPyP) Molecular Complexes. *J. Photochem. Photobiol., A* **2021**, *408*, 113082, DOI: 10.1016/j.jphotochem.2020.113082.
- (20) Fleischer, E. B.; Palmer, J. M.; Srivastava, T. S.; Chatterjee, A. Thermodynamic and Kinetic Properties of an Iron-Porphyrin System. *J. Am. Chem. Soc.* **1971**, *93*, 3162– 3167, DOI: 10.1021/ja00742a012.
- (21) Böhm, P.; Gröger, H. Iron(III)-Porphyrin Complex FeTSP: A Versatile Water-Soluble Catalyst for Oxidations in Organic Syntheses, Biorenewables Degradation and Environmental Applications. *ChemCatChem* **2015**, *7*, 22– 28, DOI: 10.1002/cctc.201402331.
- (22) Dolphin, D. *The Porphyrins. Volume 3, Part A*; Academic Press: New York, 1978.
- (23) Abdullin, D.; Fleck, N.; Klein, C.; Brehm, P.; Spicher, S.; Lützen, A.; Grimme, S.; Schiemann, O. Synthesis of  $\mu_2$ -Oxo-Bridged Iron(III) Tetraphenylporphyrin–Spacer–Nitroxide Dimers and Their Structural and Dynamics Characterization by Using EPR and MD Simulations. *Chem.—Eur. J.* **2019**, *25*, 2586– 2596, DOI: 10.1002/chem.201805016.

- (24) Kobayashi, H.; Higuchi, T.; Kaizu, Y.; Osada, H.; Aoki, M. Electronic Spectra of Tetrphenylporphinatoiron(III) Methoxide. *Bull. Chem. Soc. Jpn.* **1975**, *48*, 3137–3141, DOI: 10.1246/bcsj.48.3137.
- (25) Kobayashi, H. Magnetic Circular Dichroism of the Iron (III) Porphyrins. *Adv. Biophys.* **1976**, *8*, 191–222.
- (26) Kobayashi, N.; Koshiyama, M.; Osa, T.; Kuwana, T. Magnetic Circular Dichroism Studies on [5,10,15,20-Tetrakis(1-Methylpyridinium-4-yl)Porphinato]Iron and Some of Its Derivatives. *Inorg. Chem.* **1983**, *22*, 3608–3614, DOI: 10.1021/ic00166a024.
- (27) Kobayashi, N. [5,10,15,20-Tetrakis(1-Methylpyridinium-2-, -3-, and -4-yl)Porphinato]Iron Complexes as Seen by Electronic Absorption, Magnetic Circular Dichroism, and Electron Paramagnetic Resonance Spectroscopy. *Inorg. Chem.* **1985**, *24*, 3324–3330, DOI: 10.1021/ic00215a005.
- (28) Torbensen, K.; Han, C.; Boudy, B.; Wolff, N.; Bertail, C.; Braun, W.; Robert, M. Iron Porphyrin Allows Fast and Selective Electrocatalytic Conversion of CO<sub>2</sub> to CO in a Flow Cell. *Chem.—Eur. J.* **2020**, *26*, 3034–3038, DOI: 10.1002/chem.202000160.
- (29) Rao, H.; Lim, C.-H.; Bonin, J.; Miyake, G. M.; Robert, M. Visible-Light-Driven Conversion of CO<sub>2</sub> to CH<sub>4</sub> with an Organic Sensitizer and an Iron Porphyrin Catalyst. *J. Am. Chem. Soc.* **2018**, *140*, 17830–17834, DOI: 10.1021/jacs.8b09740.
- (30) Rury, A. S.; Sension, R. J. Broadband Ultrafast Transient Absorption of Iron (III) Tetrphenylporphyrin Chloride in the Condensed Phase. *Chem. Phys.* **2013**, *422*, 220–228, DOI: 10.1016/j.chemphys.2013.01.025.
- (31) Williams, L. J.; Knappenberger, K. L. Solvent-Dependent Absorption and Electronic Relaxation Dynamics of Iron (III) Tetra-4-N-Methylpyridylporphine. *Chem. Phys. Lett.* **2017**, *671*, 100–106, DOI: 10.1016/j.cplett.2017.01.011.
- (32) Hodgkiss, J. M.; Chang, C. J.; Pistorio, B. J.; Nocera, D. G. Transient Absorption Studies of the Pacman Effect in Spring-Loaded Diiron(III)  $\mu$ -Oxo Bisporphyrins. *Inorg. Chem.* **2003**, *42*, 8270–8277, DOI: 10.1021/ic034751o.
- (33) Guest, C. R.; Straub, K. D.; Hutchinson, J. A.; Rentzepis, P. M. Picosecond Absorption Studies on the Excited State of ( $\mu$ -Oxo)-

Bis[(Tetraphenylporphinato)Iron(III)]. *J. Am. Chem. Soc.* **1988**, *110*, 5276– 5280, DOI: 10.1021/ja00224a006.

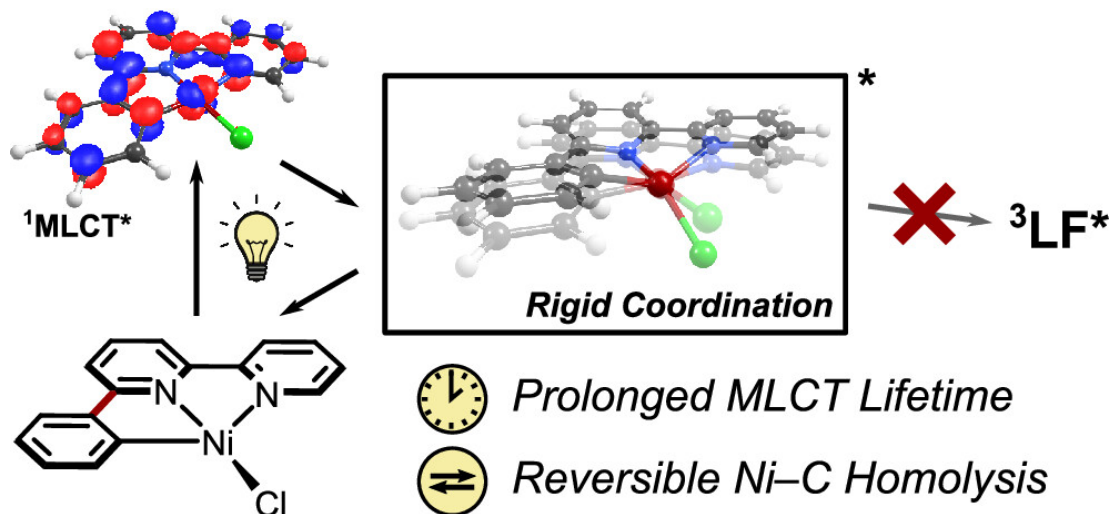
- (34) Rosenthal, J.; Lockett, T. D.; Hodgkiss, J. M.; Nocera, D. G. Photocatalytic Oxidation of Hydrocarbons by a Bis-Iron(III)- $\mu$ -Oxo Pacman Porphyrin Using O<sub>2</sub> and Visible Light. *J. Am. Chem. Soc.* **2006**, *128*, 6546– 6547, DOI: 10.1021/ja058731s.
- (35) Nappa, M.; Valentine, J. S. The Influence of Axial Ligands on Metalloporphyrin Visible Absorption Spectra. Complexes of Tetraphenylporphinatozinc. *J. Am. Chem. Soc.* **1978**, *100*, 5075– 5080, DOI: 10.1021/ja00484a027.
- (36) Rosenthal, J.; Pistorio, B. J.; Chng, L. L.; Nocera, D. G. Aerobic Catalytic Photooxidation of Olefins by an Electron-Deficient Pacman Bisiron(III)  $\mu$ -Oxo Porphyrin. *J. Org. Chem.* **2005**, *70*, 1885– 1888, DOI: 10.1021/jo048570v.

**CHAPTER 3: THE NON-INNOCENT ROLE OF AMINE ADDITIVES  
IN THE ELECTROCHEMICAL GENERATION OF HIGHLY REDUCED  
CO REDUCTION PRODUCTS IN A MOLECULAR IRON PORPHYRIN  
SYSTEM**

This chapter is temporarily embargoed.

CHAPTER 4: PHOTOPHYSICS OF A STRUCTURALLY  
CONSTRAINED Ni(II)-BIPYRIDINE ARYL HALIDE COMPLEX

**Constrained Ni(II)-bpy aryl halide complex**



Adapted with permission from:

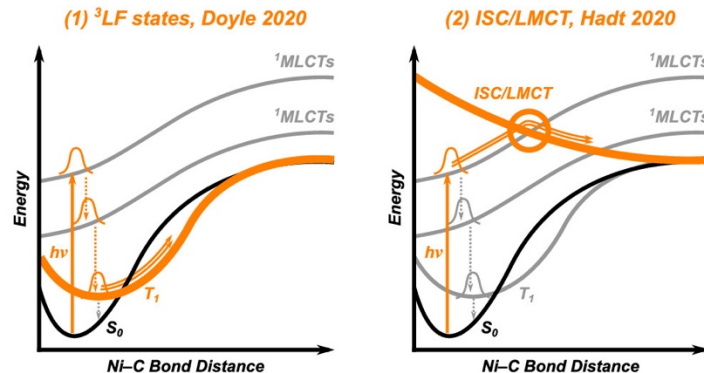
Bím, D.; Luedecke, K. M.; Cagan, D. A.; Hadt, R. G. "Light Activation and Photophysics of a Structurally Constrained Nickel(II)-Bipyridine Aryl Halide Complex." *Inorg. Chem.* **2024**, *63* (9), 4120. DOI: 10.1021/acs.inorgchem.3c03822.

Copyright 2024 American Chemical Society.

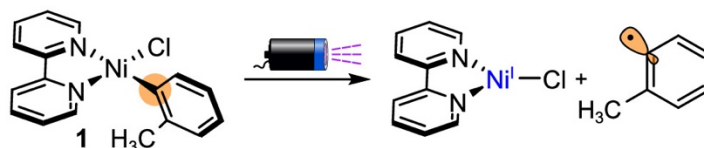
#### 4.1. Introduction

Photoredox catalysis has motivated modern synthetic organic chemistry through the development of selective bond transformations using light.<sup>1-8</sup> At its core, metallaphotoredox catalysis utilizes photoactive transition metal complexes to facilitate intramolecular charge transfer and/or outer-sphere electron transfer processes to generate catalytically reactive intermediates.<sup>9-16</sup> Nickel(II)–bipyridine (bpy) aryl halide complexes have emerged as a prominent class of light activated cross-coupling catalysts,<sup>7-22</sup> wherein direct photoexcitation leads to population of singlet metal-to-ligand charge transfer (<sup>1</sup>MLCT) excited-state potential energy surfaces and, ultimately, Ni(II)–C bond homolysis to yield reactive Ni(I) species.<sup>19</sup> Two bond homolysis mechanisms are outlined in **Figure 4.1a** and feature either (1) relaxation to a triplet Ni(II) ligand-field (<sup>3</sup>LF) state followed by thermal Ni(II)–C bond homolysis<sup>19</sup> or (2) intersystem crossing to repulsive ligand-to-metal charge transfer (LMCT) states (referred to herein as ISC/LMCT).<sup>21-23</sup> Assessing the interplay between these two (or other) possibilities remains challenging, however, as the quantum yields for Ni(II)–C bond homolysis are small, preventing direct observation using transient spectroscopies. Thus, ongoing efforts seek to understand the photophysical processes involved in photoredox catalysis and expand the catalytic repertoire and reactivity of nickel catalysts for specific applications.

a) Mechanisms of excited-state Ni–C bond homolysis



b) Conventional Ni–C bond homolysis



c) This work: Reversible Ni–C bond homolysis

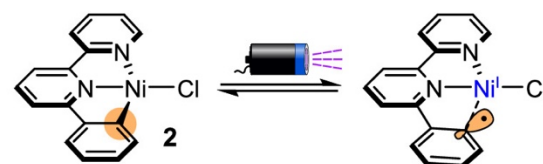


**Figure 4.1.** (a) Energy diagrams showing the proposed direct excitation mechanistic pathways for excited-state Ni(II)–C bond homolysis.<sup>19,23</sup> (b) Irradiation of untethered Ni(II)–bpy aryl halide yields the catalytically relevant Ni(I)–bpy halide intermediate and a free aryl radical. (c) Irradiation of a tethered Ni(II)–bpy aryl halide complex investigated in this work gives rise to a reversible Ni(II)–C bond homolysis equilibrium. The transient Ni(I)–bpy halide intermediate can be reacted with electrophiles in situ to promote the forward reaction.

Previous catalyst optimization efforts explored novel ligand architectures, bpy substitutions, and coordination environments to adjust the electronic properties of organonickel(II) complexes.<sup>19–21,24–29</sup> Ni(II)–C bond homolysis serves as a universal photoactive pathway and occurs even upon replacing the imine backbone with aliphatic amines or phosphines.<sup>20</sup> However, ligand modifications significantly influence the

kinetics of bond homolysis. Upon variation of the bpy and aryl substituents in Ni(II)–bpy aryl halide complexes, rate constants span  $\sim 2$  orders of magnitude, trend linearly with ligand Hammett parameters, and exhibit significant dependence on excitation energy.<sup>21,22</sup> These observations highlight the ability to tune key aspects of excited-state potential energy surfaces through structural modifications. Additionally, ligand substituents provide essential electronic contributions to the reactivity of photogenerated Ni(I) intermediates<sup>24,26,30</sup> and can be finely adjusted to suit different substrates in oxidative addition, to vary the overall solution-phase stability of Ni(I) species to improve selectivity, or to avoid off-cycle reactions.

The present study establishes the photochemical and photophysical properties of an underexplored, tethered Ni(II)–bpy aryl halide complex that has yet to be considered in the context of photoredox catalysis. Covalently tethering the aryl and bpy results in a fixed pseudosquare planar coordination geometry.<sup>31</sup> Such a structural constraint contrasts traditional untethered analogues and provides a platform to explore how limited ligand flexibility influences excited-state relaxation processes in photoredox catalysis, as we hypothesized that geometric restrictions may modify ground- and excited-state potential energy surfaces and thus the ability to produce reactive intermediates upon photoexcitation. Herein, we have examined the tethered Ni(II)–bpy aryl halide complex (**2**) using photochemical methods, ultrafast transient absorption (TA) spectroscopy, and quantum chemical calculations. Direct comparisons are made to those of the well-characterized, untethered complex (**1**).

Notably, **2** exhibits remarkable stability upon photoexcitation over a broad wavelength range. However, upon introduction of an electrophile during photoirradiation, **2** rapidly converts to a new species. Photochemical behavior studied herein supports the presence of a reversible  $\text{Ni(II)–C(aryl)} \rightleftharpoons [\text{Ni(I)} + \text{C(aryl)}^*]$  photochemical reaction and demonstrates that a photogenerated Ni(I) species can be productively captured by reaction with an electrophile. In addition to their distinct photochemical behavior, **1** and **2** exhibit distinct photophysics. While relaxation to a low-energy  $^3\text{LF}$  state has been established for **1**, structural constraints in **2** prohibit  $^3\text{LF}$  state formation and restrict excited-state relaxation, as probed by ultrafast TA spectroscopy, to MLCT potential energy surfaces.

The photoactivation of **2** in the presence of an electrophile, despite the lack of  $^3\text{LF}$  state formation, further suggests that an ISC/LMCT pathway (**Figure 4.1a**, right) may facilitate excited-state Ni(II)–C bond homolysis. In addition to inhibiting  $^3\text{LF}$  state formation, structural constraints in **2** prolong 1MLCT and relaxed- $^{1/3}\text{MLCT}$  lifetimes by factors of  $\sim 10$  and  $\sim 2$ , respectively. As such, this study holds promise for advancing our understanding of ligand electronic and steric effects in photoredox catalysis and guides approaches to unlocking new potential for the design of efficient and selective photoactive catalysts for organic synthesis.

## 4.2. Results and Analysis

### 4.2.1. Steady-State UV-vis Absorption Spectroscopy

Untethered (**1**) and covalently tethered (**2**) Ni(II)–bpy aryl halide complexes were synthesized and characterized following previous literature reports (Supporting Information section S1.2). UV–vis spectra of **1** and **2** in THF revealed two broad bands in the region of  $\sim 350$ – $600$  nm, which were previously assigned to low- (band *i*) and high-energy (band *ii*)  $^1\text{MLCT}$  transitions (**Figure 4.2**).<sup>18,21,31</sup> For **2**, band *i* is red-shifted by  $\sim 900$   $\text{cm}^{-1}$  ( $\lambda_{i,\text{max}} = 485$  and  $507$  nm for **1** and **2**, respectively) and exhibits a lower extinction coefficient ( $\epsilon = 4070$   $\text{M}^{-1} \text{cm}^{-1}$  and  $2800$   $\text{M}^{-1} \text{cm}^{-1}$  for **1** and **2**, respectively). For 11 corresponding untethered complexes, we have observed a loose trend between increasing  $\epsilon$  and longer  $\lambda_{i,\text{max}}$ , which is the opposite trend observed here for **1** and **2**.<sup>21</sup> Therefore, we attribute the lower  $\epsilon$  in **2** to the different aryl orientations, which influences the relative overlap between donor and acceptor molecular orbitals involved in the MLCT transitions. Furthermore, peak maxima red-shift and decrease in intensity in toluene relative to THF (**Figure S2**), corroborating the assignment of bands *i* and *ii* as mainly  $^1\text{MLCT}$  electronic transitions with Ni(II)-to-Phbpy  $\pi^*$  character.

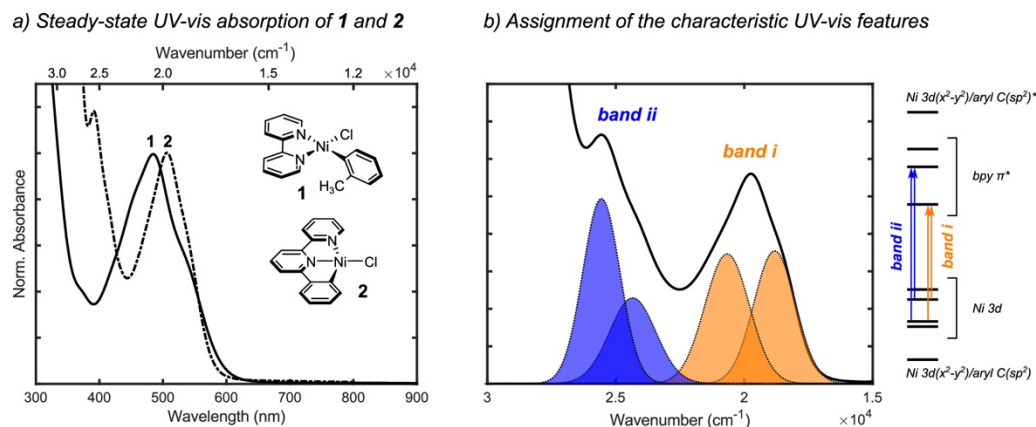


**Figure 4.2.** (a) UV–vis absorption spectra of **1** and **2** in THF. Spectra recorded in toluene are provided in **Figures S2** and **S7**. (b) Schematic representation of electronic transitions comprising bands *i* and *ii*

CASSCF/QD-NEVPT2 calculations predict multiconfigurational ground states for **1** and **2**, with closed-shell singlet weights in the CAS configuration interaction vector of only ~56–57%. Remaining configurations consist of <sup>1</sup>MLCT states (~20% and ~22% for **1** and **2**, respectively) and <sup>1</sup>LF states (~17% and ~16% for **1** and **2**, respectively; **Tables S4** and **S5**). The lowest vertical excited triplet states of mainly <sup>3</sup>LF character are at ~9300 cm<sup>-1</sup> (~26.6 kcal mol<sup>-1</sup>) and ~10 800 cm<sup>-1</sup> (~30.9 kcal mol<sup>-1</sup>) for **1** and **2**, respectively (**Figure S28**). However, free energy differences between the optimized (adiabatic) triplet and ground states are significantly different, with  $\Delta G = \sim 8$  kcal mol<sup>-1</sup> (for **1**) and  $\Delta G = \sim 27$  kcal mol<sup>-1</sup> (for **2**). This difference demonstrates a significant stabilization of the lowest energy <sup>3</sup>LF state in **1** due to sterically unencumbered geometric rearrangement, which allows for the formation of a relaxed, pseudo-*T<sub>d</sub>* coordination. The same structure is inaccessible in **2** due to steric constraints provided by the covalently tethered aryl group (**Figure S32**).

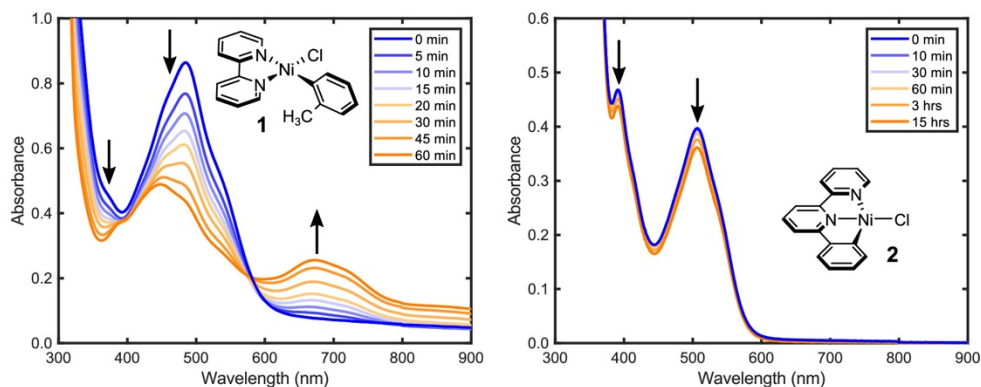
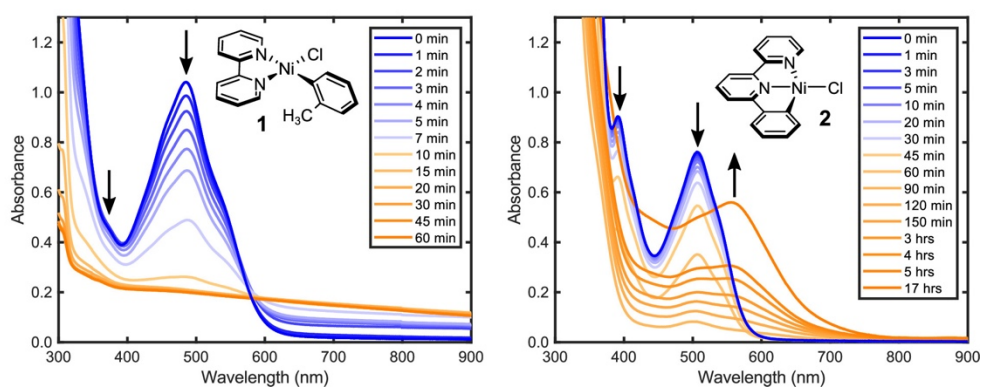
For **1**, calculations predict that bands *i* and *ii* in **Figure 4.2b** are mainly <sup>1</sup>MLCT in nature, consisting of excitations between specific Ni 3d donor orbitals and bpy  $\pi^*$  acceptor orbitals.<sup>19,21,32</sup> The most intense excitations are found for Ni 3d(*xz*)/3d(*yz*) donor orbitals, consistent with a previous report.<sup>21</sup> However, tethering the aryl group in **2** changes the composition of the electronic excitations. While excited states with the largest oscillator

strengths in **1** are  $^1\text{MLCT}$  states, the  $^1\text{LF}$  states in **2** have intensities comparable to those of the most intense low-energy  $^1\text{MLCT}$  band (**Figures S29** and **S30**). We attribute this behavior to a better electronic conjugation and overlap between the tethered aryl and bpy ligand, which increases the bpy character (thus mixing some allowed MLCT intensity) in the unoccupied Ni  $3d(x^2-y^2)/C(sp^2)^*$  acceptor orbital (**Figure S27**). The calculated intensity of the low-energy band in **2** also decreases by  $\sim 2.5$  times relative to **1** (**Tables S6** and **S7**), in agreement with the smaller experimental extinction coefficient.

In summary, covalently tethering the aryl and bpy groups modulates the electronic properties of **2** relative to **1**, as manifested in the experimental and computational changes in the excited-state compositions and intensities of bands *i* and *ii*, with band *ii* being responsible for light-activation in direct excitation nickel photoredox catalysis. In terms of other well-studied Ni(II)–bpy aryl halide complexes, tethered complex **2** provides an important reference for a comprehensive investigation of the influences of electronic and steric perturbations on its photophysical and photochemical characteristics.

#### 4.2.2. Photochemical Activity

Irradiating **2** in THF using a 390 nm LED (exciting high-energy  $^1\text{MLCT}$  band *ii*) resulted in no significant photochemical activity after 15 h (**Figure 4.3a**, right). Slow decay of characteristic absorption features occurs after prolonged irradiation, likely due to unproductive photodegradation. **2** is also photoinactive over a broad range of excitation wavelengths (370, 427, 456, 525 nm; **Figure S6**) and in toluene (**Figure S7**). This behavior is in stark contrast to **1**, which affords almost full conversion to a previously characterized Ni(I)–bpy chloride species after 1 h of photoirradiation (**Figure 4.3a**, left) using a 390 nm LED with the same power ( $k_{\text{obs}} = 3.8 \times 10^{-2} \text{ min}^{-1}$  and  $\Phi = 0.5 \times 10^{-3}$ ; LED power of  $170 \text{ mW cm}^{-2}$ ).

a) Photoirradiation of **1** and **2** using 390 nm LEDb) Photoirradiation of **1** and **2** using 390 nm LED with addition of 1000 eq. mesityl bromide

**Figure 4.3.** Photoirradiation of **1** and **2** in THF using a 390 nm LED. (a) Time-dependent photolysis profiles of **1** and **2**. (b) Time-dependent photolysis profiles of **1** and **2** in the presence of 1000 equiv of mesityl bromide

The distinct photochemical behavior of **1** and **2** (**Figure 4.3a**) indicates that **2** either (a) does not follow the same photoexcitation/relaxation pathways as **1** or (b) excited-state Ni(II)–C bond homolysis, although potentially viable, is reversible due to the covalent tethering of the bpy and aryl groups. We note that the absence of any photoproduct formation following the irradiation of **2** excludes alternate pathways for its irreversible decomposition, such as through Ni(II)–Cl bond homolysis. To distinguish between the two cases above, we have repeated photochemical experiments in the presence of a large excess (1000 equiv) of mesityl bromide, which should react if a Ni(I) intermediate is formed *in situ*. The steady-state UV–vis spectra do not change appreciably upon the addition of mesityl bromide (**Figure S3**); no reactivity is observed between Ni(II) and

mesityl bromide without irradiation. However, bands *i* and *ii* of parent Ni(II) complexes **1** and **2** decay more rapidly upon 390 nm LED irradiation in the presence of mesityl bromide (**Figure 4.3b**).

Compounds **1** and **2** exhibit distinct photochemical differences when irradiated in the presence of a large excess of mesityl bromide. Untethered **1** exhibits precedented reactivity; the accumulation of the Ni(I)–bpy chloride intermediate complex is fully suppressed by mesityl bromide (**Figure 4.3b**, left). The proposed pathway for this reactivity consists of oxidative addition of mesityl bromide to Ni(I) to yield a high-energy Ni(III) intermediate,<sup>30,33–35</sup> which can then undergo comproportionation with another Ni(I) in each reaction cycle to produce a new photoactive Ni(II)–bpy aryl halide and a photoinactive Ni(II)–bpy dihalide in a 1:1 ratio.<sup>16,33</sup> With extended irradiation, all of the starting Ni(II)–bpy aryl halide complexes are expected to ultimately convert to a triplet d<sup>8</sup> Ni(II)–bpy dihalide (**Scheme S8**), which does not possess distinctive UV–vis absorption features in the visible region (**Figure S4**). Note that the sloping UV–vis spectra in **Figure 4.3b** (left) is indicative of either the precipitation of Ni(II)–bpy dihalide or formation of an off-pathway [Ni(I)–bpy halide]<sub>2</sub> binuclear species from two Ni(I)–bpy halide units.<sup>30</sup>

Conversely, irradiation of **2** with 1000 equiv of mesityl bromide produces a new, stable species with a red-shifted absorption band at 555 nm (**Figure 4.3b**, right). Interestingly, a species with a similar absorption profile (absorption bands centered at 547, 399, and 352 nm; see **Figure S11** for comparison) has been observed by Klein and co-workers via one-electron reductive dissociation of the bromide anion from a related tethered Ni(II)–bpy phenyl bromide complex.<sup>36</sup> Based on spectroelectrochemistry, that species was assigned as the tethered, tridentate Ni(I)–bpy phenyl complex. Similar to our photochemical process, no isosbestic points were detected in the spectroelectrochemical conversion of the parent species to the proposed Ni(I)–bpy phenyl intermediate, suggesting more complex multistep reactivity.

Our attempts to isolate and characterize this soluble photogenerated species have been unsuccessful due to complications associated with irradiation of larger quantities of starting material (e.g., low solubility and low light penetration) and the presence of a large excess of mesityl bromide, Ni(II)–bpy dihalide (*vide infra*), and unreacted Ni(II)–bpy aryl

halide in the reaction mixture after irradiation. However, according to UV-vis and paramagnetic  $^1\text{H}$  NMR spectroscopic characterization of the crude reaction mixture, we note that the photogenerated species is paramagnetic ( $^1\text{H}$  NMR peaks at  $\sim 18$ ,  $\sim 23$ , and  $\sim 69$ – $76$  ppm) and stable under high temperature and concentration conditions and reacts rapidly with air (see section S1.4 of the Supporting Information). These findings corroborate the results of Klein and co-workers associating the UV-vis features to a tridentate Ni(I)-bpy phenyl species.<sup>36</sup> We also note that calculated (CASSCF/QD-NEVPT2) absorption spectra are consistent with this assignment with the tethered, tridentate Ni(I)-bpy phenyl species exhibiting a slight red shift of the main absorption feature from the parent Ni(II) complex (**Figure S31**). The calculated oscillator strengths further suggest that  $\sim 50\%$  of the parent Ni(II) species is converted to this Ni(I)-bpy phenyl species.

Additionally, from the same reaction mixture, we were able to isolate an appreciable amount of sparingly soluble Ni(II)-bpy dihalide; its spectroscopic features resemble an independently synthesized Ni(II)-<sup>Ph</sup>bpy dichloride (**Figure 4.4** and section S1.4 of the Supporting Information). We note that the possible presence of mixed chloride and bromide species cannot be ruled out, since the peaks in the paramagnetic region in **Figure 4.4** are fairly broad. Moreover, the  $^1\text{H}$  NMR spectrum of the sample was collected from the crude reaction mixture as a precipitate, washed with THF, and redissolved in  $\text{D}_2\text{O}$  for NMR analysis. Therefore, different solubilities of the chloride/bromide complex might result in altered speciation. Nonetheless, this comparison supports photodissociation of the tethered aryl ligand being indeed feasible in **2** as in **1**, as irradiation of **2** also yields an intermediate that is captured by mesityl bromide and ultimately results in the formation of a Ni(II)-bpy dihalide complex.

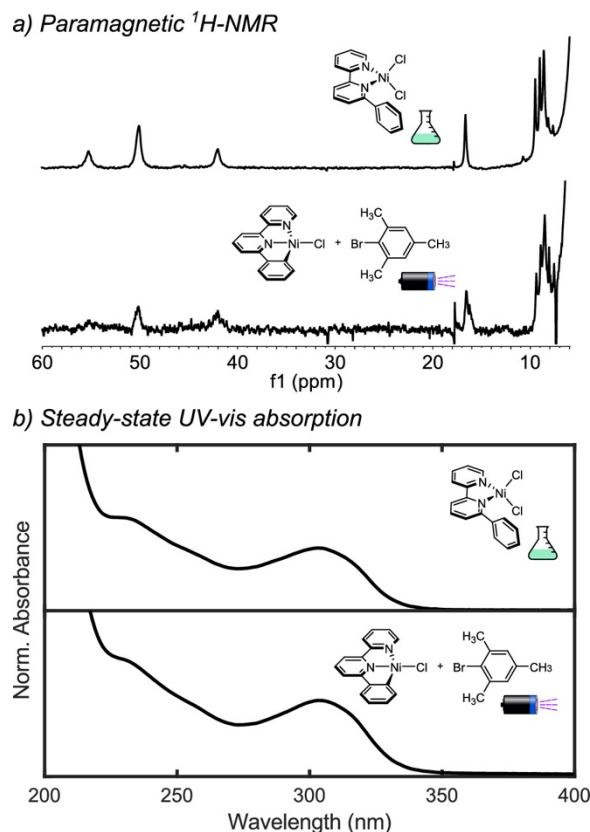


**Figure 4.4.** Spectroscopic characterization and comparison between the independently synthesized Ni(II)–Phbpy dichloride (top) and the isolated product of irradiation of **2** with mesityl bromide (bottom). (a) Paramagnetic  $^1\text{H}$  NMR spectra measured in  $\text{D}_2\text{O}$ . (b) Steady-state UV–vis absorption in  $\text{H}_2\text{O}$

Photochemical reactions of **1** and **2** exhibit distinct dependence on mesityl bromide concentrations, with increasing rates observed with increasing mesityl bromide concentrations (**Figure S19**). In both **1** and **2**, the decay of Ni(II) is assisted by the presence of mesityl bromide in solution. As discussed above, this observation is attributed to a reversible equilibrium for Ni(II)–C bond homolysis in **2**. For **1**, this behavior can likely be attributed to a solvent-caging effect, which prevents aryl radical diffusion from Ni(I), allowing sufficient time for reformation of the Ni(II)–C bond.<sup>37</sup> This effect is less pronounced when mesityl bromide is present in sufficiently high concentrations (**Figure S19**), likely due to limited formation of caged radicals due to a more rapid Ni(I) reaction with the electrophile in solution. Although complex kinetics (especially at higher mesityl

bromide concentrations) preclude obtaining well-defined rate constants for the Ni(II)–C bond homolysis step (see further discussion in Supporting Information section S1.5), we note that the irradiations of **1** with and without the addition of quantitative excess mesityl bromide reveal a nearly 2–3-fold increase in Ni(II) conversion. Such estimation offers valuable insights into the quantum yields of Ni(II)–C photochemical bond homolysis and aids in deconvolution between “productive” ligand dissociation and “unproductive” recombination kinetics. It is worth noting that the addition of mesityl bromide does not influence the ultrafast photophysical relaxation pathways as discussed below in section 2.3 and instead facilitates the dissociation of aryl radicals from the [Ni(I)···C(aryl)\*] cage. Ongoing work involves detailed quantum chemical molecular dynamics simulations being performed to better understand the behaviors of **1** and **2** after photoexcitation and the impact of mesityl bromide addition on photolysis rate constants.

To better understand the nature of the photoinitiated reactivity of **2** with mesityl bromide, we performed irradiations of **2** with a variety of substituted aryl bromides (**Figures S14–S18**). We find that the soluble products seen after prolonged irradiations exhibit comparable absorption features, consistent with the same tethered Ni(I)–bpy phenyl product seen upon the irradiation of **2** with mesityl bromide. Interestingly, we have observed an electronic influence on the apparent rate of conversion of **2**; electron-donating substituents on the aryl bromide contribute to an enhancement of this rate. Steric effects appear to play a lesser role but with a poorly discernible trend. These preliminary results suggest that a concerted oxidative addition mechanism for the activation of aryl bromides via conversion of **2** may not be operative, as it would predict enhanced reactivity with aryl bromides with electron withdrawing substituents and reduced sterics.<sup>26,33</sup> Current efforts are underway to thoroughly detail the precise mechanism of the reactivity of aryl halides with light-activated **2**.

#### 4.2.3. *Transient Absorption Spectroscopy*

To further understand the photochemical differences between **1** and **2**, we examined their excited-state relaxation pathways by using ultrafast TA spectroscopy. The photophysics of **1** and other untethered Ni(II)–bpy aryl halide complexes have been described;<sup>18,19</sup> in this study, we include **1** for direct comparison with **2**. A consistent relaxation pathway for

Ni(II)–bpy aryl halides has been outlined, regardless of whether low-energy  $^1\text{MLCT}$  ( $\lambda_{\text{exc.}} = \sim 530 \text{ nm}$ ) or high-energy  $^1\text{MLCT}$  states ( $\lambda_{\text{exc.}} = \sim 400 \text{ nm}$ ) are accessed (bands *i* and *ii* in **Figure 4.2b**).<sup>18,19</sup> However, only the high-energy  $^1\text{MLCT}$  band *ii* was proposed to be relevant for catalysis, demonstrating excited-state Ni(II)–C bond homolysis and formation of a reactive Ni(I) intermediate.<sup>21,22</sup> This assignment is exemplified by the photochemical activity of **1**, which is considerably wavelength-dependent and requires a minimum energy threshold ( $\lambda_{\text{exc.}} < 525 \text{ nm}$ ) for photolysis (**Figure S5**).

The steady-state absorption profile of **2** is red-shifted relative to that of **1** (**Figure 4.2a**). This ultimately allows enhanced accessibility of the higher-energy  $^1\text{MLCT}$  states in **2** (band *ii*) with lower-energy light. Still, both species have a notable absorption intensity associated with a high-energy  $^1\text{MLCT}$  state near 400 nm. Therefore, 400 nm excitation has been utilized for TA to probe relaxation pathways from the  $^1\text{MLCT}$  excited states of **1** and **2**, thereby addressing key excited states relevant for catalysis.

Direct photoexcitation of **1** with pulsed 400 nm light in THF results in an excited-state lifetime on the nanosecond time scale (**Figure S21**). Global analysis revealed a three-component sequential decay model composed of a fast time component ( $\tau_1 = \sim 400 \text{ fs}$ ), an intermediate component ( $\tau_2 = \sim 9 \text{ ps}$ ), and a longer-lived state ( $\tau_3 = \sim 3.5 \text{ ns}$ ). This relaxation pathway agrees well with and is analogous to that characterized by Doyle and co-workers for **1** with  $\lambda_{\text{exc.}} = 530 \text{ nm}$  (**Table S3**).<sup>19</sup> As illustrated in **Figure 4.5**, the  $^1\text{MLCT}$  excited state is first accessed upon photoexcitation. This state decays either into a relaxed  $^1\text{MLCT}$  state through vibrational cooling or to a  $^3\text{MLCT}$  state via intersystem crossing. This process is observable through the blue-shifting of the excited-state absorption (ESA) in the red region of the spectrum (**Figure S21B**), which occurs on the picosecond time scale. The  $^1\text{MLCT}$  state then relaxes into an excited  $^3\text{LF}$  state observed through the decay of the ESA feature between a  $\sim 5\text{--}20 \text{ ps}$  time delay (**Figure S21C**). Finally, this  $^3\text{LF}$  excited state undergoes a longer, spin-forbidden relaxation back to the singlet ground state in several nanoseconds (**Figure S21D**), which is reflected by the recovery of the ground-state bleach (GSB).

### Excited-state dynamics of **1** and **2**

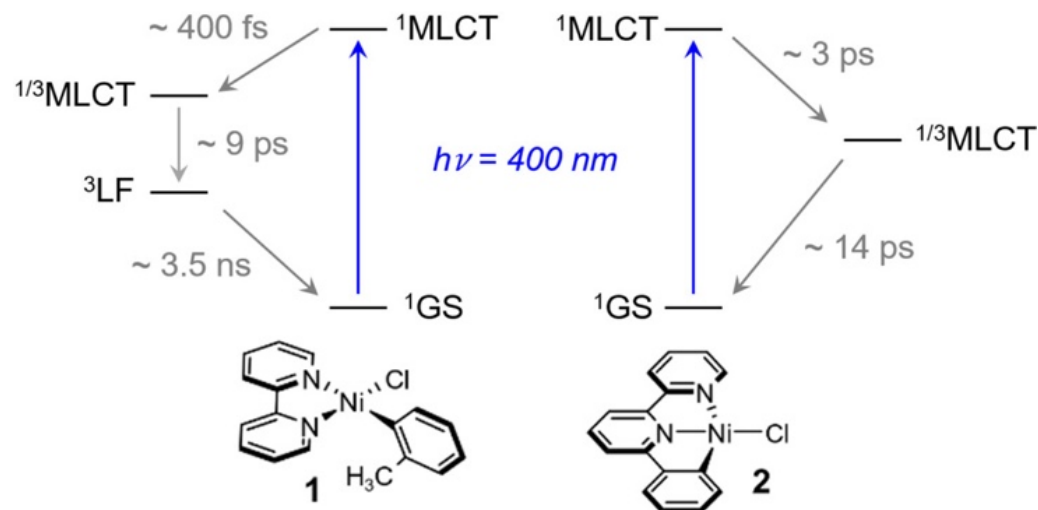


**Figure 4.5.** Proposed mechanisms of relaxation for **1** and **2** after photoexcitation into their excited  $^1\text{MLCT}$  states with 400 nm pulsed light

Photoexcitation of **2** into the high-energy  $^1\text{MLCT}$  state resulted in distinct excited-state dynamics relative to **1**. While the nonzero TA signal for **1** persists into the nanosecond regime, the entire excited-state manifold of **2** relaxes on the tens of picoseconds time scale, a significant shortening of excited-state lifetime by 2–3 orders of magnitude (**Figure 4.6**). Global analysis of the excited-state dynamics of **2** revealed a two-component sequential model consisting of a shorter ( $\tau_1 = \sim 3\text{ ps}$ ) and longer time component ( $\tau_2 = \sim 14\text{ ps}$ ). Analogous to **1**, the first  $\sim 10\text{ ps}$  of the TA difference spectra for **2** are dominated by a blue-shifting ESA alongside recovery of the GSB (**Figure 4.6c**). However, the longer time dynamics differ between the complexes, with the ESA decaying monoexponentially and with the same time constant associated with the recovery of the GSB (**Figure 4.6b** and **d**). This isosbestic behavior can be interpreted as recovery of the ground state directly from the relaxed- $^1\text{MLCT}$  or  $^3\text{MLCT}$  excited state. In all, the photophysical behavior of **2** does not support the formation of  $^3\text{LF}$  excited states with an appreciable quantum yield.

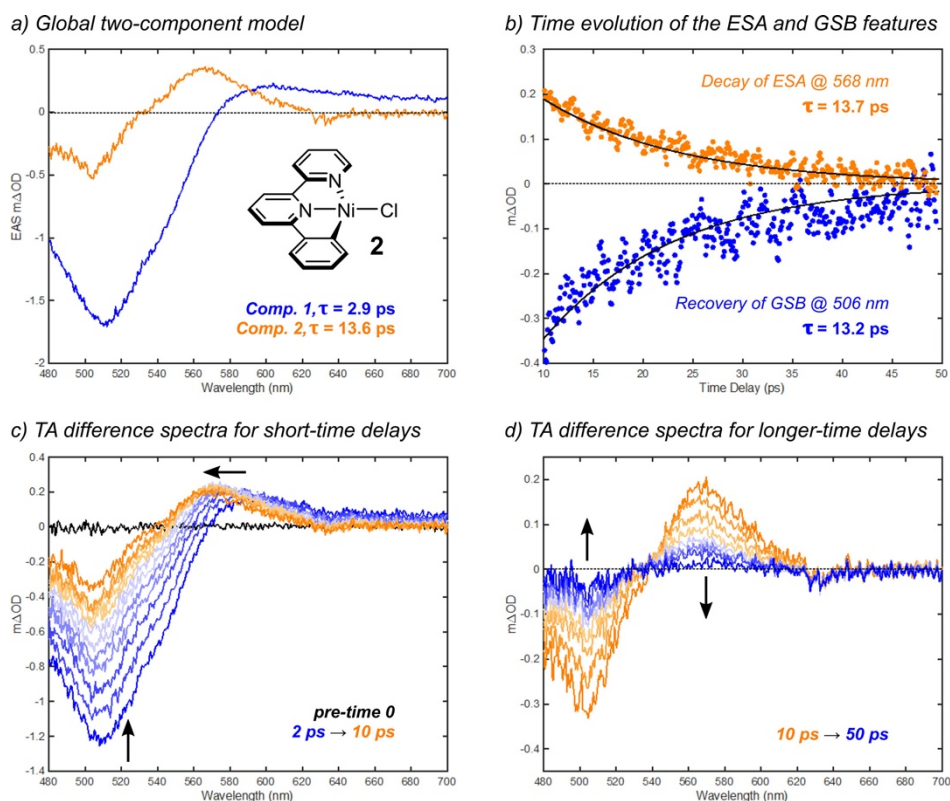


**Figure 4.6.** Ultrafast TA spectra of **2** in deoxygenated THF upon 400 nm excitation. (a) Evolution-associated spectra obtained from a two-component, sequential global model of the data. (b) Decay of the ESA feature at 568 nm ( $13.7 \pm 1.8$  ps, orange) and recovery of the GSB feature at 506 nm ( $13.2$  ps  $\pm 1.8$  ps, blue), with their fits to monoexponential functions in black. (c) TA difference spectra for short time delays between the pump and probe. (d) TA difference spectra for longer time delays between pump and probe

We also considered the influence of 100 equiv of mesityl bromide on the excited-state dynamics of **1** and **2**. Although UV–vis monitoring provides evidence of reactivity for **1** and **2** with 100 equiv of mesityl bromide during 390 nm LED photoirradiation (Figures S9 and S10), the relaxation pathways of **1** and **2** probed by TA spectroscopy remain largely unaffected by the addition of an electrophile, as relaxation time constants and spectral profiles are consistent between samples with and without mesityl bromide (see section S1.6 in the Supporting Information). These observations indicate that the TA of **1**

and **2** probe the dominant background relaxation processes and are insensitive to the low quantum yield processes related to light-activated reactivity with electrophiles (*vide infra*).

### 4.3. Discussion

Significant efforts have been dedicated to investigating the influence of steric and electronic factors on the photoredox reactivity of organonickel(II) complexes. These studies have unveiled structure–function relationships that elucidate how the ligand scaffold or electron-donating or -accepting substituents impact the formation of reactive Ni intermediates in cross-coupling catalysis. However, to the best of our knowledge, no data have been reported regarding organonickel(II) complexes with light-induced activation and dissociation of a coordinated aryl group tethered to the backbone ligand. While a number of previously synthesized tethered Ni(II)–bpy aryl halide complexes have been examined for electrochemical/reductive catalysis, including detailed spectroelectrochemical investigations, an explicit pathway for productive, direct light activation has not been outlined.<sup>31,36,38</sup> This study adopted a previously described tethered Ni(II)–bpy aryl chloride complex **2** and explored its photochemical and photophysical properties, particularly through a comparison to untethered Ni(II)–bpy aryl halide photocatalyst **1**.

In contrast to untethered analogues, **2** exhibits superior stability upon photoirradiation across a broad range of excitation wavelengths spanning ~370–525 nm. Despite this prolonged stability, the covalently tethered Ni(II) complex can still be light-activated for reactivity in the presence of electrophile. This reactivity can be attributed to a shift in reversible  $\text{Ni(II)–C(aryl)} \rightleftharpoons [\text{Ni(I)}\cdots\text{C(aryl)}^*]$  photochemical equilibrium, in which the resulting Ni(I) reacts with an electrophile in solution. Such improved stability could potentially be leveraged in photoredox catalysis. For instance, it was previously observed that the presence of electron-withdrawing substituents like methyl or ethyl esters at the bpy 4,4' positions significantly enhances the photochemical reactivity of **1**, while simultaneously shifting the steady-state absorption features to lower energies by ~2000  $\text{cm}^{-1}$  ( $\lambda_{i,\text{max}} = 532 \text{ nm}$ ).<sup>21</sup> A similar effect may be expected for **2**, which would result in even more markedly red-shifted MLCTs, making them accessible not only with lower-energy

light but also with the tethered ligand providing stability to the otherwise highly photochemically reactive Ni(II).

Although we have studied **2** in terms of its competency for photoredox catalysis, such photochemical robustness also offers the potential for regulating reactivity that is specific to experimental conditions. For example, by tuning the concentrations of other reactive species in solution, the unique photochemistry of **2** could be harnessed for a tailored release of Ni(I), thereby potentially advancing the reaction selectivity (**Figure 4.7**). This possibility could unveil intriguing and unexplored applications leveraging specific roles of Ni catalysts based on experimental conditions. A similar approach was employed to enhance yields and selectivity in cross-electrophile coupling reactions.<sup>39,40</sup> In ref. 39, adjusting the reduction potentials of homogeneous organic reductants allowed for the precise time-release of alkyl radicals from Katritzky salt precursors and, thus, synchronized their production rates with those of the Ni(II)–aryl intermediates proposed for their capture. This strategy minimized the probability of undesired side reactions and Ni catalyst decomposition. Similarly, Reisman and co-workers modulated formation rates of benzyl radicals, which yielded an analogous effect for the cross-coupling of alkenyl and benzyl electrophiles.<sup>40</sup> Analogously, the released benzyl radical is intercepted by a Ni(II)–alkenyl resting state, establishing a direct connection between radical generation rate and the selectivity of homo- vs cross-coupling reactivity. Modulation of the rate of Ni(I) formation based on the concentration of the electrophile, as demonstrated in this work, presents an alternative route to a similar strategy.

## Synchronizing Ni(II) activation and radical generation for improved selectivity in cross-coupling catalysis

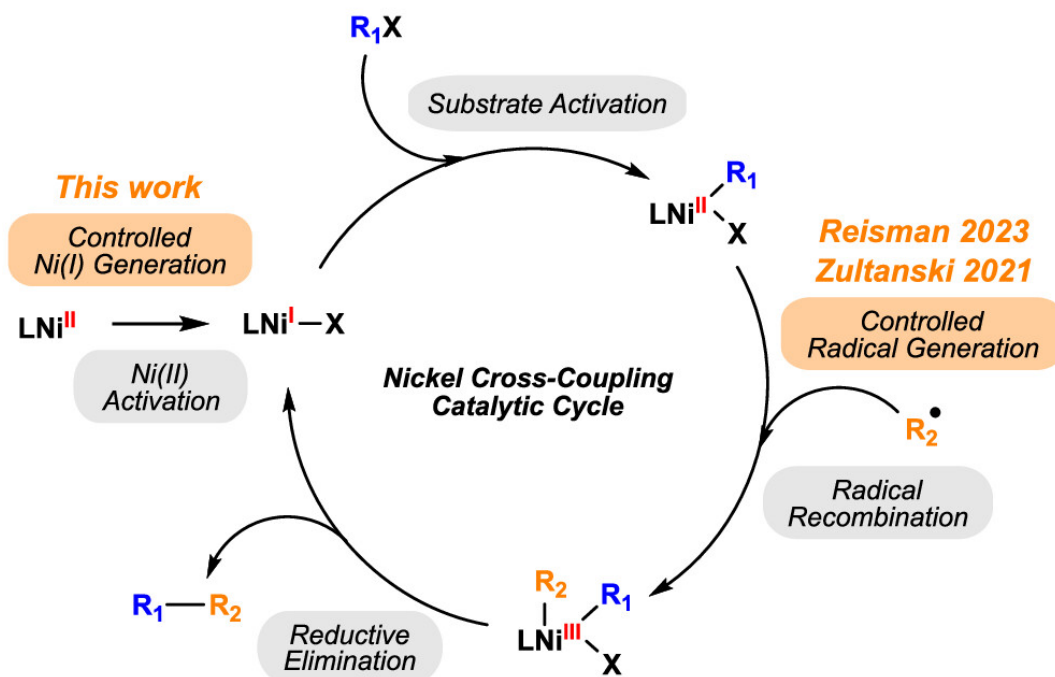


**Figure 4.7.** Cross-coupling selectivity in the Ni ground- and excited-state catalysis can be improved by synchronizing the generation of alkyl or aryl radicals ( $\text{R}_2^\bullet$ ) with the rate of formation of the  $\text{LNi}(\text{II})\text{R}_1\text{X}$  intermediate.<sup>39,40</sup> In this work, we propose an alternative strategy of controlling the generation of the  $\text{LNi}(\text{I})\text{X}$  complex from the parent Ni(II) precursor instead, offering an independent handle for the rate of nickel cross-coupling catalysis.

Further, regarding the reaction selectivity, **1** and **2** revealed different product formation upon photoirradiation in the presence of mesityl bromide. Prolonged irradiation of **1** culminated in the formation of Ni(II)–bpy dihalide, as monitored by the disappearance of the Ni(II)–bpy aryl halide UV–vis absorption features, which is consistent with the previously proposed oxidative addition and comproportionation reaction mechanism.<sup>16,30,33</sup> Contrastingly, **2** yielded a new Ni species with a unique UV–vis spectrum (**Figure 4.3b**, right) in addition to a Ni(II)–Phbpy dihalide. A species with a similar UV–vis spectrum was accessed via spectroelectrochemical one-electron reduction of the bromine analogue

of **2** and was attributed to the tethered, tridentate Ni(I)–bpy phenyl complex.<sup>36</sup> Here, we propose a photochemical pathway to the formation of this reaction intermediate. The formation of Ni(II)–Phbpy dihalide in the reaction mixture also supports the activation of mesityl bromide (**Figure 4.4**). However, this species is not the dominant product, as the higher stability of the tethered Ni(I)–bpy phenyl species and its lack of reactivity with mesityl bromide terminate the catalytic cycle at this stage. The low reactivity of the Ni(I)–bpy phenyl is likely due to the steric hindrance of the tridentate ligand coordinating and protecting the Ni(I) center. Under catalytic conditions, this stable Ni(I) intermediate could potentially be reactivated via reactivity with radicals,<sup>41,42</sup> sterically accessible alkyl bromides,<sup>43</sup> or through outer-sphere single-electron transfer processes.<sup>44</sup>

An examination of mesityl bromide concentration-dependent photochemistry highlighted controllable Ni(II) species decomposition rates (**Figure S19**), further supporting the notion of reversibility in excited-state bond homolysis. Intriguingly, a similar observation was made for both **2** and **1**, wherein reversibility in the Ni(II)–C(aryl)  $\rightleftharpoons$  [Ni(I)···C(aryl)\*] excited-state bond homolysis in the latter was not previously considered. While the concept of solvent caging and retaining the aryl radical in the proximity of Ni(II) has been posited for an oxidative addition of aryl halides reacting through a halogen-atom abstraction mechanism,<sup>33</sup> the impact of this reversibility on photochemical reactivity remains unexplored. Through a comparative assessment of the rate constants of photochemical decay of **1** with varying mesityl bromide concentrations, we observed a 5-fold increase in the rate constant. While the experimental data reported here were obtained solely in THF, a thorough investigation of the solvent dependence of this rate enhancement would provide valuable insights for understanding the effect of caged radical recombination in photoredox catalysis.<sup>45</sup> Unfortunately, the inherently low quantum yields of Ni(II)–C bond homolysis and very short MLCT excited state lifetimes hinder a direct, comprehensive experimental survey of the excited-state bond homolysis. Traditional computational methods—often static and only probing vertical energies and vertical excited states—are also insufficient.<sup>21,23,46,47</sup> Given the complexities of the excited-state dynamics and bond homolysis behavior, which may also require a multireference

treatment, insights derived from the experimental data in this study could provide an important reference for benchmarking more advanced molecular dynamics simulations.

When considering the reversibility of C(aryl) $\cdot$  formation, it is noteworthy to emphasize the research by Park and co-workers who observed a similar phenomenon with Ni(II) metallacycle compounds (**Figure 4.8**).<sup>20</sup> Regardless of the specific backbone ligand, metallacycles featuring cycloneophyl ( $-\text{C}_6\text{H}_4\text{-}o\text{-C}(\text{CH}_3)_2\text{CH}_2-$ ) and its oxa- ( $-\text{OC}_6\text{H}_4\text{-}o\text{-C}(\text{CH}_3)_2\text{CH}_2-$ ) and thia- ( $-\text{SC}_6\text{H}_4\text{-}o\text{-C}(\text{CH}_3)_2\text{CH}_2-$ ) derivatives have been proposed to undergo light-induced carbon radical generation through Ni(II)–C(sp<sup>3</sup>) bond homolysis. In the case of thia-metallacycles, radical formation can be followed by C–S bond formation through reductive elimination. In cycloneophyl and its oxa derivative, however, radical formation is followed by recombination to reform the reactant state (**Figure 4.8**). While the covalent Ni–X linkage in the metallacycles and their overall chemical behavior resemble that of **2**, the proposed observation of reversibility in **1** and the photophysics presented in this work suggest that reversible radical recombination to Ni might represent a more general paradigm to consider in Ni photoredox and single-electron chemistry.

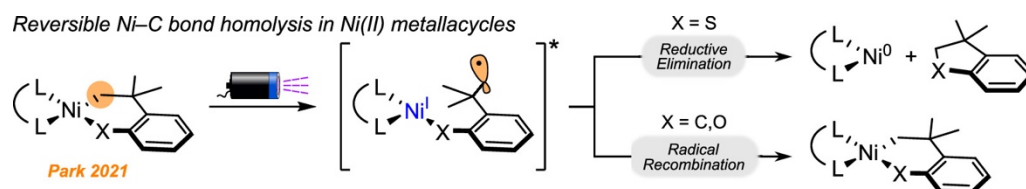


**Figure 4.8.** Irradiation of Ni(II) metallacycle compounds results in the formation of transient bound-C(sp<sup>3</sup>) radicals that can either facilitate reductive elimination or recombine to recover the Ni(II) ground state.

Using transient spectroscopies, Doyle and co-workers have provided significant insights into the excited-state dynamics of untethered Ni(II)–bpy aryl halide complexes related to **1**.<sup>18,19</sup> They observed comparable excited-state dynamics using either 400 or 530 nm excitation and further provided valuable insights into the lifetimes of key MLCT and LF excited states. Their findings established that <sup>1</sup>/<sub>3</sub>MLCT lifetimes are short (<~15 ps in a series of eight Ni(II)–bpy aryl halide complexes), while <sup>3</sup>LF states are significantly

longer-lived ( $\sim 2\text{--}8$  ns). From this analysis, in conjunction with corroborating  $^1\text{H}$  NMR 2D Exchange Spectroscopy (EXSY) and DFT-calculated bond strengths, it was inferred that the excited state responsible for Ni(II)–C(aryl) bond homolysis is the  $^3\text{LF}$  state. From comparative TA experiments and comparisons to previous literature, we find that  $^1\text{MLCT}$  states are formed upon initial 400 nm excitation for both **1** and **2**.<sup>18,21,31</sup> The excited-state dynamics of both complexes share a similar subsequent relaxation step, indicated by a recovery of the GSB and a concomitant blue-shifting in the ESA by  $\sim 20$  nm (**Figures S21 and S24**). Similar relaxation profiles, including the blue-shifting ESA, have been observed in other first- and second-row transition metal complexes, including Ni(II)–bpy aryl halides.<sup>19,48</sup> The precise nature of the relaxation process is currently unclear and can be indicative of either vibrational cooling or an intersystem crossing between  $^1/3\text{MLCT}$  states. Both processes can occur on the time scale consistent with our data, and vibrational cooling can even mediate intersystem crossing to a  $^3\text{MLCT}$  state. We note that CASSCF/QD-NEVPT2 calculations predict multiple overlapping  $^1/3\text{MLCT}$  states that could be accessible (**Figure S28**); thus, we cannot unambiguously differentiate vibrational cooling vs intersystem crossing. Notably, the blue-shifting of the ESA has also been observed for Cu(I) bis-phenanthroline complexes and was associated with the flattening of the  $T_d$  Franck–Condon geometry in the excited-state Cu(II)\* on the picosecond time scale, which is also associated with intersystem crossing.<sup>49</sup> In the Ni(II)  $d^8$  systems studied here, an interconversion between square planar and pseudo- $T_d$  geometries near the Franck–Condon point of the excited-state  $^1\text{MLCT}$  surface might take place. Such behavior could yield significantly distinct  $^1\text{MLCT}$  lifetimes, as was observed in this work for flexible **1** ( $\tau_1 = \sim 400$  fs) and more constrained **2** ( $\tau_1 = \sim 3$  ps).

The excited-state dynamics of **1** and **2** are also distinct after accessing the relaxed  $^1/3\text{MLCT}$  excited state. Due to steric constraints in **2**, distortion to a pseudo- $T_d$  geometry is prohibited (**Figures 4.9 and S32**), which strongly destabilizes the  $^3\text{LF}$  state relative to the ground state, likely making it inaccessible from the MLCT excited-state manifold. From quantum chemical calculations, the optimized  $^3\text{LF}$  state of **1** is  $\sim 19$  kcal mol $^{-1}$  lower in  $\Delta G$  than the analogous  $^3\text{LF}$  state in **2**. As a consequence, while **1** relaxes from the MLCT excited-state manifold to a longer-lived  $^3\text{LF}$  state with a time constant of  $\sim 9$  ps, **2** exhibits

a prolonged  $^1/3$ MLCT excited state that relaxes back to the singlet ground state with a time constant of  $\sim 14$  ps. A similar structural control over excited-state dynamics has been quantified for Cu(I) bis-phenanthroline complexes, in which a combined experimental and computational approach determined that steric effects can provide up to  $\sim 20$  kcal mol $^{-1}$  in tuning excited-state potential energy surfaces, which further tunes the MLCT lifetime of those complexes over 4 orders of magnitude.<sup>50</sup>

### Geometric distortions of **1** and **2** upon $^3$ LF state formation

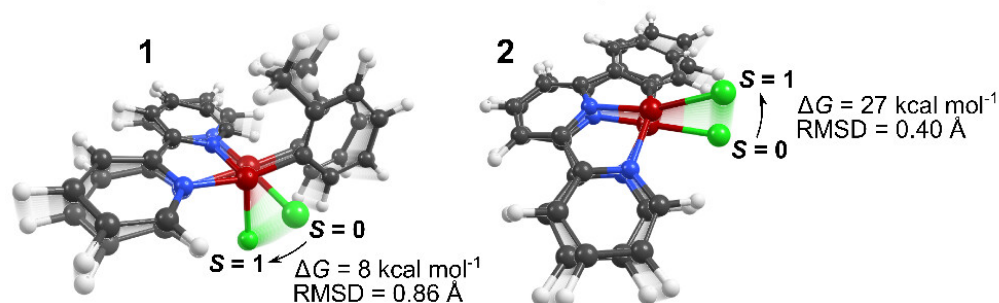


**Figure 4.9.** An overlay of DFT-optimized geometries of **1** and **2** in their ground-state singlet and triplet states, highlighting the prohibited distortion of **2** due to steric constraints.  $\Delta G$  was obtained from CASSCF/QD-NEVPT2 electronic energies (see section 2.1 of the Supporting Information); RMSD = root-mean-square deviation of atomic positions between superimposed structures of optimized singlet and triplet states.

Notably, despite the lack of  $^3$ LF state formation due to strong steric constraints, **2** still exhibits reactivity with electrophiles after photoirradiation. This reactivity suggests that access to the  $^3$ LF state may not be necessary for the generation of a reactive Ni(I) intermediate. We further note that the excited-state dynamics of **1** and **2** probed by TA are not affected by the addition of mesityl bromide, which indicates that the chemical reactivity with mesityl bromide occurs via a separate process, and reactive species are not observed as part of the excited-state dynamics probed by this experiment. This observation is reminiscent of the nature of the excited-state bond homolysis in compound **1** and related untethered complexes. Due to small quantum yields for homolysis, transient spectroscopies probe effectively unproductive, background excited-state relaxation processes that do not

result in Ni(I) intermediates and organic radicals. Similarly for **2**, the TA reports on MLCT relaxation but not excited-state bond homolysis.

The primary distinction between the unique excited-state dynamics of **1** and **2** lies in their geometric properties and excited-state distortions/constraints, which render **2** incapable of stabilizing  $^3\text{LF}$  excited states. We can also draw comparisons between the photophysics of **2** and the photophysics of other tethered Ni(II) species. A recent report by Wenger and co-workers investigated the excited-state behavior of a tethered Ni(II)–bpy aryl chloride complex with an  $\text{N}^{\wedge}\text{C}^{\wedge}\text{N}$  binding motif rather than  $\text{C}^{\wedge}\text{N}^{\wedge}\text{N}$  in **2**.<sup>51</sup> Analogous to **2**, upon 400 nm excitation, the  $\text{N}^{\wedge}\text{C}^{\wedge}\text{N}$  tethered complex accesses a  $^1\text{MLCT}$  excited state, which was proposed to undergo decay through another undefined-spin MLCT state to a  $^3\text{LF}$  state. The time constant associated with the first decay varies with solvent, ranging from  $\sim 700$  to 900 fs. This fast time constant accounts for the relaxation of both singlet and triplet MLCT manifolds. Furthermore, a solvent-dependent time constant associated with  $^3\text{LF}$  relaxation to the singlet ground state ranged from  $\sim 9.2$  to 14 ps. While the proposed excited-state decay pathway for the  $\text{N}^{\wedge}\text{C}^{\wedge}\text{N}$  tethered complex is similar to that proposed for untethered analogues,<sup>19</sup> the time constants appear comparable to those observed for **2** in this work. However, the authors hypothesized that the  $\text{N}^{\wedge}\text{C}^{\wedge}\text{N}$  isomer does not require distortion from square planar to pseudo- $T_d$  to stabilize a  $^3\text{LF}$  state. Here, we have observed a similar degree of geometric distortion upon optimization of the  $^3\text{LF}$  state in the  $\text{N}^{\wedge}\text{C}^{\wedge}\text{N}$  isomer and **2** (**Figure S33**). However, the smaller RMSD between the superimposed singlet and triplet structures of the former suggests that the  $\text{N}^{\wedge}\text{C}^{\wedge}\text{N}$  ligand remains more planar in the  $^3\text{LF}$  state, with the main distortion featuring a larger out-of-plane bending of the Ni–Cl bond. Therefore, it remains unclear whether the variance in accessing a  $^3\text{LF}$  state between the tethered isomers can be attributed to disparities in  $\text{C}^{\wedge}\text{N}^{\wedge}\text{N}$  vs  $\text{N}^{\wedge}\text{C}^{\wedge}\text{N}$  coordination or potential solvent effects on the excited-state dynamics. In **2**, the MLCT-based ESA feature decays monoexponentially with the same time constant as the recovery of the GSB, which allows us to associate the longer-lived time component as MLCT in origin, not  $^3\text{LF}$ . In both cases, the tethered isomers demonstrate significantly faster relaxation compared to untethered Ni(II)–bpy aryl halide analogues. Ultrafast X-ray spectroscopies may prove

useful for obtaining more precise mechanistic information regarding excited-state relaxation dynamics in tethered vs untethered complexes.

#### 4.4. Conclusions

We have compared covalently tethered, structurally constrained Ni(II)–bpy aryl halide complex **2** and its untethered analogue **1**, exploring the significant distinctions in their photochemical reactivity and excited-state dynamics. Key findings are as follows: (a) Unlike **1**, the tethered complex **2** exhibits prolonged stability under photoexcitation across a wide range of LED wavelengths, which indicates that excited-state bond homolysis products from **2** do not effectively accumulate over time. (b) The introduction of an electrophile during photoirradiation of **2** enables productive capture of a species capable of C(sp<sup>2</sup>)–Br activation, which we propose to be a Ni(I) intermediate based on a comparison to previous literature. This reactivity offers a promising avenue for enhancing nickel photoredox catalysis and refining reaction selectivity. (c) From concentration-dependent photochemical experiments in the presence of an electrophile, both **1** and **2** exhibit behavior consistent with reversible Ni(II)–C(aryl)  $\rightleftharpoons$  [Ni(I)···C(aryl)<sup>•</sup>] excited-state bond homolysis. (d) Distinct excited-state relaxation mechanisms occur in **1** vs **2**, which can be attributed to steric constraints introduced through the covalent linkage between the phenyl and bpy ligands, prohibiting the formation of a pseudo-*T<sub>d</sub>* geometry and access to <sup>3</sup>LF excited states.

Future investigations should focus on practical applications of the tethered complex in photoredox cross-coupling catalysis to assess its photochemical behavior under catalytic conditions and whether influences on Ni(I)–organic radical cage escape processes play an important role. Relatedly, exploring controlled Ni(I) generation holds the potential for enhancing reaction selectivity in organic synthesis. Further research into the impact of ligand substituents on the tethered bpy backbone, especially electron-withdrawing groups, may enable the use of lower-energy light and improve the stability of highly reactive intermediates, offering opportunities to tune reaction conditions in the nickel ground-state and photoredox catalysis.

#### 4.5. References

- (1) Chan, A. Y.; Perry, I. B.; Bissonnette, N. B.; Buksh, B. F.; Edwards, G. A.; Frye, L. I.; Garry, O. L.; Lavagnino, M. N.; Li, B. X.; Liang, Y.; Mao, E.; Millet, A.; Oakley, J. V.; Reed, N. L.; Sakai, H. A.; Seath, C. P.; MacMillan, D. W. C. Metallaphotoredox: The Merger of Photoredox and Transition Metal Catalysis. *Chem. Rev.* **2022**, *122* (2), 1485– 1542, DOI: 10.1021/acs.chemrev.1c00383.
- (2) Twilton, J.; Le, C.; Zhang, P.; Shaw, M. H.; Evans, R. W.; MacMillan, D. W. C. The Merger of Transition Metal and Photocatalysis. *Nat. Rev. Chem.* **2017**, *1* (7), 52, DOI: 10.1038/s41570-017-0052.
- (3) Skubi, K. L.; Blum, T. R.; Yoon, T. P. Dual Catalysis Strategies in Photochemical Synthesis. *Chem. Rev.* **2016**, *116* (17), 10035– 10074, DOI: 10.1021/acs.chemrev.6b00018.
- (4) Hopkinson, M. N.; Sahoo, B.; Li, J.-L.; Glorius, F. Dual Catalysis Sees the Light: Combining Photoredox with Organo-, Acid, and Transition-Metal Catalysis. *Chem. - A Eur. J.* **2014**, *20* (14), 3874– 3886, DOI: 10.1002/chem.201304823.
- (5) Larsen, C. B.; Wenger, O. S. Photoredox Catalysis with Metal Complexes Made from Earth-Abundant Elements. *Chem. - A Eur. J.* **2018**, *24* (9), 2039– 2058, DOI: 10.1002/chem.201703602.
- (6) Levin, M. D.; Kim, S.; Toste, F. D. Photoredox Catalysis Unlocks Single-Electron Elementary Steps in Transition Metal Catalyzed Cross-Coupling. *ACS Cent. Sci.* **2016**, *2* (5), 293– 301, DOI: 10.1021/acscentsci.6b00090.
- (7) Cheung, K. P. S.; Sarkar, S.; Gevorgyan, V. Visible Light-Induced Transition Metal Catalysis. *Chem. Rev.* **2022**, *122* (2), 1543– 1625, DOI: 10.1021/acs.chemrev.1c00403.
- (8) Tay, N. E. S.; Lehnher, D.; Rovis, T. Photons or Electrons? A Critical Comparison of Electrochemistry and Photoredox Catalysis for Organic Synthesis. *Chem. Rev.* **2022**, *122* (2), 2487– 2649, DOI: 10.1021/acs.chemrev.1c00384.
- (9) Till, N. A.; Tian, L.; Dong, Z.; Scholes, G. D.; MacMillan, D. W. C. Mechanistic Analysis of Metallaphotoredox C-N Coupling: Photocatalysis Initiates and Perpetuates Ni(I)/Ni(III) Coupling Activity. *J. Am. Chem. Soc.* **2020**, *142* (37), 15830– 15841, DOI: 10.1021/jacs.0c05901.

- (10) Qin, Y.; Sun, R.; Gianoulis, N. P.; Nocera, D. G. Photoredox Nickel-Catalyzed C-S Cross-Coupling: Mechanism, Kinetics, and Generalization. *J. Am. Chem. Soc.* **2021**, *143* (4), 2005–2015, DOI: 10.1021/jacs.0c11937.
- (11) Diccianni, J. B.; Diao, T. Mechanisms of Nickel-Catalyzed Cross-Coupling Reactions. *Trends Chem.* **2019**, *1* (9), 830–844, DOI: 10.1016/j.trechm.2019.08.004.
- (12) Diccianni, J.; Lin, Q.; Diao, T. Mechanisms of Nickel-Catalyzed Coupling Reactions and Applications in Alkene Functionalization. *Acc. Chem. Res.* **2020**, *53* (4), 906–919, DOI: 10.1021/acs.accounts.0c00032.
- (13) Cavalcanti, L. N.; Molander, G. A. Photoredox Catalysis in Nickel-Catalyzed Cross-Coupling. *Top. Curr. Chem.* **2016**, *374* (4), 39, DOI: 10.1007/s41061-016-0037-z.
- (14) Lin, C.-Y.; Power, P. P. Complexes of Ni(i): A “Rare” Oxidation State of Growing Importance. *Chem. Soc. Rev.* **2017**, *46* (17), 5347–5399, DOI: 10.1039/C7CS00216E.
- (15) Bismuto, A.; Finkelstein, P.; Müller, P.; Morandi, B. The Journey of Ni(I) Chemistry. *Helv. Chim. Acta* **2021**, *104* (12), e2100177, DOI: 10.1002/hlca.202100177.
- (16) Day, C. S.; Martin, R. Comproportionation and Disproportionation in Nickel and Copper Complexes. *Chem. Soc. Rev.* **2023**, *52* (19), 6601–6616, DOI: 10.1039/D2CS00494A.
- (17) Welin, E. R.; Le, C.; Arias-Rotondo, D. M.; McCusker, J. K.; MacMillan, D. W. C. Photosensitized, Energy Transfer-Mediated Organometallic Catalysis through Electronically Excited Nickel(II). *Science* **2017**, *355* (6323), 380–385, DOI: 10.1126/science.aal2490.
- (18) Shields, B. J.; Kudisch, B.; Scholes, G. D.; Doyle, A. G. Long-Lived Charge-Transfer States of Nickel(II) Aryl Halide Complexes Facilitate Bimolecular Photoinduced Electron Transfer. *J. Am. Chem. Soc.* **2018**, *140* (8), 3035–3039, DOI: 10.1021/jacs.7b13281.
- (19) Ting, S. I.; Garakyaraghi, S.; Taliaferro, C. M.; Shields, B. J.; Scholes, G. D.; Castellano, F. N.; Doyle, A. G. 3d-d Excited States of Ni(II) Complexes Relevant to Photoredox Catalysis: Spectroscopic Identification and Mechanistic Implications. *J. Am. Chem. Soc.* **2020**, *142* (12), 5800–5810, DOI: 10.1021/jacs.0c00781.

- (20) Shin, J.; Lee, J.; Suh, J.-M.; Park, K. Ligand-Field Transition-Induced C-S Bond Formation from Nickelacycles. *Chem. Sci.* **2021**, *12* (48), 15908– 15915, DOI: 10.1039/D1SC05113J.
- (21) Cagan, D. A.; Bím, D.; Silva, B.; Kazmierczak, N. P.; McNicholas, B. J.; Hadt, R. G. Elucidating the Mechanism of Excited-State Bond Homolysis in Nickel-Bipyridine Photoredox Catalysts. *J. Am. Chem. Soc.* **2022**, *144* (14), 6516– 6531, DOI: 10.1021/jacs.2c01356.
- (22) Yang, L.; Lu, H.-H.; Lai, C.-H.; Li, G.; Zhang, W.; Cao, R.; Liu, F.; Wang, C.; Xiao, J.; Xue, D. Light-Promoted Nickel Catalysis: Etherification of Aryl Electrophiles with Alcohols Catalyzed by a Ni(II)-Aryl Complex. *Angew. Chemie Int. Ed.* **2020**, *59* (31), 12714– 12719, DOI: 10.1002/anie.202003359.
- (23) Cagan, D. A.; Stroschio, G. D.; Cusumano, A. Q.; Hadt, R. G. Multireference Description of Nickel-Aryl Homolytic Bond Dissociation Processes in Photoredox Catalysis. *J. Phys. Chem. A* **2020**, *124* (48), 9915– 9922, DOI: 10.1021/acs.jpca.0c08646.
- (24) Newman-Stonebraker, S. H.; Raab, T. J.; Roshandel, H.; Doyle, A. G. Synthesis of Nickel(I)-Bromide Complexes via Oxidation and Ligand Displacement: Evaluation of Ligand Effects on Speciation and Reactivity. *J. Am. Chem. Soc.* **2023**, *145* (35), 19368– 19377, DOI: 10.1021/jacs.3c06233.
- (25) Ghosh, I.; Shlapakov, N.; Karl, T. A.; Düker, J.; Nikitin, M.; Burykina, J. V.; Ananikov, V. P.; König, B. General Cross-Coupling Reactions with Adaptive Dynamic Homogeneous Catalysis. *Nature* **2023**, *619* (7968), 87– 93, DOI: 10.1038/s41586-023-06087-4.
- (26) Tang, T.; Hazra, A.; Min, D. S.; Williams, W. L.; Jones, E.; Doyle, A. G.; Sigman, M. S. Interrogating the Mechanistic Features of Ni(I)-Mediated Aryl Iodide Oxidative Addition Using Electroanalytical and Statistical Modeling Techniques. *J. Am. Chem. Soc.* **2023**, *145* (15), 8689– 8699, DOI: 10.1021/jacs.3c01726.
- (27) Cavedon, C.; Gisbertz, S.; Reischauer, S.; Vogl, S.; Sperlich, E.; Burke, J. H.; Wallick, R. F.; Schrottke, S.; Hsu, W.; Anghileri, L.; Pfeifer, Y.; Richter, N.; Teutloff, C.; Müller-Werkmeister, H.; Cambié, D.; Seeberger, P. H.; Vura-Weis, J.; van der Veen, R. M.;

- Thomas, A.; Pieber, B. Intraligand Charge Transfer Enables Visible Light Mediated Nickel Catalyzed Cross Coupling Reactions. *Angew. Chemie Int. Ed.* **2022**, *61* (46), e202211433, DOI: 10.1002/anie.202211433.
- (28) Yang, L.; Yan, Y.; Cao, N.; Hao, J.; Li, G.; Zhang, W.; Cao, R.; Wang, C.; Xiao, J.; Xue, D. Ni(I)-Catalyzed Hydroxylation of Aryl Halides with Water under Thermal Catalysis. *Org. Lett.* **2022**, *24* (51), 9431–9435, DOI: 10.1021/acs.orglett.2c03840.
- (29) Müller, P.; Finkelstein, P.; Trapp, N.; Bismuto, A.; Jeschke, G.; Morandi, B. Nickel(I)-Phenolate Complexes: The Key to Well-Defined Ni(I) Species. *Inorg. Chem.* **2023**, *62* (41), 16661–16668, DOI: 10.1021/acs.inorgchem.3c01559.
- (30) Cagan, D. A.; Bím, D.; McNicholas, B. J.; Kazmierczak, N. P.; Oyala, P. H.; Hadt, R. G. Photogenerated Ni(I)-Bipyridine Halide Complexes: Structure-Function Relationships for Competitive C(Sp<sup>2</sup>)–Cl Oxidative Addition and Dimerization Reactivity Pathways. *Inorg. Chem.* **2023**, *62* (24), 9538–9551, DOI: 10.1021/acs.inorgchem.3c00917.
- (31) Vogt, N.; Sandleben, A.; Kletsch, L.; Schäfer, S.; Chin, M. T.; Vicic, D. A.; Hörner, G.; Klein, A. Role of the X Coligands in Cyclometalated [Ni(Phbpy)X] Complexes (HPhbpy = 6-Phenyl-2,2'-Bipyridine). *Organometallics* **2021**, *40* (11), 1776–1785, DOI: 10.1021/acs.organomet.1c00237.
- (32) Basu, A.; Gafney, H. D.; Streckas, T. C. Resonance Raman Spectra of Ruthenium(II) Complexes of Bipyridine and Substituted Bipyridines: Ground- and Excited-State Properties. *Inorg. Chem.* **1982**, *21* (6), 2231–2235, DOI: 10.1021/ic00136a021.
- (33) Ting, S. I.; Williams, W. L.; Doyle, A. G. Oxidative Addition of Aryl Halides to a Ni(I)-Bipyridine Complex. *J. Am. Chem. Soc.* **2022**, *144* (12), 5575–5582, DOI: 10.1021/jacs.2c00462.
- (34) Kalvet, I.; Guo, Q.; Tizzard, G. J.; Schoenebeck, F. When Weaker Can Be Tougher: The Role of Oxidation State (I) in P- vs N-Ligand-Derived Ni-Catalyzed Trifluoromethylthiolation of Aryl Halides. *ACS Catal.* **2017**, *7* (3), 2126–2132, DOI: 10.1021/acscatal.6b03344.

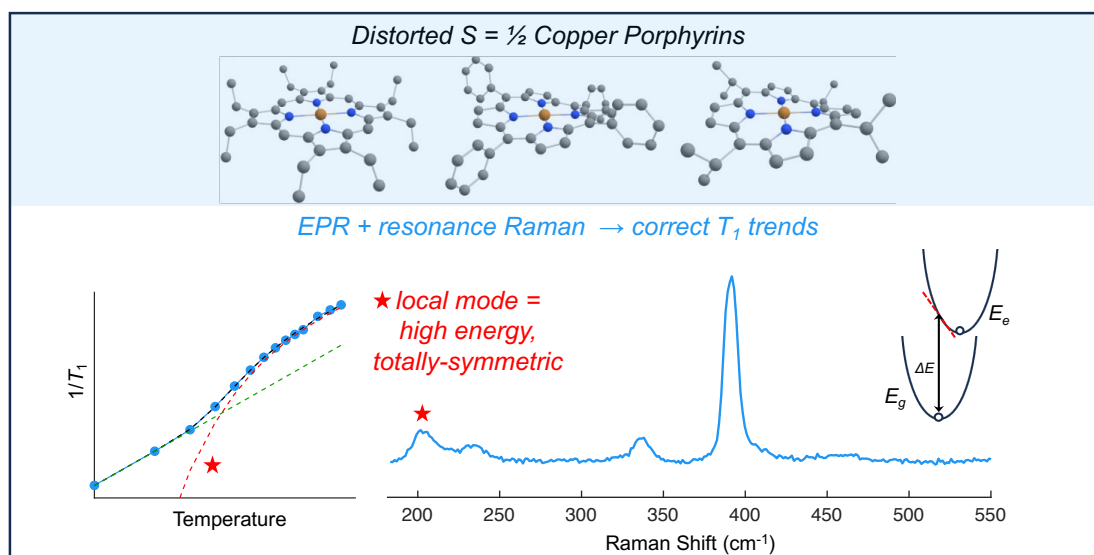
- (35) Na, H.; Mirica, L. M. Deciphering the Mechanism of the Ni-Photocatalyzed C-O Cross-Coupling Reaction Using a Tridentate Pyridinophane Ligand. *Nat. Commun.* **2022**, *13* (1), 1313, DOI: 10.1038/s41467-022-28948-8.
- (36) Klein, A.; Rausch, B.; Kaiser, A.; Vogt, N.; Krest, A. The Cyclometalated Nickel Complex [(Phbpy)NiBr] (Phbpy- = 2,2'-Bipyridine-6-Phen-2-Yl) - Synthesis, Spectroscopic and Electrochemical Studies. *J. Organomet. Chem.* **2014**, *774*, 86–93, DOI: 10.1016/j.jorganchem.2014.10.013.
- (37) Franck, J.; Rabinowitsch, E. Some Remarks about Free Radicals and the Photochemistry of Solutions. *Trans. Faraday Soc.* **1934**, *30* (0), 120–130, DOI: 10.1039/tf9343000120.
- (38) Klein, A.; Sandleben, A.; Vogt, N. Synthesis, Structure and Reactivity of Cyclometalated Nickel(II) Complexes: A Review and Perspective. *Proc. Natl. Acad. Sci. India Sect. A Phys. Sci.* **2016**, *86* (4), 533–549, DOI: 10.1007/s40010-016-0289-6.
- (39) Charboneau, D. J.; Huang, H.; Barth, E. L.; Germe, C. C.; Hazari, N.; Mercado, B. Q.; Uehling, M. R.; Zultanski, S. L. Tunable and Practical Homogeneous Organic Reductants for Cross-Electrophile Coupling. *J. Am. Chem. Soc.* **2021**, *143* (49), 21024–21036, DOI: 10.1021/jacs.1c10932.
- (40) Turro, R. F.; Wahlman, J. L. H.; Tong, Z. J.; Chen, X.; Yang, M.; Chen, E. P.; Hong, X.; Hadt, R. G.; Houk, K. N.; Yang, Y.-F.; Reisman, S. E. Mechanistic Investigation of Ni-Catalyzed Reductive Cross-Coupling of Alkenyl and Benzyl Electrophiles. *J. Am. Chem. Soc.* **2023**, *145* (27), 14705–14715, DOI: 10.1021/jacs.3c02649.
- (41) Gutierrez, O.; Tellis, J. C.; Primer, D. N.; Molander, G. A.; Kozlowski, M. C. Nickel-Catalyzed Cross-Coupling of Photoredox-Generated Radicals: Uncovering a General Manifold for Stereoconvergence in Nickel-Catalyzed Cross-Couplings. *J. Am. Chem. Soc.* **2015**, *137* (15), 4896–4899, DOI: 10.1021/ja513079r.
- (42) Lin, Q.; Spielvogel, E. H.; Diao, T. Carbon-Centered Radical Capture at Nickel(II) Complexes: Spectroscopic Evidence, Rates, and Selectivity. *Chem.* **2023**, *9* (5), 1295–1308, DOI: 10.1016/j.chempr.2023.02.010.

- (43) Lin, Q.; Fu, Y.; Liu, P.; Diao, T. Monovalent Nickel-Mediated Radical Formation: A Concerted Halogen-Atom Dissociation Pathway Determined by Electroanalytical Studies. *J. Am. Chem. Soc.* **2021**, *143* (35), 14196– 14206, DOI: 10.1021/jacs.1c05255.
- (44) Tsou, T. T.; Kochi, J. K. Mechanism of Oxidative Addition. Reaction of Nickel(0) Complexes with Aromatic Halides. *J. Am. Chem. Soc.* **1979**, *101* (21), 6319– 6332, DOI: 10.1021/ja00515a028.
- (45) Male, J. L.; Lindfors, B. E.; Covert, K. J.; Tyler, D. R. The Effect of Radical Size and Mass on the Cage Recombination Efficiency of Photochemically Generated Radical Cage Pairs. *J. Am. Chem. Soc.* **1998**, *120* (50), 13176– 13186, DOI: 10.1021/ja980911x.
- (46) Ma, P.; Wang, S.; Chen, H. Reactivity of Transition-Metal Complexes in Excited States: C–O Bond Coupling Reductive Elimination of a Ni(II) Complex Is Elicited by the Metal-to-Ligand Charge Transfer State. *ACS Catal.* **2020**, *10* (1), 1– 6, DOI: 10.1021/acscatal.9b03827.
- (47) Maity, B.; Scott, T. R.; Stroschio, G. D.; Gagliardi, L.; Cavallo, L. The Role of Excited States of LNiII/III(Aryl)(Halide) Complexes in Ni–Halide Bond Homolysis in the Arylation of Csp<sup>3</sup>–H Bonds. *ACS Catal.* **2022**, *12* (21), 13215– 13224, DOI: 10.1021/acscatal.2c04284.
- (48) Brown, A. M.; McCusker, C. E.; Carey, M. C.; Blanco-Rodríguez, A. M.; Towrie, M.; Clark, I. P.; Vlček, A.; McCusker, J. K. Vibrational Relaxation and Redistribution Dynamics in Ruthenium(II) Polypyridyl-Based Charge-Transfer Excited States: A Combined Ultrafast Electronic and Infrared Absorption Study. *J. Phys. Chem. A* **2018**, *122* (40), 7941– 7953, DOI: 10.1021/acs.jpca.8b06197.
- (49) Shaw, G. B.; Grant, C. D.; Shirota, H.; Castner, E. W.; Meyer, G. J.; Chen, L. X. Ultrafast Structural Rearrangements in the MLCT Excited State for Copper(I) Bis-Phenanthrolines in Solution. *J. Am. Chem. Soc.* **2007**, *129* (7), 2147– 2160, DOI: 10.1021/ja067271f.
- (50) Stroschio, G. D.; Ribson, R. D.; Hadt, R. G. Quantifying Entatic States in Photophysical Processes: Applications to Copper Photosensitizers. *Inorg. Chem.* **2019**, *58* (24), 16800– 16817, DOI: 10.1021/acs.inorgchem.9b02976.

- (51) Ogawa, T.; Wenger, O. S. Nickel(II) Analogues of Phosphorescent Platinum(II) Complexes with Picosecond Excited State Decay. *Angew. Chemie Int. Ed.* **2023**, *62* (46), e202312851, DOI: 10.1002/anie.202312851.

**PART II: SPIN RELAXATION**

**CHAPTER 5: DETERMINING THE KEY VIBRATIONS FOR SPIN  
RELAXATION IN RUFFLED CU(II) PORPHYRINS VIA RESONANCE  
RAMAN SPECTROSCOPY**



**Adapted with permission from:**

Kazmierczak, N. P.; Lopez, N. E.; **Luedecke, K. M.**; Hadt, R. G. “Determining the Key Vibrations for Spin Relaxation in Ruffled Cu(II) Porphyrins *via* Resonance Raman Spectroscopy.” *Chem. Sci.* **2024**, *15* (7), 2380. DOI: 10.1039/D3SC05774G.

Copyright 2024 The Royal Society of Chemistry.

## 5.1. Introduction

The rise of molecular quantum information science has placed new importance on developing molecules with long-lasting electron spin coherence times ( $T_2$ ), a parameter which sets the maximum length of time quantum information can be stored and processed.<sup>1</sup> At elevated temperatures, vibration-mediated spin relaxation ( $T_1$ ) limits the maximum attainable value of  $T_2$ ,<sup>2</sup> implying that vibrations effectively leak quantum information into the environment. While room-temperature electron spin coherence has been measured in a handful of  $S = 1/2$  systems,<sup>3–8</sup> other key classes of molecular qubits, such as the Cr(IV) optically addressable qubits, remain limited to sub-liquid nitrogen temperatures owing to  $T_1$ -limited  $T_2$ .<sup>9–12</sup> Thus, understanding the relationship between molecular geometric/electronic structure and spin relaxation rates remains a key mechanistic goal of molecular quantum information science. The number of thermally-accessible vibrational modes that could potentially contribute to spin relaxation renders such investigations theoretically and spectroscopically challenging.

One approach to build  $T_1$  mechanistic understanding is to employ theoretical models of the spin-relaxation process. Several models based on the easily handled spin Hamiltonian have been proposed, but crucially, multiple expressions have been used for the spin–phonon coupling coefficient (**Fig. 5.1A**). One can use derivatives of either the  $g$ -tensor<sup>2,13–17</sup> or the hyperfine tensor,<sup>15,16</sup> pick different elements of the tensor (on-diagonal only<sup>2,5,13,14</sup> vs. including off-diagonal<sup>15–17</sup>), and employ first<sup>13–15</sup> vs. second<sup>16,18</sup> derivatives. Depending on the theoretical choices made, different vibrational modes are predicted to dominate spin relaxation, ranging from ultra-low-energy  $e_g$  rotational modes ( $<50\text{ cm}^{-1}$ )<sup>19</sup> to totally symmetric metal–ligand stretching modes ( $>200\text{ cm}^{-1}$ ).<sup>2,13,14</sup> None of these spin Hamiltonian models can be considered mechanistically definitive due to two key issues: (1) derivatives of a spin Hamiltonian tensor do not constitute true matrix elements between spin states,<sup>20</sup> no matter how sophisticated the quantum master equation<sup>21</sup> used to handle the rate calculations, and (2) no spin Hamiltonian model successfully accounts for  $T_1$  anisotropy, which instead requires analysis of spin–orbit wavefunctions.<sup>20</sup> At best, spin Hamiltonian models can predict the average temperature-dependent  $T_1$  over all molecular orientations, functioning as a proxy for the true spin–orbit

mechanism.<sup>20</sup> Further discrepancies arise when comparing the theoretically predicted temperature scaling of  $T_1$  to experiment. On the basis of ultra-low-energy modes, contemporary *ab initio* models commonly predict flat, single-exponent power law behavior<sup>19</sup> for temperature-dependent  $T_1$ . However, experimental log–log plots of  $1/T_1$  vs. temperature display marked curvature for most  $S = \frac{1}{2}$  molecular qubits, which has been interpreted by local mode fitting to indicate the contribution of molecular vibrational modes  $>100 \text{ cm}^{-1}$  that give rise to a nonconstant power law exponent.<sup>14,22,23</sup> Experimentally parameterized  $T_1$  models have successfully reproduced this curvature for high-symmetry Cu(II) and V(IV) complexes,<sup>14</sup> but the curvature is not successfully predicted by *ab initio* models that emphasize ultra-low-energy modes.<sup>19</sup> We conclude that *ab initio* prediction of  $T_1$  in  $S = \frac{1}{2}$  molecular qubits has not yet achieved satisfactory agreement with experimental data.

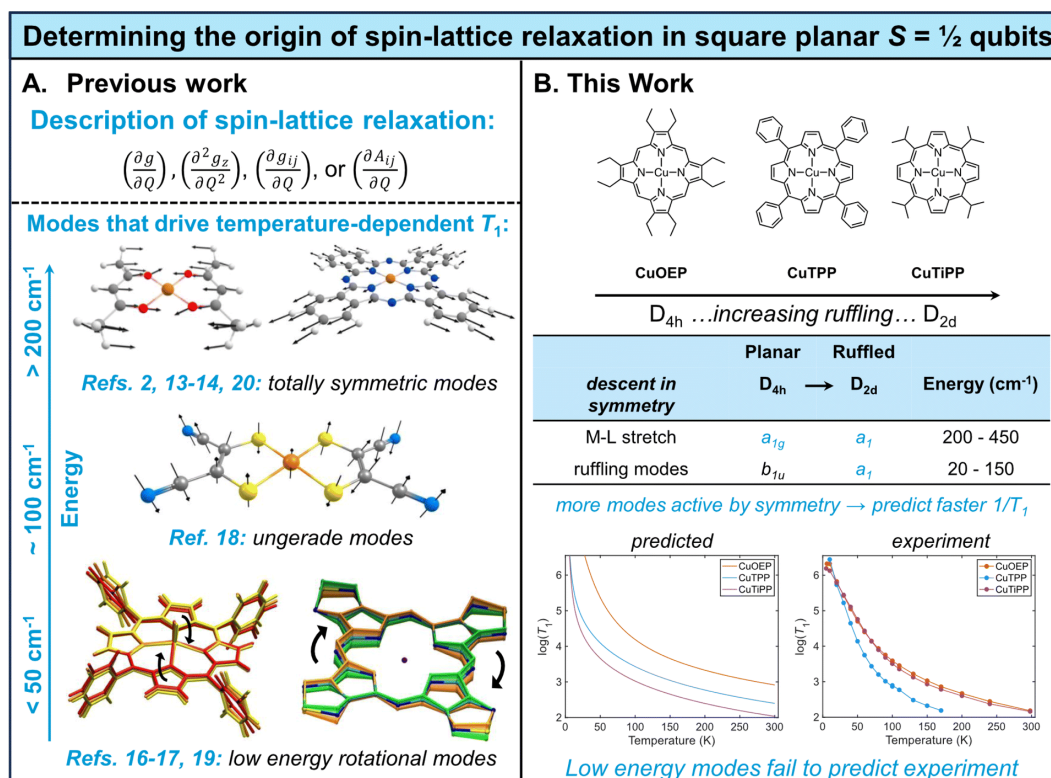


**Figure 5.1.** Mechanistic studies of spin–lattice relaxation in  $S = \frac{1}{2}$  qubits. (A) Previous theoretical studies have employed a variety of models for molecular spin–phonon

coupling, leading to disparate predictions of modes with different energies and symmetries driving spin relaxation. Figures adapted with permission from refs. 17–20. **(B)** This work systematically probes the effect of the  $b_{1u}$  ruffling distortion on spin relaxation in a series of copper porphyrins, finding that existing theory systematically overestimates the contribution of low-energy ruffling modes.

Alternatively, mechanistic understanding may be developed from experimentally-determined  $T_1$  structure–property relationships. While relatively few such relationships have been explored in detail, one of the best-established connections has been demonstrated between the degree of first coordination sphere planarity and  $T_1$  in four-coordinate Cu(II)  $S = 1/2$  molecular qubits.<sup>2</sup> Two limiting geometries are possible: square planar ( $D_{4h}$ ), in which the opposing L–M–L bond angle is  $180^\circ$ , and tetrahedral ( $T_d$ ), in which the opposing L–M–L bond angle is  $109.5^\circ$ . From the  $D_{4h}$  geometry, ligated atoms can undergo distortion along the  $b_{2u}$  bending mode, which lowers the point group to  $D_{2d}$  and systematically decreases the L–M–L angle from  $180^\circ$  toward  $109.5^\circ$ . It has been experimentally demonstrated that planar structures have longer spin lifetimes (long  $T_1$ ) than  $b_{2u}$ -distorted structures.<sup>5,23</sup> This result can be understood via application of group theory selection rules to the spin–phonon coupling problem.<sup>13,14</sup> In order for a vibrational mode to cause spin relaxation by altering the  $g$  value, it must transform as either a totally symmetric vibrational mode ( $a_1$  or  $a_{1g}$ ) or an excited-state Jahn-Teller mode. In the  $D_{4h}$  geometry, the  $b_{2u}$  bending mode does not satisfy these symmetry requirements. However, once the equilibrium structure has been distorted along the bending motion in the  $D_{2d}$  point group, the bending mode now transforms as  $a_1$  and can induce spin relaxation, as confirmed by calculation of  $dg/dQ$  spin–phonon coupling coefficients.<sup>13</sup> This specific relationship illustrates a general principle: when a high-symmetry equilibrium structure is distorted along a non-totally-symmetric vibrational mode, that mode transforms as the totally symmetric representation in the new point group (**Figure 5.1B**, ESI Section 4C) and can cause spin relaxation.<sup>14</sup>

Metalloporphyrins offer an attractive platform for extending  $T_1$  structure–property relationships to new types of molecular geometries. Depending on the steric hindrance and

substitutional pattern of peripheral moieties, porphyrins may adopt equilibrium geometries with saddled ( $b_{2u}$ ), ruffled ( $b_{1u}$ ), domed ( $a_{2u}$ ), or waved ( $e_g$ ) distortions, where the labels indicate the symmetry of the distorting vibrational mode in the  $D_{4h}$  point group.<sup>24</sup> The saddling distortion is equivalent to the same first coordination sphere bending distortion to  $D_{2d}$  described above (**Figures 5.2B and C**). By contrast, the  $b_{1u}$  ruffling distortion (**Figures 5.2B and C**) also results in a  $D_{2d}$  equilibrium geometry, but the first coordination sphere remains completely unaltered (**Figure 5.2A**). Instead, the porphyrin meso carbons are distorted above and below the plane of the first coordination sphere, rendering ruffling a secondary sphere structural distortion. By analogy to the  $b_{2u}$  bending mode argument, the  $b_{1u}$  ruffling mode will transform as  $a_1$  in the  $D_{2d}$  distorted point group, opening up the possibility of contributions to spin relaxation (ESI Section 4C). Ruffling modes in porphyrins exist in the ultra-low-energy range ( $\sim 50 \text{ cm}^{-1}$ ), indicating that ruffled  $S = \frac{1}{2}$  porphyrins may show a decisive, unique contribution of low-energy modes to  $T_1$ .

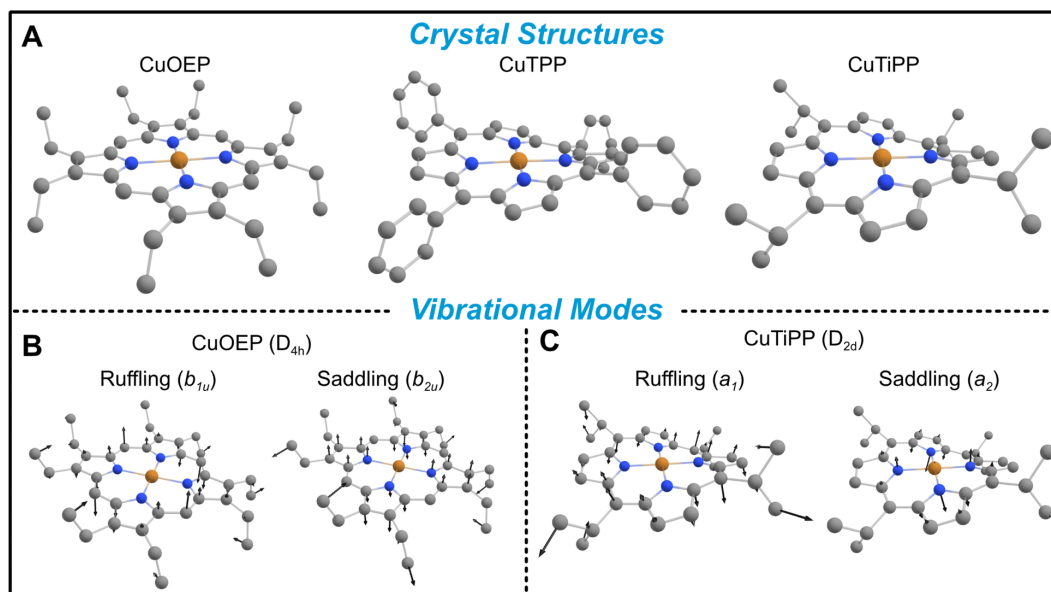


**Figure 5.2.** Geometries of ruffled metalloporphyrins. (A) Crystal structures demonstrate increasing static ruffling in the series  $\text{CuOEP} < \text{CuTPP} < \text{CuTiPP}$ . (B) Representative ruffling and saddling vibrational modes for CuOEP transform as non-totally-symmetric irreducible representations (irreps) due to the planar  $D_{4h}$  point group (ethyl groups neglected). Only the saddling mode alters the first coordination sphere geometry. (C) The

static distortion of CuTiPP causes the ruffling vibration to transform as the totally-symmetric irrep in the new  $D_{2d}$  point group, while the saddling vibration remains non-totally-symmetric. H atoms are omitted for clarity.

In this study, we measure temperature-dependent  $T_1$  *via* pulse electron paramagnetic resonance (EPR) on a series of three Cu(II) metalloporphyrins (CuP) (**Figures 5.1B and 5.2A**): copper octaethylporphyrin (CuOEP), copper tetraphenylporphyrin (CuTPP), and copper tetraisopropylporphyrin (CuTiPP). CuOEP possesses a planar crystal structure, while CuTPP and CuTiPP exhibit increasing degrees of the ruffling distortion (**Figure 5.2A**). Computational modeling via density functional theory (DFT) suggests that  $T_1$  times should decrease with increasing ruffling distortion. However, experimental  $T_1$  measurements do not trend with ruffling: the planar CuOEP and highly ruffled CuTiPP display robust room-temperature coherence while the moderately ruffled CuTPP does not. The breakdown of the computational analysis can be attributed to an overemphasis of the lowest-energy ruffling mode. We then employ resonance Raman (rR) spectroscopy to detect the vibrational modes driving spin relaxation across this series and find a set of symmetric stretching vibrations in the 200–300  $\text{cm}^{-1}$  region that trend with the experimentally observed  $T_1$ . Our results demonstrate that ultra-low-energy modes do not drive spin relaxation in copper porphyrins, thereby distinguishing between conflicting theoretical models of spin relaxation (**Figure 5.1A**).

## 5.2. Results

To quantify the amount of distortion in a given metalloporphyrin crystal structure, we applied the normal coordinate structural decomposition (NSD) developed by Shelnut<sup>25</sup> and implemented in the program by Kingsbury and Senge.<sup>24</sup> CuOEP was chosen as the undistorted control compound, as it displays no tendency towards ruffling and only slight amounts of waving (**Table 5.1**). The distorted ruffled structures were chosen according to two criteria: (1) ruffling should be by far the largest distortion of the porphyrin, and (2) there must exist a diamagnetic host matrix of comparable distortions for preparation of EPR solid-state dilution samples. CuTPP and CuTiPP satisfy criterion (1), with CuTPP

having only a small secondary saddling distortion and CuTiPP having a very small secondary waving distortion. Regarding criterion (2), the corresponding Ni(II) porphyrins both display dominant ruffling distortions. The NiTPP matrix is closely matched to the CuTPP structure in both the primary magnitude of ruffling and the secondary saddling, while the NiTiPP matrix displays somewhat increased ruffling over the Cu structure (2.03 vs. 1.35) and an additional saddling distortion (0.46 vs. 0.00). These metrics indicate that the ruffling distortion increases in the series CuOEP < CuTPP < CuTiPP. Note that metalloporphyrins can crystallize in multiple phases: while the ruffled structure for CuTPP is the more common polymorph in the Cambridge Structural Database,<sup>26–28</sup> there also exist two planar polymorphs.<sup>29,30</sup> Additionally, we obtained a new ruffled solvate crystal phase for CuTiPP through single crystal X-ray diffraction (ESI Section 2C). We confirmed that all EPR sample preparations in this work adhered to the ruffled (or, for CuOEP and ZnOEP, planar) geometries via powder X-ray diffraction (PXRD) and Rietveld refinement for comparison to the single crystal structures (ESI Section 2B, 4B). Good EPR sample agreement with the polymorphs used for the NSD analysis in **Table 5.1** was found in all cases.

**Table 5.1.** Normal coordinate structural decomposition analysis of porphyrin distortions

<b>Distortion mode</b>	<b>Ruffling (<math>b_{1u}</math>)</b>	<b>Saddling (<math>b_{2u}</math>)</b>	<b>Doming (<math>a_{2u}</math>)</b>	<b>Waving (<math>e_g(x)</math>)</b>	<b>Waving (<math>e_g(y)</math>)</b>
CuOEP	0.00	0.00	0.00	0.11	0.05
CuTPP	1.18	0.22	0.00	0.00	0.00
CuTiPP	1.35	0.00	0.00	0.00	0.11
ZnOEP	0.00	0.00	0.00	0.16	0.06
NiTPP	1.27	0.27	0.00	0.00	0.00
NiTiPP	2.03	0.46	0.03	0.09	0.10

Temperature-dependent  $T_1$  measurements were acquired for all three CuP species (**Figure 5.3**), prepared as 1% solid-state powder dilutions in the corresponding isostructural diamagnetic host (**Table 5.1**). Inversion recovery traces were acquired at field

positions corresponding to both perpendicular (**Figure 5.3B**) and parallel (**Figure 5.3C**) orientations.<sup>20</sup> CuTPP exhibits the fastest spin relaxation of all CuP species at both field positions, with a particularly distinct relaxation trend at the perpendicular position. The comparatively fast spin relaxation is consistent with previous studies on Ti(III)/CuTPP bimetallic and monometallic congeners in solution,<sup>31</sup> as well as CuTPP embedded in a metal–organic framework (MOF),<sup>32,33</sup> which did not observe room-temperature coherence for CuTPP. CuOEP exhibits the slowest relaxation (i.e., longest  $T_1$  time) at the perpendicular position, while CuTiPP exhibits the slowest relaxation at the parallel position; the orientation-averaged  $1/T_1$  values are very similar for CuOEP and CuTiPP (**Figure S36**). Observer position differences in spin relaxation point to the presence of  $T_1$  anisotropy for the three CuP species.  $T_1$  anisotropy arises from the presence of anisotropic minority spin contributions in the ground-state spin–orbit wavefunction and how they are modulated by totally symmetric vibrations.<sup>20</sup> Note that the  $T_1$  values for all three porphyrins are quite similar at 20 K but diverge as temperature increases, indicating that higher-energy molecular vibrational modes are responsible for the differences between the compounds. Note also that CuOEP and CuTiPP display room-temperature (297 K) coherence, with  $T_1$  and  $T_m$  (the phase memory time<sup>2</sup>) of 185 ns and 87 ns for CuOEP and 145 ns and 50 ns for CuTiPP at perpendicular orientations. To the best of our knowledge, room-temperature electron spin coherence has only been demonstrated in one previous CuN<sub>4</sub> molecular qubit, Cu(tmtaa),<sup>5</sup> and is not observed for copper phthalocyanine (CuPc).<sup>22</sup> CuTPP displays an extremely weak spin echo at room temperature, with  $T_1$  and  $T_m$  of 60 and 49 ns at the perpendicular position. No echo was detectable at the CuTPP parallel position, and a room-temperature echo-detected field sweep could not be acquired. As such, we do not consider this signal robust enough for designation of CuTPP as a room-temperature coherent molecular qubit.

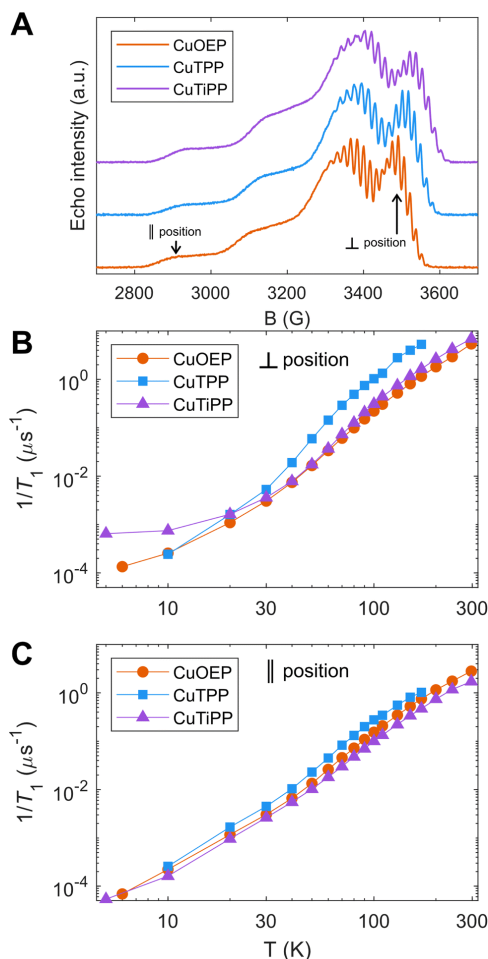


**Figure 5.3.** Temperature-dependent  $T_1$  by pulse EPR X-band inversion recovery in 1% solid state powder dilutions of CuOEP in ZnOEP, CuTPP in NiTPP, and CuTiPP in NiTiPP. (A) Echo-detected field sweeps, with field positions selective for parallel and perpendicular molecular orientations indicated for CuOEP. The analogous field positions are chosen for CuTPP and CuTiPP. (B) Perpendicular position spin relaxation rates. (C) Parallel position spin relaxation rates

Since  $1/T_1$  increases in the order  $\text{CuOEP} = \text{CuTiPP} \ll \text{CuTPP}$ , while ruffling increases in the order  $\text{CuOEP} < \text{CuTPP} < \text{CuTiPP}$ , the results of **Figure 5.3** do not support the hypothesis that increased ruffling distortion activates new channels for spin relaxation. To examine the theoretical underpinnings of this notion, we performed molecular spin-phonon coupling calculations according to a previously published procedure to predict

$1/T_1$  traces (**Equation 5.1**).<sup>14</sup> The normal-mode derivatives of the principal values of the  $g$ -tensor,  $dg/dQ$ , were averaged to obtain the spin–phonon coupling coefficients, thereby modeling the average  $1/T_1$  relaxation across all orientations. Thermal weighting was applied via a two-phonon Green's function to model the temperature dependence of the Raman spin relaxation process.<sup>16</sup> An experimentally calibrated proportionality constant of  $A = 1.01 \times 105 \mu\text{s}^{-1}$  was used to convert the  $1/T_1$  simulations into absolute rates.<sup>14</sup> This model has been shown to correctly predict the  $T_1$  log–log slope of the molecular qubits CuPc and VOPc, as well as correctly ordering the relative  $T_1$  for a series of four Cu(II) and V(IV) sulfur and selenium-ligated qubits.<sup>14</sup>

$$\frac{1}{T_1} = A \sum_{i=1}^{3N-6} \sum_{j=x,y,z} \frac{1}{3} \left( \frac{\partial g_j}{\partial Q_i} \right)^2 \frac{\exp[E_i/k_B T]}{(\exp[E_i/k_B T] - 1)^2} \quad (5.1)$$

Theoretical calculations predict that  $1/T_1$  should increase in the order CuOEP < CuTPP < CuTiPP (**Figure 5.4A**; see **Figure S51** for an overlay of theory and experiment). This trend agrees with the order of increasing ruffling, but it does not agree with the experimental  $T_1$  ordering. To understand the origin of the trend in the calculations, the individual vibrational mode contributions to  $1/T_1$  are plotted for CuOEP (**Figure 5.4B**) and CuTiPP (**Figure 5.4C**); ruffled CuTPP follows similar behavior to ruffled CuTiPP (**Figure S52**). The contributions from each normal mode are additive towards the total rate of spin relaxation. All mode contributions have the same functional shape in accordance with the thermal weighting function, with two degrees of freedom: (1) a larger energy of the vibrational mode translates the  $1/T_1$  contribution to the right, since the mode will not be thermally populated until higher temperatures, and (2) a larger  $dg_i/dQ$  value shifts the  $1/T_1$  contribution up on the plot, indicating that it mediates faster spin relaxation. For CuOEP, the calculated relaxation rate from  $\sim 30$ – $70$  K is set by low-energy vibrational modes, mostly of an  $e_g$  rotational character with small amounts of symmetric stretch mixed in due to the waving distortion in CuOEP (**Table 5.1**). However, at 100 K and above, totally symmetric stretch modes take over the dominant contribution to spin relaxation (green lines, **Figures 5.4B** and **S38–S40, S54A**). By contrast, spin relaxation for CuTiPP

is predicted to be dominated by a single low-energy ruffling mode at  $26\text{ cm}^{-1}$  (Fig. S46) over the entire temperature range studied (yellow lines, **Figure 5.4C**), which almost exactly matches the total  $1/T_1$  calculated trace. The contribution from other modes, including the totally symmetric stretch, is predicted to be  $<15\%$  (**Figure S54C**). Therefore, molecular spin–phonon coupling calculations predict that the low-energy ruffling modes should dominate the  $1/T_1$  for the ruffled porphyrins, and the absence of these distortion-activated modes in CuOEP should lead to a longer calculated spin lifetime. The room-temperature coherence of CuTiPP contradicts this prediction.

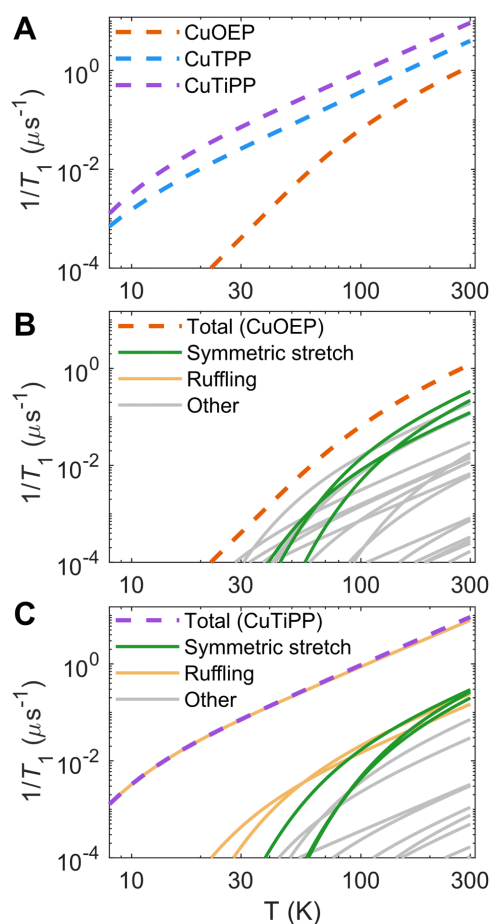


**Figure 5.4.** Calculated spin relaxation rates  $1/T_1$  for the Cu porphyrin series. **(A)** Total calibrated relaxation rates. **(B)** Breakdown of individual vibrational mode contributions for planar CuOEP. Symmetric stretching modes dominate  $T_1$  for  $T \geq 100\text{ K}$ , while ruffling mode contributions are negligible. **(C)** Breakdown of individual vibrational mode

contributions for ruffled CuTiPP. A single low-energy ( $26\text{ cm}^{-1}$ ) ruffling mode dominates the calculated  $1/T_1$  over the entire temperature range. Individual mode contributions are additive on a linear  $y$ -axis scale.

To determine the source of this discrepancy, we analyzed the temperature-dependent log–log slope of  $1/T_1$ . For a single power law process, such as those predicted by the Debye model for acoustic phonon spin relaxation,<sup>34</sup> the log–log slope should be constant. This behavior is often observed in experimental  $T_1$  for inorganic lattices where the acoustic phonon branches drive  $T_1$  over the entire Raman process temperature range.<sup>34,35</sup> However, variation in the log–log slope with temperature is common for molecular complexes. This behavior can originate from either (1) a crossover between two different spin relaxation processes (such as acoustic phonon relaxation vs. molecular vibration/local mode relaxation), or (2) the thermal population of higher-energy molecular vibrations, for which the innate spin relaxation contribution does not follow a power law form (**Equation 5.1**).<sup>14</sup> In the first case, a sharp increase occurs in the log–log slope with increasing temperature, as a process that scales weakly with temperature gives way to a process that scales more strongly with temperature. In the second case, a smooth decrease occurs in the log–log slope with increasing temperature due to the thermal weighting functional form. The curvature of the log–log  $1/T_1$  can then be used to pinpoint the energy of the contributing molecular vibration. Higher-energy molecular vibrations display a larger and temperature-dependent log–log slope even at elevated temperatures. In contrast, the log–log slope of a low-energy molecular vibration flattens out towards a constant value of 2 in the high temperature limit ( $k_bT \gg E_{vib}$ ), owing to the asymptotic behavior of the two-phonon Green's function.

Both CuOEP and CuTiPP display a temperature-dependent log–log slope (**Figures 5.5A and B**), which starts at a minimum below 10 K for the one-phonon direct process, peaks sharply at a value of  $\sim 4$  at  $\sim 60$  K, and then diminishes gradually towards  $\sim 2.5$  at room temperature. The sharp increase from 10–60 K experimentally indicates a change in the relaxation process (case 1), wherein two-phonon scattering from a higher-energy molecular vibration ( $>60$  K) takes over from acoustic/pseudoacoustic phonons ( $<30$  K).

The gradual decrease from 60 K towards room temperature indicates that one or more molecular vibrational modes controls spin relaxation over this region (case 2). By comparing these slopes to those of the theoretical calculations (**Figure 5.4**), the origin of the discrepancies with experiment can be ascertained. The calculated  $T_1$  log–log slope for CuOEP matches the experimental behavior, which can be attributed in the calculation to the population of totally symmetric stretch modes above 60 K (**Figures 5.4B** and **5.5A**). Note that the calculations do not include acoustic phonons, so the divergence of the calculated log–log slope below 20 K is expected. However, the calculated  $T_1$  for CuTiPP displays a qualitatively incorrect log–log slope of 2 throughout the entire temperature range, while the experimental log–log slope peaks at a value of  $\sim 4.5$  at 60 K. The calculated log–log slope of 2 arises from the  $26\text{ cm}^{-1}$  ruffling mode (**Figure 5.5B**), which is predicted to dominate spin relaxation across all temperatures. A similar disagreement arises for CuTPP due to the same ruffling mode phenomenon (**Figures S53** and **S55**). We conclude that the calculated spin relaxation for CuOEP is in agreement with experiment, but the calculated spin relaxation for CuTiPP and CuTPP is incorrect due to overemphasis on the low-energy ruffling modes. Evidently, the ultra-low-energy modes do not dominate spin relaxation in experiment.

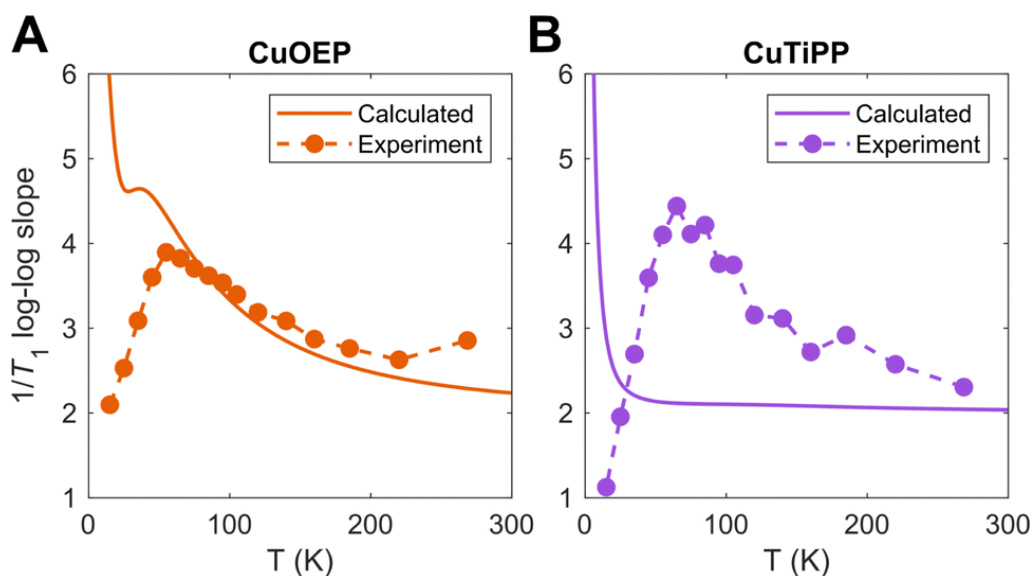


**Figure 5.5.** Calculated vs. experimental  $1/T_1$  log–log slopes for (A) CuOEP and (B) CuTiPP

To experimentally ascertain the energy range of the vibrational modes that drive spin relaxation, local mode fits<sup>22</sup> to the  $1/T_1$  data (**Figures 5.6A–C**) were carried out according to **Equation 5.2**. The least-squares fit was performed on the log–log data for equivalent residuals weighting across the entire temperature range.

$$\frac{1}{T_1} = aT^n + b \frac{\exp[E_{loc}/k_B T]}{(\exp[E_{loc}/k_B T] - 1)^2} \quad (5.2)$$

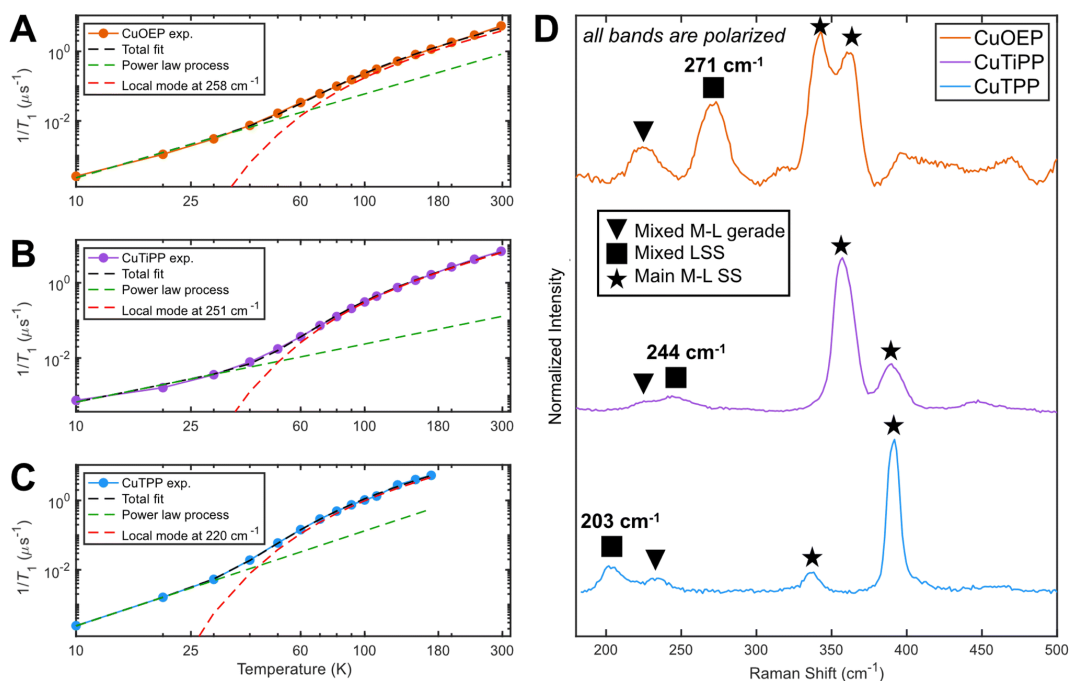


**Figure 5.6.** Determination of the dominant vibrational mode energy for spin relaxation. Local mode fitting at the perpendicular observer position according to **eqn (5.1)** for (A) CuOEP, (B) CuTiPP, and (C) CuTPP. (D) Resonance Raman spectroscopy obtained via 457.9 nm excitation (Soret preresonance enhancement). CuOEP collected in  $\text{CS}_2$  at room temperature, while CuTiPP and CuTPP collected in  $\text{C}_6\text{H}_6$  at room temperature; all samples are at a concentration of 2 mM. All peak positions are accurate to within  $5 \text{ cm}^{-1}$ .

The power law term accounts for a combination of the one-phonon direct process plus two-phonon Raman relaxation operating on low-energy phonons; combining these reduces the number of free parameters to avoid overfitting. Lower temperature measurements (<10 K) would likely be needed to isolate the direct process contribution. It is well established that the Raman process in molecular solids need not follow the Debye model  $T^9$  scaling,<sup>36</sup> so a variable exponent  $n$  is included. The second term has the same functional form as the two-phonon Green's function used for thermal weighting of molecular vibrational modes. In effect, this fitting postulates a single molecular vibration of energy  $E_{\text{loc}}$  capable of explaining the high-temperature  $T_1$  values, while allowing for an unresolved collection of weakly-coupled low-energy modes to determine the low-temperature  $T_1$  values. All fits yield a local mode energy between 200–270  $\text{cm}^{-1}$ , which fall in the energetic range of bond-stretching vibrational modes. This analysis indicates that a similar type of vibrational mode likely determines  $T_1$  in all three porphyrins. The fitted energy for CuTPP is lower than the fitted energies for CuOEP or CuTiPP, matching the room-temperature coherence observation for CuOEP and CuTiPP but not CuTPP. Local mode fitting on  $T_1$  values collected at the parallel field position reinforces that the local mode energy for CuTPP is distinct from, and lower than, the mode energies for CuOEP and CuTiPP (Table S7). The local mode energies  $E_{\text{loc}}$  correlate better with the observed  $T_1$  values than the coupling prefactor  $b$ , suggesting that vibrational mode energy shifts are principally responsible for the different  $T_1$  values across the compound series (Table S8).

rR spectroscopy was employed to identify vibrational modes in this energy range that could participate in spin–phonon coupling. Owing to selection rules of Raman scattering, only *gerade* modes are visible in centrosymmetric complexes. Furthermore, the A-term mechanism of Soret-band rR intensity enhancement selectively excites totally symmetric  $a_1/a_{1g}$  modes,<sup>37,38</sup> which are precisely those modes predicted by group theory to have the correct symmetry for driving spin relaxation.<sup>14</sup> rR spectra for all three compounds display four main bands in the 200–400  $\text{cm}^{-1}$  region, including two bands between 200–300  $\text{cm}^{-1}$  (**Figure 5.6D**). Crucially, these latter bands appear lower in energy for CuTPP than for CuOEP or CuTiPP, in agreement with the relative rates of spin relaxation. All bands

display a depolarization ratio less than 0.75 (**Figures S22–S24**), indicating at least some component of totally symmetric motion is present. The band positions in the solution-phase data are consistent within  $8\text{ cm}^{-1}$  of rR spectra acquired in the solid state and display similar relative resonance enhancement (**Table S2** and **Figure S25**), indicating these reflect the vibrational structure present in the EPR samples as well. DFT frequency calculations of vibrations with Raman intensity display very good agreement with the experimental spectra and enable the assignment of the  $300\text{--}400\text{ cm}^{-1}$  bands to totally symmetric metal–ligand stretching modes (ESI Section 3C). The  $200\text{--}300\text{ cm}^{-1}$  bands contain one instance of a mixed ligand symmetric stretch (LSS) and one instance of a mixed metal–ligand gerade mode with a principal contribution from non-totally symmetric motion. At least some symmetric motion must be admixed to account for the observation that all bands are polarized. Note the ordering of these latter two modes changes between the three CuP species.

Owing to the spin–phonon coupling group theory selection rule for totally symmetric vibrations, the mixed LSS mode energies were extracted from the rR spectra and compared with the local mode fits. Good agreement is found (**Table 5.2**), showing a  $>40\text{ cm}^{-1}$  distinction between the low-energy CuTPP LSS mode ( $203\text{ cm}^{-1}$ ) and those of CuOEP ( $271\text{ cm}^{-1}$ ) and CuTiPP ( $244\text{ cm}^{-1}$ ). This trend indicates that the energetic positioning of the LSS mode can explain the temperature-dependent  $T_1$  results for the three CuP systems. In addition, the presence of a minor saddling distortion for CuTPP but not CuOEP or CuTiPP (**Table 5.1**) may lead to enhanced spin–phonon coupling, as saddling motions are known to be activated for spin relaxation via a first coordination sphere distortion. Porphyrin saddling contributions to  $T_1$  will be analyzed in more detail in a future study. We conclude that high-energy totally symmetric stretch modes, and not low-energy ruffling modes, control the relative  $T_1$  ordering for CuOEP, CuTiPP, and CuTPP above 60 K.

**Table 5.2.** Positions of local mode energies and Raman mixed ligand symmetric stretch peaks

Compound	Perpendicular orientation local mode (cm <sup>-1</sup> )	Raman mixed LSS mode (cm <sup>-1</sup> )
CuOEP	258	271
CuTiPP	251	244
CuTPP	220	203

### 5.3. Discussion

The failure of computational spin relaxation models to predict the correct high-energy stretching vibrational modes is not a unique feature of ruffled porphyrins. In several cases, molecular spin–phonon coupling models seem to have a bias toward over-emphasizing low-energy modes, leading to predictions of ultra-low-energy vibrations dominating  $T_1$ . However, such assignments often fail to account for the temperature-dependent  $T_1$  curvature and log–log slope changes, such as in the case of *ab initio* modeling of vanadyl tetraphenylporphyrin (VOTPP).<sup>19</sup> Thus, such theoretical claims of low-energy phonon dominance should be treated with significant caution.

The origins of this computational low-energy bias are unclear, but likely relate to some of the approximations used to build the models. One possibility is that gas-phase DFT overestimates the amplitudes of low-energy vibrational modes, which should be more constrained in the solid-state. However, condensed-phase phonon calculations retain the same bias toward low-energy modes.<sup>19</sup> Additionally, the use of full- $g$ -tensor  $dg_{ij}/dQ$  values for spin Hamiltonian matrix elements may overestimate the coupling of certain types of low-energy modes, such as  $e_g$  rotations of the first coordination sphere, that do not dynamically change the total amount of minority spin mixing through the magnitude of spin–orbit coupling. Incorporation of spin–orbit coupling spin-flip matrix elements into *ab initio*  $T_1$  modeling with quantum master equations may remedy this difficulty.

Experimentally, this work shows that rR spectroscopy is a powerful tool for building spin dynamics structure–property relationships by leveraging the selectivity for totally symmetric mode energies. Previous works have attempted to empirically correlate vibrations to features of spin relaxation through terahertz spectroscopy<sup>39–42</sup> or computation of the vibrational density of states.<sup>5,32</sup> However, terahertz or IR absorption spectroscopies

rely on electric dipole selection rules that select for *ungerade* modes in centrosymmetric complexes. Group theory analysis has established a selection rule for spin–phonon coupling, which indicates that only *gerade* vibrations (predominately  $a_{1g}$  modes) are able to couple to the spins in centrosymmetric complexes.<sup>14,17</sup> Thus, IR or far-IR absorption spectroscopies do not probe the modes of relevance for spin–phonon coupling for square-planar complexes. Furthermore, the full vibrational density of states, or even atom-specific partial density of states, becomes very complicated in macrocyclic qubits like porphyrins, rendering statements about specific vibrational modes challenging. A-term enhanced rR spectra, however, have the key virtue of selectivity for the  $a_1/a_{1g}$  modes most relevant to spin relaxation, making spectral correlations much more straightforward.

In addition, the magnitude of A-term resonance enhancement provided by excitation into a strongly dipole-allowed electronic absorption band is determined by the amount of excited-state distortion through the electronuclear coupling integral.<sup>37</sup> This same term arises in the ligand field theory of spin–phonon coupling, where excited-state distortion is required to observe nonzero  $dg_i/dQ$ .<sup>14</sup> Thus, there may be a connection between the magnitude of resonance enhancement and the magnitude of spin–phonon coupling itself. The caveat is that the electronic excited state of relevance is different for  $g$ -tensor contributions ( $d$ – $d$  transition) vs. rR spectroscopy (charge transfer). In general, one cannot reliably acquire rR spectra for  $d$ – $d$  bands, and many molecular qubits feature intense electronic transitions that obscure these transitions in electronic absorption spectra. The excited-state distortions need not be the same between the two types of electronic excited states. Further work will investigate whether reliable information on spin relaxation can be extracted from the magnitude of A-term enhancement in rR spectra of molecular qubits.

#### 5.4. Conclusions

This work probes the effect of the ruffling distortion on spin relaxation in a series of three copper porphyrins. Two of the three members of the series (CuOEP and CuTiPP) display room-temperature coherence, indicating the suitability of copper porphyrins as a new class of molecules for room-temperature molecular quantum information science applications.

Unlike in the well-studied case of  $b_{2u}$  bending/saddling vibrations, increasing  $b_{1u}$  ruffling distortion does not correlate to decreased  $T_1$  times, despite the mode transforming as  $a_1$  in  $D_{2d}$ . This unexpected result may indicate that primary coordination sphere distortions are required to materially activate new vibrational modes for spin relaxation, and secondary sphere effects such as ruffling have too weak an influence on angular momentum and spin-orbit coupling to induce spin flips. Computational spin relaxation models fail to account for the insensitivity of  $T_1$  to the ruffling distortion, indicating a direction for future theoretical efforts. rR spectroscopy successfully identifies a specific vibrational mode with totally symmetric character that correctly trends with the experimental  $T_1$  local mode fits. Thus, this study indicates the primary vibrational modes responsible for  $S = \frac{1}{2}$  CuP spin relaxation above  $\sim 60$  K correspond to bond stretches with totally symmetric character, not ultra-low-energy modes of rotational character.

## 5.5. References

- (1) M. Atzori and R. Sessoli, The Second Quantum Revolution: Role and Challenges of Molecular Chemistry, *J. Am. Chem. Soc.*, **2019**, *141*(29), 11339–11352, DOI: 10.1021/jacs.9b00984.
- (2) R. Mirzoyan, N. P. Kazmierczak and R. G. Hadt, Deconvolving Contributions to Decoherence in Molecular Electron Spin Qubits: A Dynamic Ligand Field Approach, *Chem.–Eur. J.*, **2021**, *27*, 9482–9494, DOI: 10.1002/chem.202100845.
- (3) K. Bader, D. Dengler, S. Lenz, B. Endeward, S.-D. Jiang, P. Neugebauer and J. van Slageren, Room Temperature Quantum Coherence in a Potential Molecular Qubit, *Nat. Commun.*, **2014**, *5*(1), 5304, DOI: 10.1038/ncomms6304.
- (4) M. S. Fataftah, M. D. Krzyaniak, B. Vlaisavljevich, M. R. Wasielewski, J. M. Zadrozny and D. E. Freedman, Metal–Ligand Covalency Enables Room Temperature Molecular Qubit Candidates, *Chem. Sci.*, **2019**, *10*(27), 6707–6714, DOI: 10.1039/C9SC00074G.
- (5) M. J. Amdur, K. R. Mullin, M. J. Waters, D. Puggioni, M. K. Wojnar, M. Gu, L. Sun, P. H. Oyala, J. M. Rondinelli and D. E. Freedman, Chemical Control of Spin–Lattice

- Relaxation to Discover a Room Temperature Molecular Qubit, *Chem. Sci.*, **2022**, *13*, 7034–7045, DOI: 10.1039/D1SC06130E.
- (6) M. Atzori, L. Tesi, E. Morra, M. Chiesa, L. Sorace and R. Sessoli, Room-Temperature Quantum Coherence and Rabi Oscillations in Vanadyl Phthalocyanine: Toward Multifunctional Molecular Spin Qubits, *J. Am. Chem. Soc.*, **2016**, *138*(7), 2154–2157, DOI: 10.1021/jacs.5b13408.
- (7) M. Atzori, E. Morra, L. Tesi, A. Albino, M. Chiesa, L. Sorace and R. Sessoli, Quantum Coherence Times Enhancement in Vanadium(IV)-Based Potential Molecular Qubits: The Key Role of the Vanadyl Moiety, *J. Am. Chem. Soc.*, **2016**, *138*, 11234–11244.
- (8) A.-M. Ariciu, D. H. Woen, D. N. Huh, L. E. Nodaraki, A. K. Kostopoulos, C. A. P. Goodwin, N. F. Chilton, E. J. L. McInnes, R. E. P. Winpenny, W. J. Evans and F. Tuna, Engineering Electronic Structure to Prolong Relaxation Times in Molecular Qubits by Minimising Orbital Angular Momentum, *Nat. Commun.*, **2019**, *10*(1), 3330, DOI: 10.1038/s41467-019-11309-3.
- (9) D. W. Laorenza, A. Kairalapova, S. L. Bayliss, T. Goldzak, S. M. Greene, L. R. Weiss, P. Deb, P. J. Mintun, K. A. Collins, D. D. Awschalom, T. C. Berkelbach and D. E. Freedman, Tunable Cr<sup>4+</sup> Molecular Color Centers, *J. Am. Chem. Soc.*, **2021**, *143*, 21350–21363, DOI: 10.1021/jacs.1c10145.
- (10) S. L. Bayliss, D. W. Laorenza, P. J. Mintun, B. D. Kovos, D. E. Freedman and D. D. Awschalom, Optically Addressable Molecular Spins for Quantum Information Processing, *Science*, **2020**, *370*(6522), 1309–1312, DOI: 10.1126/science.abb9352.
- (11) S. L. Bayliss, P. Deb, D. W. Laorenza, M. Onizhuk, G. Galli, D. E. Freedman and D. D. Awschalom, Enhancing Spin Coherence in Optically Addressable Molecular Qubits through Host-Matrix Control, *Phys. Rev. X*, **2022**, *12*(3), 031028, DOI: 10.1103/PhysRevX.12.031028.
- (12) N. P. Kazmierczak, K. M. Luedecke, E. T. Gallmeier and R. G. Hadt,  $T_1$  Anisotropy Elucidates Spin Relaxation Mechanisms in an  $S = 1$  Cr(IV) Optically Addressable Molecular Qubit, *J. Phys. Chem. Lett.*, **2023**, *14*(34), 7658–7664, DOI: 10.1021/acs.jpcclett.3c01964.

- (13) R. Mirzoyan and R. G. Hadt, The Dynamic Ligand Field of a Molecular Qubit: Decoherence through Spin–Phonon Coupling, *Phys. Chem. Chem. Phys.*, **2020**, 22(20), 11249–11265, DOI: 10.1039/D0CP00852D.
- (14) N. P. Kazmierczak, R. Mirzoyan and R. G. Hadt, The Impact of Ligand Field Symmetry on Molecular Qubit Coherence, *J. Am. Chem. Soc.*, **2021**, 143(42), 17305–17315, DOI: 10.1021/jacs.1c04605.
- (15) A. Lunghi and S. Sanvito, How Do Phonons Relax Molecular Spins?, *Sci. Adv.*, **2019**, 5(9), eaax7163, DOI: 10.1126/sciadv.aax7163.
- (16) A. Lunghi and S. Sanvito, The Limit of Spin Lifetime in Solid State Electronic Spins, *J. Phys. Chem. Lett.*, **2020**, 11(15), 6273–6278, DOI: 10.1021/acs.jpcclett.0c01681.
- (17) F. Santanni, A. Albino, M. Atzori, D. Ranieri, E. Salvadori, M. Chiesa, A. Lunghi, A. Bencini, L. Sorace, F. Totti and R. Sessoli, Probing Vibrational Symmetry Effects and Nuclear Spin Economy Principles in Molecular Spin Qubits, *Inorg. Chem.*, **2021**, 60(1), 140–151, DOI: 10.1021/acs.inorgchem.0c02573.
- (18) L. Escalera-Moreno, N. Suaud, A. Gaita-Ariño and E. Coronado, Determining Key Local Vibrations in the Relaxation of Molecular Spin Qubits and Single-Molecule Magnets, *J. Phys. Chem. Lett.*, **2017**, 8(7), 1695–1700, DOI: 10.1021/acs.jpcclett.7b00479.
- (19) E. Garlatti, A. Albino, S. Chicco, V. H. A. Nguyen, F. Santanni, L. Paolasini, C. Mazzoli, R. Caciuffo, F. Totti, P. Santini, R. Sessoli, A. Lunghi and S. Carretta, The Critical Role of Ultra-Low-Energy Vibrations in the Relaxation Dynamics of Molecular Qubits, *Nat. Commun.*, **2023**, 14(1), 1653, DOI: 10.1038/s41467-023-36852-y.
- (20) N. P. Kazmierczak and R. G. Hadt, Illuminating Ligand Field Contributions to Molecular Qubit Spin Relaxation via  $T_1$  Anisotropy, *J. Am. Chem. Soc.*, **2022**, 144(45), 20804–20814, DOI: 10.1021/jacs.2c08729.
- (21) A. Lunghi, Toward Exact Predictions of Spin-Phonon Relaxation Times: An Ab Initio Implementation of Open Quantum Systems Theory, *Sci. Adv.*, **2022**, 8(31), eabn7880, DOI: 10.1126/sciadv.abn7880.

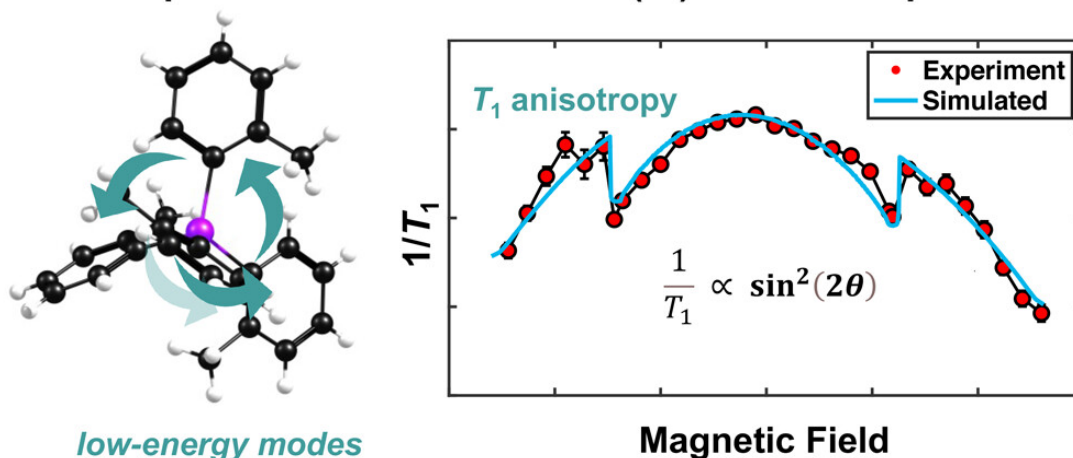
- (22) A. H. Follmer, R. D. Ribson, P. H. Oyala, G. Y. Chen and R. G. Hadt, Understanding Covalent versus Spin–Orbit Coupling Contributions to Temperature-Dependent Electron Spin Relaxation in Cupric and Vanadyl Phthalocyanines, *J. Phys. Chem. A*, **2020**, *124*(44), 9252–9260, DOI: 10.1021/acs.jpca.0c07860.
- (23) A. J. Fielding, S. Fox, G. L. Millhauser, M. Chattopadhyay, P. M. H. Kroneck, G. Fritz, G. R. Eaton and S. S. Eaton, Electron Spin Relaxation of Copper(II) Complexes in Glassy Solution between 10 and 120K, *J. Magn. Reson.*, **2006**, *179*(1), 92–104, DOI: 10.1016/j.jmr.2005.11.011.
- (24) C. J. Kingsbury and M. O. Senge, The Shape of Porphyrins, *Coord. Chem. Rev.*, **2021**, *431*, 213760, DOI: 10.1016/j.ccr.2020.213760.
- (25) W. Jentzen, X.-Z. Song and J. A. Shelnutt, Structural Characterization of Synthetic and Protein-Bound Porphyrins in Terms of the Lowest-Frequency Normal Coordinates of the Macrocycle, *J. Phys. Chem. B*, **1997**, *101*(9), 1684–1699, DOI: 10.1021/jp963142h.
- (26) E. B. Fleischer, C. K. Miller and L. E. Webb, Crystal and Molecular Structures of Some Metal Tetraphenylporphines, *J. Am. Chem. Soc.*, **1964**, *86*(12), 2342–2347, DOI: 10.1021/ja01066a009.
- (27) M. Zeller, S. J. DiMuzio, R. J. Wilcox and A. D. Hunter, *CCDC 252379: Experimental Crystal Structure Determination*, *CSD Commun*, **2005**, DOI: 10.5517/cc8gm8l.
- (28) C. Chen, X.-T. He, D.-L. Hong, J.-W. Wang, Y.-H. Luo and B.-W. Sun, Tuning the Crystal Structures of Metal-Tetraphenylporphines via a Magnetic Field, *New J. Chem.*, **2018**, *42*(15), 12570–12575, DOI: 10.1039/C8NJ01882K.
- (29) H.-S. He, A Second Polymorph of (5,10,15,20-Tetra-phenylporphyrinato)Copper(II), *Acta Crystallogr., Sect. E: Struct. Rep. Online*, **2007**, *63*(4), m976–m977, DOI: 10.1107/S1600536807008574.
- (30) L. Aparici Plaza and J. Chojnacki, Influence of Chloro-form on Crystalline Products Yielded in Reactions of 5,10,15,20- Tetra-phenyl-porphyrin with HCl and Copper(II) Salts, *Acta Crystallogr. C*, **2012**, *68*(1), m24–m28, DOI: 10.1107/S0108270111054102.

- (31) S. von Kugelgen, M. D. Krzyaniak, M. Gu, D. Puggioni, J. M. Rondinelli, M. R. Wasielewski and D. E. Freedman, Spectral Addressability in a Modular Two Qubit System, *J. Am. Chem. Soc.*, **2021**, *143*(21), 8069–8077, DOI: 10.1021/jacs.1c02417.
- (32) C.-J. Yu, S. von Kugelgen, M. D. Krzyaniak, W. Ji, W. R. Dichtel, M. R. Wasielewski and D. E. Freedman, Spin and Phonon Design in Modular Arrays of Molecular Qubits, *Chem. Mater.*, **2020**, *32*(23), 10200–10206, DOI: 10.1021/acs.chemmater.0c03718.
- (33) C.-J. Yu, M. D. Krzyaniak, M. S. Fataftah, M. R. Wasielewski and D. E. Freedman, A Concentrated Array of Copper Porphyrin Candidate Qubits, *Chem. Sci.*, **2019**, *10*(6), 1702–1708, DOI: 10.1039/C8SC04435J.
- (34) K. J. Standley and R. A. Vaughan, *Electron Spin Relaxation Phenomena in Solids*, Springer US, Boston, MA, **1969**, DOI: 10.1007/978-1-4899-6539-4.
- (35) E. S. Sabisky and C. H. Anderson, Spin-Lattice Relaxation of  $Tm^{2+}$  in  $CaF_2$ ,  $SrF_2$ , and  $BaF_2$ , *Phys. Rev. B: Condens. Matter Mater. Phys.*, **1970**, *1*(5), 2028–2040, DOI: 10.1103/PhysRevB.1.2028.
- (36) L. Gu and R. Wu, Origin of the Anomalously Low Raman Exponents in Single Molecule Magnets, *Phys. Rev. B*, **2021**, *103*(1), 014401, DOI: 10.1103/PhysRevB.103.014401.
- (37) A. C. Albrecht, On the Theory of Raman Intensities, *J. Chem. Phys.*, **1961**, *34*(5), 1476–1484, DOI: 10.1063/1.1701032.
- (38) J. G. Rankin and R. S. Czernuszewicz, Fingerprinting Petroporphyrin Structures with Vibrational Spectroscopy: Resonance Raman Spectra of Nickel and Vanadyl Etioporphyrins I and III, *Org. Geochem.*, **1993**, *20*(5), 521–538, DOI: 10.1016/0146-6380(93)90021-3.
- (39) M. Atzori, S. Benci, E. Morra, L. Tesi, M. Chiesa, R. Torre, L. Sorace and R. Sessoli, Structural Effects on the Spin Dynamics of Potential Molecular Qubits, *Inorg. Chem.*, **2018**, *57*(2), 731–740, DOI: 10.1021/acs.inorgchem.7b02616.
- (40) A. Albino, S. Benci, L. Tesi, M. Atzori, R. Torre, S. Sanvito, R. Sessoli and A. Lunghi, First-Principles Investigation of Spin–Phonon Coupling in Vanadium-Based Molecular Spin Quantum Bits, *Inorg. Chem.*, **2019**, *58*(15), 10260–10268, DOI: 10.1021/acs.inorgchem.9b01407.

- (41) A. Albino, S. Benci, M. Atzori, L. Chelazzi, S. Ciattini, A. Taschin, P. Bartolini, A. Lunghi, R. Righini, R. Torre, F. Totti and R. Sessoli, Temperature Dependence of Spin–Phonon Coupling in [VO(Acac)<sub>2</sub>]: A Computational and Spectroscopic Study, *J. Phys. Chem. C*, **2021**, *125*(40), 22100–22110, DOI: 10.1021/acs.jpcc.1c06916.
- (42) L. C. d. Camargo, M. Briganti, F. S. Santana, D. Stinghen, R. R. Ribeiro, G. G. Nunes, J. F. Soares, E. Salvadori, M. Chiesa, S. Benci, R. Torre, L. Sorace, F. Totti and R. Sessoli, Exploring the Organometallic Route to Molecular Spin Qubits: The [CpTi(Cot)] Case, *Angew. Chem.*, **2021**, *133*(5), 2620–2625, DOI: 10.1002/ange.202009634.

**CHAPTER 6:  $T_1$  ANISOTROPY ELUCIDATES SPIN RELAXATION MECHANISMS IN AN  $S = 1$  Cr(IV) OPTICALLY ADDRESSABLE MOLECULAR QUBIT**

**Spin-lattice relaxation in Cr(IV) molecular qubits**



Adapted with permission from:

Kazmierczak, N. P.<sup>†</sup>; Luedecke, K. M.<sup>†</sup>; Gallmeier, E. T.; Hadt, R. G. “ $T_1$  Anisotropy Elucidates Spin Relaxation Mechanisms in an  $S = 1$  Cr(IV) Optically Addressable Molecular Qubit.” *J. Phys. Chem. Lett.* **2023**, *14* (34), 7658. DOI: 10.1021/acs.jpcllett.3c01964.

<sup>†</sup>Co-first author.

Copyright 2023 American Chemical Society.

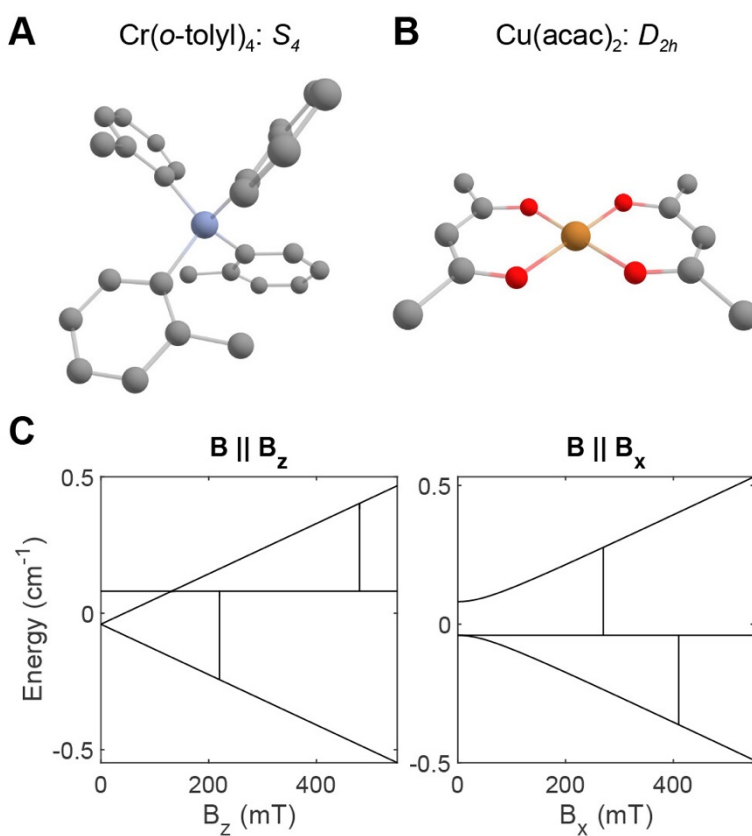
## 6.1. Introduction

The anionic nitrogen vacancy ( $\text{NV}^-$ ) center in diamond constitutes one of the most widely implemented platforms for quantum sensing and imaging.<sup>1</sup> Substitutional replacement of two carbons in the diamond lattice with a nitrogen and a vacancy forms an  $S = 1$  paramagnetic defect that exhibits selective photoluminescence behavior depending on the Zeeman sublevel that the spin occupies.<sup>2,3</sup> Furthermore, optical excitation of the  $\text{NV}^-$  center accumulates ground-state spin polarization through a spin-selective intersystem crossing mechanism. These two features enable optical initialization and detection of quantum states in the Zeeman sublevels of the  $S = 1$  defect, permitting a much greater degree of spatial localization than can be achieved with direct resonant microwave readout of the Zeeman sublevels. This functionality has enabled quantum sensing in a variety of applications,<sup>1</sup> including atomic scale magnetic resonance imaging of nuclear spin clusters,<sup>4</sup> probing intracellular molecular dynamics,<sup>5</sup> nanometer-scale thermometry with millikelvin accuracy inside a living cell,<sup>6</sup> imaging magnetic fields in live magnetotactic bacteria,<sup>7</sup> measuring local ion concentrations,<sup>8</sup> and strain/pressure sensing.<sup>8</sup> The main downsides of  $\text{NV}^-$  centers relate to the large bulk of the diamond lattice, the poor control over where the  $\text{NV}^-$  defects arise in the lattice, and the fixed nature of the  $\text{NV}^-$  center coherence properties.<sup>9</sup>

Production of molecules exhibiting the same optical initialization and readout capabilities would overcome these limitations of  $\text{NV}^-$  centers and open up molecular *in situ* and *in vivo* quantum sensing capabilities on the single nanometer scale. Multiple systems have been investigated on the basis of both  $S = 1$  and  $S > 1$  architectures,<sup>10-12</sup> but to date, the most successful molecules have been pseudo- $T_d$   $S = 1$  Cr(IV) tetraaryl and tetraalkyl complexes,<sup>13,14</sup> which display optical addressability and prolonged coherence times when diluted in nonisostructural diamagnetic matrices.<sup>15</sup> However, owing to fast spin relaxation, Cr(IV) molecular qubits do not display spin coherence at temperatures higher than  $\sim 60$  K, at which point  $T_m$  becomes spin-lattice relaxation ( $T_1$ ) limited. This behavior is significantly inferior to that of both  $\text{NV}^-$  centers and microwave addressable  $S = 1/2$  molecular qubits such as VOPc and  $[\text{Cu}(\text{mnt})_2]^{2-}$ , which display coherence up to room temperature.<sup>16-18</sup> In particular, quantum sensing of biological systems would benefit greatly

from the ability to perform room-temperature coherence measurements under ambient biochemical conditions. Therefore, to maximize the full potential of optically addressable molecular qubits, it is essential to identify and remove contributions to fast spin relaxation.

Recently,  $T_1$  anisotropy has emerged as a novel technique for interrogating spin-phonon coupling contributions to spin relaxation and decoherence in  $S = 1/2$  systems.<sup>19</sup> This approach can provide information regarding the vibrational contributions and mechanism of spin relaxation that is not accessible through more common temperature-dependent  $T_1$  measurements. Here, we apply this methodology to  $\text{Cr}(o\text{-tolyl})_4$ , an  $S = 1$  tetraaryl Cr(IV) optically addressable molecular qubit (**Scheme 6.1A**). We find qualitatively different  $T_1$  anisotropy patterns relative to  $\text{Cu}(\text{acac})_2$  (**Scheme 6.1B**) and other copper(II) and vanadium(IV)  $S = 1/2$  systems, indicating unique spin-phonon coupling contributions to spin relaxation.



**Scheme 6.1.** Molecular Crystal Structures and Point Groups of **(A)**  $S = 1$   $\text{Cr}(o\text{-tolyl})_4$  and **(B)**  $S = 1/2$   $\text{Cu}(\text{acac})_2$ ; **(C)** Simulated Zeeman Levels for  $\text{Cr}(o\text{-tolyl})_4$  with  $D = -0.117$   $\text{cm}^{-1}$ , as determined in this work.<sup>a</sup> In panels A and B, C = gray, Cr = blue, Cu = orange, and O = red. H atoms omitted for clarity. In panel B, slight distortion from planarity. In panel C, vertical lines denote X-band EPR transitions at 9.6 GHz

## 6.2. Results and Discussion

The concept of  $T_1$  anisotropy probes how the spin relaxation rate changes for molecules with different orientations relative to the spectrometer's applied magnetic field ( $B_0$ ). In general, EPR spectra of powder or frozen solution samples can display resonance positions selective for these different molecular orientations, enabling access to orientation-specific relaxation rates without the need for single crystal experiments.<sup>20</sup> Cr(IV) qubits satisfy this requirement for orientation selectivity, as the microwave absorption spectrum of  $\text{Cr}(o\text{-tolyl})_4$  is composed of two transitions between the three  $M_S$  sublevels (**Scheme 6.1C**), and each spin transition occurs at a different resonance field depending on the molecular orientation (**Figure 6.1A, B**). By weighting these orientations with the fraction of molecules absorbing at the given field and averaging over the two spin transitions, we can define an average molecular orientation probed by EPR at any given resonance field (**Figure 6.1C**). At X-band, the pure parallel position can be addressed by performing pulsed EPR at 220 and 480 mT (lines atop **Figure 6.1A**). While no single position is uniquely selective for the perpendicular orientation, the Pake pattern horns at 280 and 410 mT display an average orientation around  $80^\circ$ , giving a close approximation to the pure perpendicular position behavior.

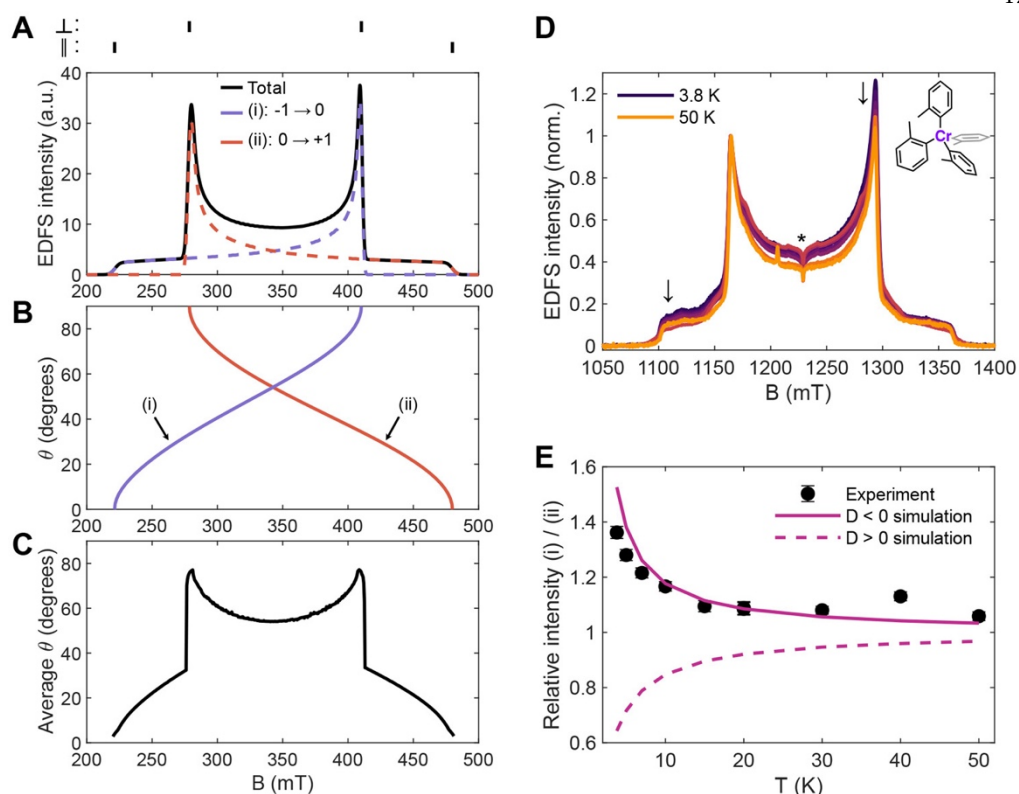


**Figure 6.1.** Anisotropy in Cr(IV) pulsed EPR. (A) Simulated X-band EDFS for Cr(*o*-tolyl)<sub>4</sub> showing the contributions from each spin transition in the case of  $D < 0$ . (B) Orientation of the molecule with respect to the value of  $B_0$ .  $\theta = 0^\circ$  indicates  $B_0$  is parallel to the principal symmetry axis of the axial ZFS tensor. (C) Average orientation of the molecule over all spin transitions. (D) Variable-temperature Q-band EDFSs using soft pulses ( $\pi = 80$  ns) and normalized to the peak at 1160 mT. \* likely indicates an artifact due to cross-relaxation or a double-quantum transition (Supporting Information, Section 3). (E) Comparison between experimental powder manifold intensities and simulations for  $D < 0$  and  $D > 0$

The identity of the  $M_S = -1 \rightarrow 0$  and  $M_S = 0 \rightarrow +1$  transitions depends upon the sign of the axial zero-field splitting (ZFS) parameter  $D$ . While a perfectly  $T_d$   $S = 1$  molecule cannot exhibit ZFS owing to cubic symmetry and a lack of second-order spin-orbit interactions,<sup>21</sup> Cr(*o*-tolyl)<sub>4</sub> crystallizes in the  $S_4$  point group.<sup>13</sup> The sign of  $D$  is sensitive to changes in the electronic structure upon structural distortions from  $T_d$  to  $S_4$ , including

splitting of ligand field excited-state energies and anisotropic orbital covalency.<sup>21,22</sup> Correct computational modeling of the sign of  $D$  is therefore essential for spin-phonon coupling calculations to accurately describe the electronic structure. Although the absolute ZFS parameters for  $\text{Cr}(o\text{-tolyl})_4$  have been reported ( $|D| = 0.117 \text{ cm}^{-1}$ ,  $E \approx 0 \text{ cm}^{-1}$ )<sup>13</sup>, the sign of the ZFS has yet to be determined experimentally. To achieve this, we acquired variable-temperature Q-band echo-detected field sweeps (EDFSs) from 3.8 to 50 K (**Figure 6.1D**). Soft microwave pulses were employed to suppress electron spin echo envelope modulation (ESEEM), which can add artifacts to EDFS spectra, and  $T_m$  was measured at several field positions and temperatures to ensure anisotropic  $T_m$  did not bias the EDFS intensity (Supporting Information, Sections 3–4). As the sample temperature increases, the intensity of the spin transition spanning 1100–1290 mT decreases relative to the transition spanning 1160–1370 mT (arrows in **Figure 6.1D**). This behavior and corresponding simulation (**Figure 6.1E**) indicates that the former is the ground-state  $M_S = -1 \rightarrow 0$  transition and that the sign of  $D$  is negative for  $\text{Cr}(o\text{-tolyl})_4$  ( $D = -0.121 \text{ cm}^{-1}$ ), consistent with calculations.<sup>23,24</sup> Note this sign differs from the pseudo- $T_d$  Cr(IV) siloxide complex,  $\text{Cr}(\text{DTBMS})_4$ , which exhibits  $D > 0$ .<sup>25</sup> This indicates that distortions away from  $T_d$  can produce categorically distinct electronic structure modifications in Cr(IV) complexes, which may lead to diverging spin-phonon coupling behavior.

Inversion recovery  $T_1$  measurements at 40 K were conducted on a 1.8% dilution of  $\text{Cr}(o\text{-tolyl})_4$  into an isostructural diamagnetic  $\text{Sn}(o\text{-tolyl})_4$  matrix (**Figure 6.2A–C**). The slowest rates of spin relaxation were recorded at the pure parallel orientations, while the perpendicular orientations also displayed local minima in the spin relaxation rates (**Figure 6.2B**). Fastest spin relaxation was observed at the intermediate orientations closest to  $45^\circ$ , which are found both immediately to the outside of the Pake pattern horns and also in the very center of the spectrum (**Figure 6.1C**). The  $T_1$  anisotropy pattern can be most nearly described by a  $\sin^2(2\theta)$  functional form (**Figure 6.2C**), where  $\theta$  is obtained from the orientation analysis in **Figure 6.1**. The  $\sin^2(2\theta)$  function accounts for the slower spin relaxation along the canonical (parallel and perpendicular) orientations and faster spin relaxation along the intermediate orientations. Additionally, a  $\sin^2(\theta)$  function and a linear function proportional to  $B$  (linear in the magnetic field) were considered. Note that the

function linear in  $B$  does not directly depend upon the molecular angle  $\theta$  and is therefore more precisely construed as isotropic field-dependent spin relaxation rather than true anisotropy (Supporting Information, Section 5). This term may be understood as the slope of the Brons–van Vleck spin lifetime field dependence commonly observed in AC magnetometry, and this slope is indeed negative at X-band fields (0.3 T) for common V(IV) qubits.<sup>26</sup> A least-squares fit of the inversion recovery data was conducted to quantify the relative contributions of different anisotropy functions (Supporting Information, Section 5.1 and 5.3). The 40 K  $T_1$  field dependence of Cr(*o*-tolyl)<sub>4</sub> can be described by this method as composed of 13%  $\sin^2(2\theta)$ , 6%  $\sin^2(\theta)$ , and 5% linear in  $B$  contributions, with a 76% constant (isotropic) component. This method of  $T_1$  anisotropy analysis is applicable to any EPR-addressable  $S = 1$  complex with an anisotropic powder spectrum.

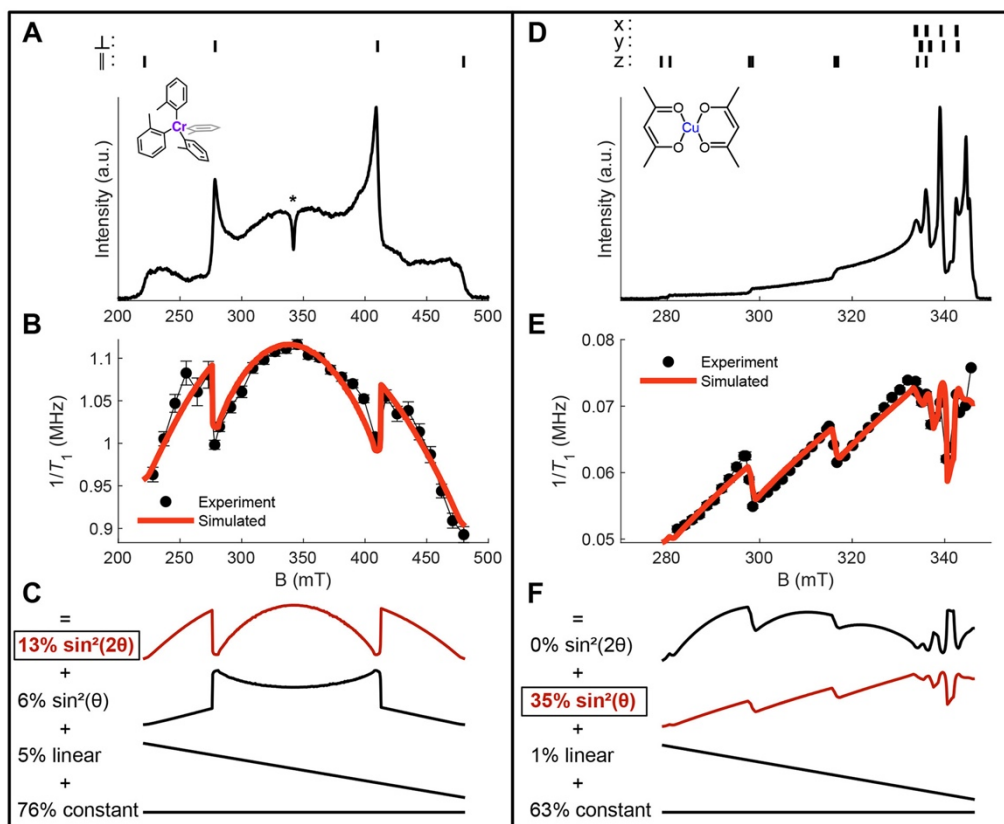


**Figure 6.2.**  $T_1$  anisotropy at 40 K of (A–C)  $\text{Cr}(o\text{-tolyl})_4$  and (D–F)  $\text{Cu}(\text{acac})_2$ . (A, D) X-band EDFs. (B, E)  $T_1$  anisotropy by inversion recovery, overlaid with best fit. (C, F) Orientation functions used to construct the  $T_1$  anisotropy fit

Crucially, this behavior contrasts with that observed for tetragonal  $S = 1/2$  Cu(II), V(IV), and Cr(V) compounds previously investigated by  $T_1$  anisotropy at 100 K, in which the fastest and slowest values of spin relaxation were always found at the canonical orientations.<sup>19,20,27</sup> To see if this was an effect of the temperature regime studied, we collected  $T_1$  anisotropy at 40 K of 0.1%  $\text{Cu}(\text{acac})_2$  diluted in the isostructural diamagnetic matrix  $\text{Pd}(\text{acac})_2$  (**Figure 6.2D–F**). The 40 K  $\text{Cu}(\text{acac})_2$  completely follows the  $\sin^2(\theta)$  functional form with no apparent significant contributions from  $\sin^2(2\theta)$  (**Figure 6.2F**). The spin relaxation rate at the  $45^\circ$  orientation is simply the average of the rates at the canonical positions. These observations point to a qualitatively different origin of  $T_1$  anisotropy in  $\text{Cr}(o\text{-tolyl})_4$  vs  $\text{Cu}(\text{acac})_2$ .

To ascertain the type of vibrations responsible for these distinct patterns, we probed the temperature dependence of the  $T_1$  anisotropy for  $\text{Cr}(o\text{-tolyl})_4$  and  $\text{Cu}(\text{acac})_2$ . We quantify the amount of  $T_1$  anisotropy as a fraction of the largest  $1/T_1$  over all field positions (**Figure S17**). Over the temperature range of 7–60 K, the amount of  $T_1$  anisotropy for  $\text{Cr}(o\text{-tolyl})_4$  steadily decreases, with the dominant  $\sin^2(2\theta)$  anisotropic contribution decreasing from 23% to 10% of the total  $T_1$  (**Figure 6.3**). This decrease with increasing temperature indicates that  $\sin^2(2\theta)$  anisotropy arises from very low-energy degrees of freedom, likely acoustic or pseudoacoustic phonons<sup>28</sup> (*vide infra*). Indeed, the isotropic field-dependent contribution to  $1/T_1$  decreases at the same pace over this temperature range, and this contribution is commonly ascribed to the direct process of spin relaxation.<sup>26</sup> In contrast, the  $\sin^2(\theta)$   $T_1$  anisotropy contribution increases sharply with temperatures for  $\text{Cu}(\text{acac})_2$ , constituting only 0.5% of the total  $T_1$  at 20 K but 62% at 100 K (**Figure 6.3**). Examination of the field-dependent  $T_1$  for  $\text{Cu}(\text{acac})_2$  at 20 K validates that the spin relaxation anisotropy is greatly reduced (**Figure S22**), while the parallel and perpendicular  $T_1$  at 100 K differ by a factor of 2.4, as observed and analyzed previously by the Hadt group.<sup>19</sup> This validates that the  $\sin^2(\theta)$  anisotropy for  $\text{Cu}(\text{acac})_2$  arises from higher-energy molecular vibrational

modes (optical phonons) that are not thermally populated at 20 K. Thus, the  $T_1$  anisotropies for  $\text{Cr}(o\text{-tolyl})_4$  vs  $\text{Cu}(\text{acac})_2$  originate from different types of phonons. Note that both anisotropies are temperature dependent in a manner consistent with the effect of thermal population of vibrational modes.<sup>29-31</sup> Anisotropic spectral diffusion was ruled out as a principal cause of the observed  $T_1$  patterns for both compounds (Supporting Information, Section 5.2).

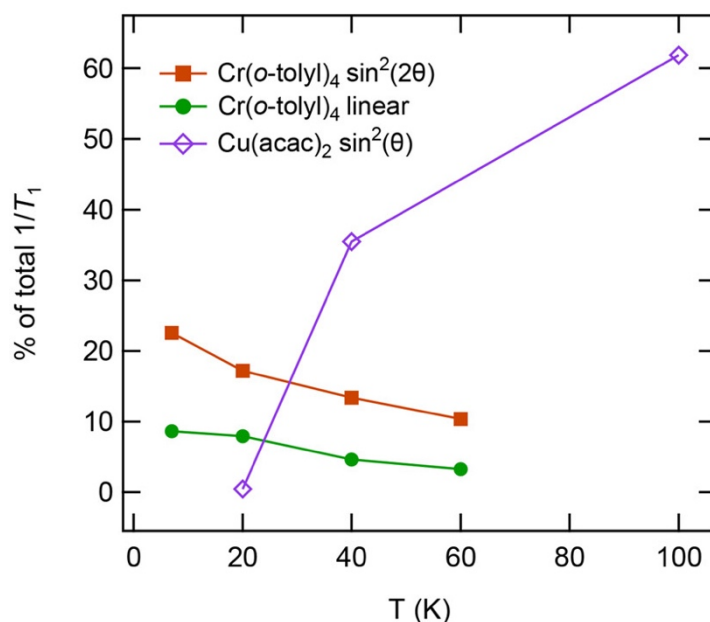


**Figure 6.3.** Temperature dependence of  $T_1$  anisotropy contributions for  $\text{Cr}(o\text{-tolyl})_4$  and  $\text{Cu}(\text{acac})_2$

A major attraction of the  $T_1$  anisotropy methodology lies in the possibility of correlating the observed functional forms (e.g.,  $\sin^2(\theta)$  and  $\sin^2(2\theta)$ ) to their origins in specific molecular degrees of freedom. Previous work has analyzed  $\sin^2(\theta)$  spin relaxation anisotropy for  $\text{Cu}(\text{II})$  and  $\text{V}(\text{IV})$  molecular vibrations and shown it to be consistent with totally symmetric modes with metal–ligand stretching character<sup>29,32,33</sup> inducing relaxation through a modulation of the minority spin component of the ligand field wave function.<sup>19</sup> However, a new theoretical analysis is required to explain the  $\sin^2(2\theta)$  anisotropy in  $\text{Cr}(o\text{-tolyl})_4$ . While  $\sin^2(2\theta)$   $T_1$  anisotropy has not been previously characterized,  $T_m$  anisotropy

with a  $\sin^2(2\theta)$  functional dependence has been observed in several  $S = 1/2$  systems and has been attributed to rotational motion caused by librations.<sup>34,36</sup> This induces a change in resonant field position described by  $dB_{\text{res}}/d\theta$ , which is determined by the derivative of the projected  $g$  value,  $dg/d\theta$ . The derivative of the  $g$ -tensor  $dg/dQ$  has been successfully used as a simplified model for the spin-phonon coupling coefficient describing spin relaxation, where, in this case, the vibrational mode  $Q$  is equal to a rotation  $\theta$ , so there may be a connection between  $dB_{\text{res}}/d\theta$  and spin relaxation in this context as well. Note that here, rotational motion refers specifically to any molecular movement that causes rotation of principal tensor axes of the magnetic Hamiltonian. This does not necessarily imply rigid rotor molecular rotations, and possibilities include coupled rotations of different molecules in the solid-state unit cell (pseudoacoustic or acoustic phonons), glassy librations, or molecular vibrations where the first coordination sphere and the extended ligand framework rotate in opposite directions (Supporting Information, Section 6.1).

We therefore hypothesized that rotational motion from low-energy pseudoacoustic or acoustic phonons may explain the  $\sin^2(2\theta)$  functional form of the  $\text{Cr}(o\text{-tolyl})_4$   $T_1$  anisotropy. As the ZFS ( $D = -0.117 \text{ cm}^{-1}$ ) is smaller than the Zeeman splitting energy at X-band ( $0.32 \text{ cm}^{-1}$  for  $g = 2$  at 340 mT), we assume the spins are aligned along the applied magnetic field and treat the ZFS as a first-order perturbation to the Zeeman splitting of energy levels. Treating  $dB_{\text{res}}/d\theta$  as a quantity proportional to the spin-flip matrix element for rotational motion, we obtain (Supporting Information, Section 6):

$$\frac{1}{T_1} \propto \left| \frac{\partial B_{\text{res}}}{\partial \theta} \right|^2 = \frac{9D^2}{4\beta^2 g^2} \sin^2(2\theta) \quad (6.1)$$

Thus, the  $\sin^2(2\theta)$  form is consistent with the expected  $T_1$  anisotropy due to rotational motion. The decrease in the  $\sin^2(2\theta)$  contribution to the  $T_1$  anisotropy with increasing temperature also suggests that the rotational motion arises from low-energy acoustic or pseudoacoustic phonons. The latter may carry significant rotational character when there are multiple molecules per unit cell,<sup>28</sup> as is the case here ( $Z = 10$ ).<sup>37</sup> Further exploration of

structurally diverse  $S = 1$  complexes will be required to ascertain the generality of the rotational  $\sin^2(2\theta)$  contributions.

The  $T_1$  anisotropy for  $\text{Cr}(o\text{-tolyl})_4$  reduces in magnitude at higher temperatures as molecular vibrations begin to dominate spin relaxation through the Raman process. It remains to be asked why the  $\text{Cr}(o\text{-tolyl})_4$  higher energy ( $>100\text{ cm}^{-1}$ ) molecular vibrations do not display  $T_1$  anisotropy, while the  $\text{Cu}(\text{acac})_2$  totally symmetric vibrations display strong  $\sin^2(\theta)$  anisotropy. This phenomenon is explained by a consideration of the orbital angular momentum matrix elements for a square planar vs. pseudo- $T_d$  system. For  $D_{4h}$   $\text{Cu}(\text{acac})_2$ , the  $d(x^2 - y^2)$  ground state has an orbital angular momentum matrix element with the  $d(xy)$  excited state of squared modulus 4, while the matrix elements with  $d(xz)$  and  $d(yz)$  each have a squared modulus of only 1.<sup>33</sup> These orbital angular momentum matrix elements control the amount of minority spin in the ground-state wave function. Since the different excited states contribute to the wave function's minority spin along only some magnetic field orientations, the total minority spin for  $\text{Cu}(\text{acac})_2$  is greater for the perpendicular orientation than for the parallel orientation, thus giving rise to anisotropic relaxation.<sup>19</sup> However, in the cubic symmetry of the  $T_d$  point group, there can be no difference in matrix elements between the equivalent  $x$ ,  $y$ , and  $z$  directions, so there can be no difference in the minority spin along different orientations. The small distortion from  $T_d$  required to produce nonzero ZFS<sup>25,38</sup> is evidently too small to yield a significant  $\sin^2(\theta)$   $T_1$  anisotropy in  $\text{Cr}(o\text{-tolyl})_4$ . Similar arguments were proposed to rationalize the presence of  $T_1$  anisotropy in tetragonal nitridochromium(V) octaethylporphyrin and nitridochromium(V) tetratolylporphyrin, whereas the rhombic  $\text{Cr}(\text{V})\text{O}(\text{HEBA})_2^-$  complex did not display appreciable  $T_1$  anisotropy.<sup>27,39</sup> Therefore, molecular vibrations (optical phonons) are likely to produce isotropic  $T_1$  for  $\text{Cr}(o\text{-tolyl})_4$ , in contrast to the previously analyzed tetragonal  $S = 1/2$  systems.

### 6.3. Conclusions

In summary, our findings provide the first direct evidence for ascribing features of spin relaxation to specific types of motion in an optically addressable molecular qubit. These degrees of freedom are distinct from the totally symmetric optical phonons implicated in  $S$

= 1/2 microwave addressable molecular systems. As such, these experimental data are critical for defining the nature of spin-phonon couplings and the mechanism of  $T_1$  in theoretical approaches seeking to model spin relaxation lifetimes. We note that the rotational motion contributions analyzed here likely do not dominate spin relaxation rates for  $T > 60$  K, as the anisotropic component of the spin relaxation is reduced at higher temperatures due to the increased role of high-energy molecular vibrations (**Figure 6.3**). Nonetheless, restraining rotational motions for pseudo- $T_d$  Cr(IV) is likely to prolong spin lifetimes. Such structure–function relationships for spin dynamics will be essential for designing molecular optically addressable qubits displaying room temperature coherence.

#### 6.4. References

- (1) Schirhagl, R.; Chang, K.; Loretz, M.; Degen, C. L. Nitrogen-Vacancy Centers in Diamond: Nanoscale Sensors for Physics and Biology. *Annu. Rev. Phys. Chem.* **2014**, *65* (1), 83– 105, DOI: 10.1146/annurev-physchem-040513-103659.
- (2) Doherty, M. W.; Manson, N. B.; Delaney, P.; Jelezko, F.; Wrachtrup, J.; Hollenberg, L. C. L. The Nitrogen-Vacancy Colour Centre in Diamond. *Phys. Rep.* **2013**, *528* (1), 1– 45, DOI: 10.1016/j.physrep.2013.02.001.
- (3) Fataftah, M. S.; Freedman, D. E. Progress towards Creating Optically Addressable Molecular Qubits. *Chem. Commun.* **2018**, *54* (98), 13773– 13781, DOI: 10.1039/C8CC07939K.
- (4) Abobeih, M. H.; Randall, J.; Bradley, C. E.; Bartling, H. P.; Bakker, M. A.; Degen, M. J.; Markham, M.; Twitchen, D. J.; Taminiiau, T. H. Atomic-Scale Imaging of a 27-Nuclear-Spin Cluster Using a Quantum Sensor. *Nature* **2019**, *576* (7787), 411– 415, DOI: 10.1038/s41586-019-1834-7.
- (5) McGuinness, L. P.; Yan, Y.; Stacey, A.; Simpson, D. A.; Hall, L. T.; Maclaurin, D.; Praver, S.; Mulvaney, P.; Wrachtrup, J.; Caruso, F.; Scholten, R. E.; Hollenberg, L. C. L. Quantum Measurement and Orientation Tracking of Fluorescent Nanodiamonds inside Living Cells. *Nat. Nanotechnol.* **2011**, *6* (6), 358– 363, DOI: 10.1038/nnano.2011.64.

- (6) Kucsko, G.; Maurer, P. C.; Yao, N. Y.; Kubo, M.; Noh, H. J.; Lo, P. K.; Park, H.; Lukin, M. D. Nanometre-Scale Thermometry in a Living Cell. *Nature* **2013**, *500* (7460), 54– 58, DOI: 10.1038/nature12373.
- (7) Le Sage, D.; Arai, K.; Glenn, D. R.; DeVience, S. J.; Pham, L. M.; Rahn-Lee, L.; Lukin, M. D.; Yacoby, A.; Komeili, A.; Walsworth, R. L. Optical Magnetic Imaging of Living Cells. *Nature* **2013**, *496* (7446), 486– 489, DOI: 10.1038/nature12072.
- (8) Schirhagl, R.; Chang, K.; Loretz, M.; Degen, C. L. Nitrogen-Vacancy Centers in Diamond: Nanoscale Sensors for Physics and Biology. *Annu. Rev. Phys. Chem.* **2014**, *65* (1), 83– 105, DOI: 10.1146/annurev-physchem-040513-103659.
- (9) Graham, M. J.; Zadrozny, J. M.; Fataftah, M. S.; Freedman, D. E. Forging Solid-State Qubit Design Principles in a Molecular Furnace. *Chem. Mater.* **2017**, *29* (5), 1885– 1897, DOI: 10.1021/acs.chemmater.6b05433.
- (10) Fataftah, M. S.; Bayliss, S. L.; Laorenza, D. W.; Wang, X.; Phelan, B. T.; Wilson, C. B.; Mintun, P. J.; Kovos, B. D.; Wasielewski, M. R.; Han, S.; Sherwin, M. S.; Awschalom, D. D.; Freedman, D. E. Trigonal Bipyramidal  $V^{3+}$  Complex as an Optically Addressable Molecular Qubit Candidate. *J. Am. Chem. Soc.* **2020**, *142* (48), 20400– 20408, DOI: 10.1021/jacs.0c08986.
- (11) Wojnar, M. K.; Laorenza, D. W.; Schaller, R. D.; Freedman, D. E. Nickel(II) Metal Complexes as Optically Addressable Qubit Candidates. *J. Am. Chem. Soc.* **2020**, *142* (35), 14826– 14830, DOI: 10.1021/jacs.0c06909.
- (12) Lenz, S.; Bamberger, H.; Hallmen, P. P.; Thiebes, Y.; Otto, S.; Heinze, K.; van Slageren, J. Chromium(III)-Based Potential Molecular Quantum Bits with Long Coherence Times. *Phys. Chem. Chem. Phys.* **2019**, *21* (13), 6976– 6983, DOI: 10.1039/C9CP00745H.
- (13) Bayliss, S. L.; Laorenza, D. W.; Mintun, P. J.; Kovos, B. D.; Freedman, D. E.; Awschalom, D. D. Optically Addressable Molecular Spins for Quantum Information Processing. *Science* **2020**, *370* (6522), 1309– 1312, DOI: 10.1126/science.abb9352.
- (14) Laorenza, D. W.; Kairalapova, A.; Bayliss, S. L.; Goldzak, T.; Greene, S. M.; Weiss, L. R.; Deb, P.; Mintun, P. J.; Collins, K. A.; Awschalom, D. D.; Berkelbach, T. C.;

- Freedman, D. E. Tunable Cr<sup>4+</sup> Molecular Color Centers. *J. Am. Chem. Soc.* **2021**, *143*, 21350–21363, DOI: 10.1021/jacs.1c10145.
- (15) Bayliss, S. L.; Deb, P.; Laorenza, D. W.; Onizhuk, M.; Galli, G.; Freedman, D. E.; Awschalom, D. D. Enhancing Spin Coherence in Optically Addressable Molecular Qubits through Host-Matrix Control. *Phys. Rev. X* **2022**, *12* (3), 031028, DOI: 10.1103/PhysRevX.12.031028.
- (16) Bader, K.; Dengler, D.; Lenz, S.; Endeward, B.; Jiang, S.-D.; Neugebauer, P.; van Slageren, J. Room Temperature Quantum Coherence in a Potential Molecular Qubit. *Nat. Commun.* **2014**, *5* (1), 5304, DOI: 10.1038/ncomms6304.
- (17) Atzori, M.; Tesi, L.; Morra, E.; Chiesa, M.; Sorace, L.; Sessoli, R. Room-Temperature Quantum Coherence and Rabi Oscillations in Vanadyl Phthalocyanine: Toward Multifunctional Molecular Spin Qubits. *J. Am. Chem. Soc.* **2016**, *138* (7), 2154–2157, DOI: 10.1021/jacs.5b13408.
- (18) Follmer, A. H.; Ribson, R. D.; Oyala, P. H.; Chen, G. Y.; Hadt, R. G. Understanding Covalent versus Spin-Orbit Coupling Contributions to Temperature-Dependent Electron Spin Relaxation in Cupric and Vanadyl Phthalocyanines. *J. Phys. Chem. A* **2020**, *124* (44), 9252–9260, DOI: 10.1021/acs.jpca.0c07860.
- (19) Kazmierczak, N. P.; Hadt, R. G. Illuminating Ligand Field Contributions to Molecular Qubit Spin Relaxation via  $T_1$  Anisotropy. *J. Am. Chem. Soc.* **2022**, *144* (45), 20804–20814, DOI: 10.1021/jacs.2c08729.
- (20) Du, J.-L.; Eaton, G. R.; Eaton, S. S. Temperature and Orientation Dependence of Electron-Spin Relaxation Rates for Bis(Diethyldithiocarbamate)Copper(II). *J. Magn. Reson. A* **1995**, *117* (1), 67–72, DOI: 10.1006/jmra.1995.9971.
- (21) Deaton, J. C.; Gebhard, M. S.; Solomon, E. I. Transverse and Longitudinal Zeeman Effect on [PPh<sub>4</sub>][FeCl<sub>4</sub>]: Assignment of the Ligand Field Transitions and the Origin of the <sup>6</sup>A<sub>1</sub> Ground-State Zero-Field Splitting. *Inorg. Chem.* **1989**, *28* (5), 877–889, DOI: 10.1021/ic00304a016.
- (22) Griffith, J. S. *The Theory of Transition-Metal Ions*; Cambridge University Press, **1961**.

- (23) Sauza-de la Vega, A.; Pandharkar, R.; Stroschio, G. D.; Sarkar, A.; Truhlar, D. G.; Gagliardi, L. Multiconfiguration Pair-Density Functional Theory for Chromium(IV) Molecular Qubits. *JACS Au* **2022**, *2*, 2029, DOI: 10.1021/jacsau.2c00306.
- (24) Janicka, K.; Wysocki, A. L.; Park, K. Computational Insights into Electronic Excitations, Spin-Orbit Coupling Effects, and Spin Decoherence in Cr(IV)-Based Molecular Qubits. *J. Phys. Chem. A* **2022**, *126* (43), 8007– 8020, DOI: 10.1021/acs.jpca.2c06854.
- (25) Bucinsky, L.; Breza, M.; Malček, M.; Powers, D. C.; Hwang, S. J.; Krzystek, J.; Nocera, D. G.; Telser, J. High-Frequency and -Field EPR (HFEP) Investigation of a Pseudotetrahedral Cr<sup>IV</sup> Siloxide Complex and Computational Studies of Related Cr<sup>IV</sup>L<sub>4</sub> Systems. *Inorg. Chem.* **2019**, *58* (8), 4907– 4920, DOI: 10.1021/acs.inorgchem.8b03512.
- (26) Atzori, M.; Morra, E.; Tesi, L.; Albino, A.; Chiesa, M.; Sorace, L.; Sessoli, R. Quantum Coherence Times Enhancement in Vanadium(IV)-Based Potential Molecular Qubits: The Key Role of the Vanadyl Moiety. *J. Am. Chem. Soc.* **2016**, *138*, 11234– 11244, DOI: 10.1021/jacs.6b05574.
- (27) Konda, R.; Du, J.-L.; Eaton, S. S.; Eaton, G. R. Electron Spin Relaxation Rates for Nitridochromium(V) Tetratolylporphyrin and Nitridochromium(V) Octaethylporphyrin in Frozen Solution. *Appl. Magn. Reson.* **1994**, *7* (2–3), 185– 193, DOI: 10.1007/BF03162611.
- (28) Kragoskow, J. G. C.; Mattioni, A.; Staab, J. K.; Reta, D.; Skelton, J. M.; Chilton, N. F. Spin-Phonon Coupling and Magnetic Relaxation in Single-Molecule Magnets. *Chem. Soc. Rev.* **2023**, *52*, 4567, DOI: 10.1039/D2CS00705C.
- (29) Kazmierczak, N. P.; Mirzoyan, R.; Hadt, R. G. The Impact of Ligand Field Symmetry on Molecular Qubit Coherence. *J. Am. Chem. Soc.* **2021**, *143* (42), 17305– 17315, DOI: 10.1021/jacs.1c04605.
- (30) Lunghi, A.; Sanvito, S. The Limit of Spin Lifetime in Solid-State Electronic Spins. *J. Phys. Chem. Lett.* **2020**, *11* (15), 6273– 6278, DOI: 10.1021/acs.jpcllett.0c01681.
- (31) Santanni, F.; Albino, A.; Atzori, M.; Ranieri, D.; Salvadori, E.; Chiesa, M.; Lunghi, A.; Bencini, A.; Sorace, L.; Totti, F.; Sessoli, R. Probing Vibrational Symmetry Effects

- and Nuclear Spin Economy Principles in Molecular Spin Qubits. *Inorg. Chem.* **2021**, *60* (1), 140–151, DOI: 10.1021/acs.inorgchem.0c02573.
- (32)Mirzoyan, R.; Hadt, R. G. The Dynamic Ligand Field of a Molecular Qubit: Decoherence through Spin-Phonon Coupling. *Phys. Chem. Chem. Phys.* **2020**, *22* (20), 11249–11265, DOI: 10.1039/D0CP00852D.
- (33)Mirzoyan, R.; Kazmierczak, N. P.; Hadt, R. G. Deconvolving Contributions to Decoherence in Molecular Electron Spin Qubits: A Dynamic Ligand Field Approach. *Chem.—Eur. J.* **2021**, *27*, 9482–9494, DOI: 10.1002/chem.202100845.
- (34)Du, J.-L.; More, K. M.; Eaton, S. S.; Eaton, G. R. Orientation Dependence of Electron Spin Phase Memory Relaxation Times in Copper(II) and Vanadyl Complexes in Frozen Solution. *Isr. J. Chem.* **1992**, *32* (2–3), 351–355, DOI: 10.1002/ijch.199200041.
- (35)Jackson, C. E.; Lin, C.-Y.; van Tol, J.; Zadrozny, J. M. Orientation Dependence of Phase Memory Relaxation in the V(IV) Ion at High Frequencies. *Chem. Phys. Lett.* **2020**, *739*, 137034, DOI: 10.1016/j.cplett.2019.137034.
- (36)Eaton, S. S.; Eaton, G. R. Relaxation Mechanisms. *eMagRes* **2016**, *5* (4), 1543–1556, DOI: 10.1002/9780470034590.emrstm1507.
- (37)Bayliss, S.; Laorenza, D.; Mintun, P.; Kovos, B.; Freedman, D.; Awschalom, D. *CCDC 1992356: Experimental Crystal Structure Determination*; **2020**; DOI: 10.5517/CCDC.CSD.CC24W6KT.
- (38)Mowat, W.; Shortland, A. J.; Hill, N. J.; Wilkinson, G. Elimination Stabilized Alkyls. Part II. Neopentyl and Related Alkyls of Chromium(IV). *J. Chem. Soc., Dalton Trans.* **1973**, (7), 770–778, DOI: 10.1039/dt9730000770.
- (39)Du, J. L.; Eaton, G. R.; Eaton, S. S. Electron-Spin-Lattice Relaxation in Natural Abundance and Isotopically Enriched Oxo-Chromium(V)Bis (2-Hydroxy-2-Ethylbutyrate). *J. Magn. Reson. A* **1995**, *115* (2), 236–240, DOI: 10.1006/jmra.1995.1172.

**APPENDIX A: SUPPORTING INFORMATION FOR CHAPTER 2:  $\mu$ -  
OXO DIMERIZATION EFFECTS ON GROUND- AND EXCITED-STATE  
PROPERTIES OF A WATER-SOLUBLE IRON PORPHYRIN CO<sub>2</sub>  
REDUCTION CATALYST**

The supporting information is available free of charge at <https://pubs.acs.org/doi/10.1021/acs.inorgchem.2c03215> and includes materials and synthesis, high-resolution mass spectrometry as well as additional UV-vis spectra, EPR spectra, MCD spectra, and TA spectra.

**APPENDIX B: SUPPORTING INFORMATION FOR CHAPTER 3:****THE NON-INNOCENT ROLE OF AMINE ADDITIVES IN THE  
ELECTROCHEMICAL GENERATION OF HIGHLY REDUCED CO  
REDUCTION PRODUCTS IN A MOLECULAR IRON PORPHYRIN  
SYSTEM**

This section is temporarily embargoed.

**APPENDIX C: SUPPORTING INFORMATION FOR CHAPTER 4:  
PHOTOPHYSICS OF A STRUCTURALLY CONSTRAINED NICKEL(II)-  
BIPYRIDINE ARYL HALIDE COMPLEX**

The supporting information is available free of charge at <https://pubs.acs.org/doi/10.1021/acs.inorgchem.3c03822> and includes experimental and computational methods, synthetic details, UV-vis/photochemical data, kinetic modeling, transient absorption spectra analysis, NMR spectra, calculated properties, XYZ of the optimized structures, and additional comments.

**APPENDIX D: SUPPORTING INFORMATION FOR CHAPTER 5:  
DETERMINING THE KEY VIBRATIONS FOR SPIN RELAXATION IN  
RUFFLED CU(II) PORPHYRINS VIA RESONANCE RAMAN  
SPECTROSCOPY**

The supporting information is available free of charge at <https://doi.org/10.1039/d3sc05774g> and includes experimental and computational methods, synthetic details, UV-vis data, powder X-ray diffraction data, single crystal x-ray structure determination, resonance Raman data, electron paramagnetic resonance data, and supplemental discussion.

**APPENDIX E: SUPPORTING INFORMATION FOR CHAPTER 6:  $T_1$   
ANISOTROPY ELUCIDATES SPIN RELAXATION MECHANISMS IN  
AN  $S = 1$  CR(IV) OPTICALLY ADDRESSABLE MOLECULAR QUBIT**

The supporting information is available free of charge at <https://pubs.acs.org/doi/10.1021/acs.jpcclett.3c01964> and includes experimental methods, temperature-dependent EPR fitting,  $T_1$  anisotropy fitting, and theoretical derivation of  $T_1$  anisotropy functional forms.